

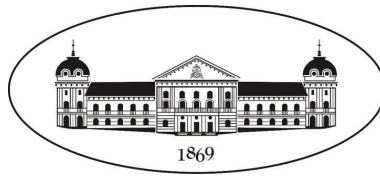
Fast Variability in Selected Chromospherically Active Dwarf Stars and Observational Equipment for Their Study

Rumen G. Bogdanovski

A thesis submitted for the degree of Doctor of Philosophy in the field of
"Astrophysics and Stellar Astronomy", code 01.04.02

June, 2015

Institute of Astronomy with NAO



Bulgarian Academy of Sciences

**Fast Variability in Selected Chromospherically
Active Dwarf Stars and Observational
Equipment for Their Study**

Rumen G. Bogdanovski

A thesis submitted for the degree of Doctor of Philosophy in the field of
"Astrophysics and Stellar Astronomy", code 01.04.02

Advisor: Prof. Dr. Renada Konstantinova-Antova

June, 2015

Rumen G.Bogdanovski

Fast Variability in Selected Chromospherically Active Dwarf Stars and Observational Equipment for Their Study

A thesis submitted for the degree of Doctor of Philosophy in the field of "Astrophysics and Stellar Astronomy", code 01.04.02, June, 2015

Advisor: Prof. Dr. Renada Konstantinova-Antova

Institute of Astronomy with NAO

Bulgarian Academy of Sciences

72 Tsarigradsko shosse blvd.

Sofia BG1756

Contents

Introduction	7
Thesis Structure	9
I Overview	11
1 Chromospherically Active Dwarf Stars	13
1.1 Discovery and Classification	13
1.2 General Characteristics	15
2 High Speed Photometry	21
2.1 Brief overview of the common photo detectors used in Astronomy . .	21
2.1.1 Charge-coupled devices	21
2.1.2 Avalanche photodiodes	22
2.1.3 Photo multiplier tubes	24
2.2 Choice of the detector	26
2.3 Principles of photon counting with PMT	26
2.3.1 Efficiency and pulse heights	27
2.3.2 Photon counting circuit	29
2.3.3 Linearity of the photon counting	29
2.3.4 Signal-to-noise ratio	30
3 Goals of the study	33
II Network-based Synchronous System for High Speed Photometry	35
4 System overview	37
5 Hardware	39
5.1 Photon Counting Module	39
5.1.1 Synchronization Unit and Real Time Clock	40
5.1.2 Channel Counters and Filter/Tag Registers	41

5.1.3	Control and Communication Units	41
5.2	Filter & Tag Control Unit	42
6	Software	43
6.1	Server Software: photosrv	43
6.1.1	Access Control Layer	44
6.1.2	User Communication Layer	44
6.1.3	Hardware Communication Layer	45
6.1.4	Time Synchronization	45
6.2	Client Software: photclient	47
6.3	Data viewer: photview	49
6.4	PCM Simulator: devsim	50
7	Tests and First Light	51
III	Study of the Flares of EV Lacertae and AD Leonis	53
8	Synchronous Observations of EV Lacertae	55
8.1	Observations	56
8.2	Methods	56
8.3	Search for HFOs during flares	57
8.3.1	The flare on September 14, 2004	57
8.3.2	The flare on September 12, 2004	58
8.4	Some colorimetric results based on the data obtained during this campaign	61
9	Photometric study of the flare activity of AD Leonis	65
9.1	Observations	66
9.2	Flare frequency and activity cycle	66
9.3	Using wavelets to search for high–frequency optical oscillations	70
9.3.1	The Wavelet transform used for the performed analysis	70
9.3.2	Reconstruction of the original time series	72
9.3.3	Significance levels	73
9.4	Search for High–frequency optical oscillations during flares	73
9.5	Optical oscillations during flares	76
	Conclusion	87
	Main Contributions	89
	List of publications on the topic, talks and posters	91

Citations found in ADS	93
Acknowledgements	95
Appendices	97
A Manual of devsim	99
B Configuration of devsim	101
C Manual of photsrv	105
D Configuration of photsrv	109
E Configuration of photsrv Access Control	113
F Commands of photsrv	115
G Photon Counting Module (PCM) Communiation Protocol	127
H Batch Scripting for photclient	135
I 2 Channel Photon Counting Module (PCM2) Hardware User's Guide	139
J 5 Channel Photon Counting Module (PCM5) Hardware User's Guide	143
K Filter & Tag Control Unit (FTC 01) Operation	149
L Filter & Tag Control Unit (FTC 02) Operation	153
M Communication between Photon Counting Module and Filter & Tag Control Unit	157
References	163

Introduction

” *Computer science is no more about computers than astronomy is about telescopes.*

— **Edsger Dijkstra**
Dutch computer scientist

The operation of the magnetic dynamo is the primary cause of the chromospheric activity of the dwarf stars. Depending on the mass of the dwarf star, the magnetic dynamo operates in two different regions in the stellar interiors – below the convection zone or in the convection zone. One of the manifestations of its operation are the sporadic flares which are studied in this thesis. The flares are sudden, rapid and intense increases of the brightness of the star. They occur when magnetic energy that has built up in the stellar atmosphere is suddenly released and radiation is emitted across virtually the entire electromagnetic spectrum, from radio waves to x-rays and gamma rays. A flare basically starts with magnetic flux emergence, which is the emergence of magnetic field on the surface of the star, carrying magnetic energy from the interior to the atmosphere. Part of this magnetic energy is immediately released when emerging magnetic field expands to form a magnetic structure on the surface. The expansion is driven by the Lorentz force, generated by the cross-field current – the electric current crossing the magnetic field. On the other hand, the electric current flowing along the magnetic field (called field-aligned current) does not generate Lorentz force, so its energy does not play role in the expansion process. In addition, the field-aligned current is not easy to dissipate in a highly conductive medium such as the corona, so it is stored there as free energy that becomes the energy source of flares and flare-associated phenomena (Shibata & Magara, 2011). In contrast, a finite value of resistivity causes the Ohmic dissipation of the cross-field current, which is especially efficient in a region, called current sheet, where an intensive electric current flows. At some point the dissipation causes topological change in the magnetic field called magnetic reconnection,

this way reducing the magnetic field to a state that has lower energy than before. Through this process the magnetic energy stored inside and outside the current sheet is converted to kinetic and thermal energy. Magnetic reconnection is also accompanied by generation of a strong electric field around the current sheet (convective electric field), which could accelerate charged particles (Shibata & Magara, 2011). Sometimes these events go along with phenomena such as optical oscillations which are rarely observed and not well explained.

Light oscillations during the stellar flares have been reported for the first time by Rodono (1974), and confirmations appeared later by Zhilyaev et al. (2000) and several other articles. Further studies of these subtle phenomena with higher temporal resolution and better precision can contribute to the understanding of the smaller scale processes that take place during the stellar flares and their explanation. Which in turn can help drawing a more detailed picture of the whole event and the processes that cause it.

The observations of variable stars, especially those which show fast changes in their brightness, require high speed and high precision photometry. In order to study events like low amplitude optical oscillations and small scale fluctuations in the light curves, synchronous observations are required. These observations have to be carried out simultaneously at two or more, preferably distant, sites (Romanyuk et al., 2001), which allows the identification and elimination of artifacts produced by the equipment and the atmospheric interferences. In this way the fine structure of the light curve is revealed with a significant certainty.

In order to study these events a new high speed time synchronized photometric system had to be designed, which addresses the requirements of the observations of high frequency subtle phenomena during stellar flares. It provides remote automated and centralized control of the photometric equipment over a computer network, as well as remote monitoring. Furthermore, some preliminary data processing can be performed at the time the data is obtained.

Using this system a study of chromospherically active dwarf stars is carried out, two of which, EV Lacertae and AD Leonis, are presented here. EV Lacertae was observed with the first prototype of this system in 2004 during an international observational campaign in collaboration between Greece, Ukraine and Bulgaria. AD Leonis is observed with the final version of the system during several internal observational campaigns between 2006 and 2008 using three Bulgarian telescopes at NAO Rozhen and AO Belogradchik. The observational data is analyzed using techniques, some of which are used for the first time for searching for high frequency optical oscillations during the flares of the chromospherically active dwarf stars.

Thesis Structure

Part I

This part gives an overview of the chromospherically active dwarf stars and the goals of this study are defined. It also briefly describes several commonly used photo detectors in astronomy and discusses their properties in terms of their fitness for high speed photometry.

Part II

This part describes the principles used in the development of the synchronous system for high speed photometry with distant telescopes. It gives an overview and description of the hardware and the software developed for the system.

Part III

In this part the observations and the methods for data processing are described, and the results from the studies of EV Lacertae and AD Leonis are presented.

Appendices

In this part a complete description of the separate hardware units and software modules of the synchronous system of distant telescopes is given including: timing diagrams, communication protocols, configurations, hardware signals, user guides etc.

Part I

Overview

” *Even if you're on the right track, you'll get run over if you just sit there.*

— **Will Rogers**
US humorist and actor

Chromospherically Active Dwarf Stars

1.1 Discovery and Classification

Flare stars have been detected for the first time in 1924 by Hertzsprung. On one of the plates exposed on January 29 while photographing faint stars in the constellation of Carina one of the stars turned out to be 2^m brighter than it was registered on the other plates. The fast increase of its brightness implied that the star could not be classified as a novae or as an oscillating RR-Lyrae type stars. Therefore Hertzsprung speculated that this event may be a result of an asteroid falling on the star. This seems to be the first registered flare of a chromospherically active dwarf star.

In December 1938 while studying the spectra of faint stars in the constellation of Orion Wachmann (1939) found unusual variable star with abnormal spectrum. The spectrum was obtained by using an objective prism, the spectrum was discretely broadened in one direction at 0.02mm every 6 minutes for one hour in total. During the first third of the exposure the spectrum resembled one of the nucleus of a planetary nebula of the WR type. On the continuous radiation background continuum the spectrum showed strong emissions in H_γ , H_δ , H_ϵ and H_ζ . After that the brightness of the star decreased by at least one and a half magnitudes and on the remaining part of the exposure mostly the emission lines were visible. At the same time the spectrum of the nearby star showed uniform darkening throughout the length. On the photographs taken a month later the spectrum of this star was a normal K star spectrum with no emission lines.

In 1940 during the study of the parallaxes of faint stars van Maanen (1940) found that Lalande 21258 (WX UMa) which is a star of M6e spectral type had brightness of 16^m on more than twenty plates, except for two plates, obtained on May 11, 1939 with separation of half an hour between the exposures, where it had brightness of 14.2^m and 14.5^m . Several years later van Maanen (1945) found out the same during the measurement of the parallax of Ross 882 (YZ CMe). In his announcement he mentioned that both stars had low absolute brightness and are of a late spectral type, so they have to be variable stars of the same type.

In 1947 Luyten discovered a very high proper-motion of 3.3"/year of the star L 726-8 and attracted the attention of the astronomical community to this object. Carpenter discovered that the star has very red colour and he measured its parallax. Page and Struve obtained spectra of this star and determined that it has M6 spectral type with emission lines of hydrogen and calcium. Joy & Humason (1949) observed L 726-8 on the 2.54m reflector telescope on Mount Wilson and discovered that it is a binary star and the two components were separated by 1.5". Van Bisbruk and van den Bos carried out micrometric observations of this binary system. This was a collaboration with Carpenter who exposed a plate for determining the parallax of the star on which he made five separate exposures and one of the images of the star turned out to be much brighter than the other four. During the study of the plate Hughes and Luyten concluded that it was due to flare of the fainter component of the system. In three minutes the brightness of this star increased at least twelve times. Collecting all the previously announced observations Luyten (1949) found that the system L 726-8 is a binary system with components of the lowest mass and estimated the energy of the outburst at about 4×10^{31} Ergs and noted the explosive nature of its release. After that Joy & Humason (1949) announced additional important data obtained on the 2.54m reflector at Mount Wilson. In August and September 1948 they obtained spectra of each of the components of the system. On all of the plates they saw a spectrum of an M dwarf with very strong emissions of the hydrogen and calcium. But one of the spectra was very different. The absorption lines were almost washed out by a strong continuous emission, which was especially pronounced in the wavelengths shorter than the wavelength of H_{δ} . The bright hydrogen lines were amplified compared to the calcium lines and some other emissions lines were vivid, but there were no forbidden lines. Joy and Humason were sure that they had observed similar event to the one registered photographically by Carpenter. However, unlike Luyten who assumed that the increase of the brightness during the flare was caused by the emerging of the emission lines in the fainter component, Joy and Humason concluded that the increase of the brightness is mainly due to the continuous emission. Later the fainter component of the system L 276-8 was designated as UV Ceti and became known by this name.

This study of UV Ceti provoked more detailed research of the variable stars of the spectral type dMe and within the next decades a lot of data on these objects was obtained. During these years photoelectric studies were carried out for the first time. This made possible detailed light curves of the flare events to be registered (Gordon & Kron, 1949; Liller, 1952; Roques, 1953, 1954).

During the years a lot of sporadic studies about the flare stars were published but few of them shed any light on the nature of the flares of the UV Ceti type stars.

They were more about describing these stars, their common characteristics, as well as their place among the other eruptive variable stars. A major role in this played the numerous publications of Petit (1954, 1955, 1957, 1958, 1959, 1961). The results of this initial accumulation of data on the activity of red dwarf stars were described in detail by Gershberg (1970). In 1958 on the X meeting of the International Astronomical Union the stars of the UV Ceti type were classified as a separate type of erupting variable stars and defined as dwarf stars with spectral types from dM3e to dM6e which are characterized by rare and short flares with amplitudes between 1^m to 6^m . The maximum brightness (usually quite sharp) is achieved in several seconds or several tens of seconds after the beginning of the flare and the total duration of the event is from 10 to 50 minutes. UV Ceti is given as a typical example. This definition is updated and extended in the recent revisions of the General Catalog of Variable Stars but is still clearly photometric: "Eruptive variables of the UV Ceti type, these are K Ve–M Ve stars sometimes displaying flare activity with amplitudes from several tenths of a magnitude up to 6 mag in V. The amplitude is considerably greater in the ultraviolet spectral region. Maximum light is attained in several seconds or dozens of seconds after the beginning of a flare; the star returns to its normal brightness in several minutes or dozens of minutes." (Samus et al., 2012).

1.2 General Characteristics

The flare stars of the UV Ceti type are known in the solar vicinity and in several close-by open clusters. Being dim or very faint objects these stars can be studied in details at distances of less than several dozens of parsecs. But on the other hand, they make a significant part of the stellar population. Their density in the solar vicinity is about 0.056 stars/pc^3 and the total stellar density is no more than twice this value (Shakhovskaya, 1995). The fast decrease of the density of the flare stars with the increase of the distance from the sun is explained with the low luminosity of these objects, which makes them difficult to detect at greater distances. This hypothesis was confirmed by the statistical analysis made by Mirzoyan et al. (1988). This way the known stars of the UV Ceti type can be considered a random selection from the stellar population of the galaxy, determined by the location of the sun. A list of the known flare stars in the solar vicinity is created in the Crimean observatory by Gershberg et al. (1999). The current version of this database consists of about 240 flare stars. On the other hand Hawley et al. (1996) carried out a spectral classification of about 2000 close to the sun M dwarfs and found that 105 of them with spectral types M0–M3 and 208 with spectral types M4–M8 show emissions. Com-

binning the data from Gershberg et al. (1999) and Hawley et al. (1996) the spectral distribution of the chromospherically active dwarfs is given in Table 1.1.

Table 1.1. The number of UV Ceti type variable stars by spectral type according to Gershberg et al. (1999) and Hawley et al. (1996)

Spectral type	G0–G9	K0–K3	K4–K8	M0–M3	M4–M8
Number of stars	10	19	25	146	212

Petit (1961) and Joy & Abt (1974) discovered a fast increase of the share of the emission line stars with the transition from early M to late M dwarfs and Joy & Abt (1974) concluded that all dwarf stars later than M5.5 are emission stars. But Giampapa (1983) discovered that among M6 and later dwarfs dominate the non-emission ones. According to Shakhovskoy (1993) the share of the flare stars among the dwarfs increases from 3% for the early G to 30% for the late M types. According to Hawley et al. (1996) the share of emission line objects in K6 is 1%, in M0–M3 is approximately 10% and monotonously increases to 60% in M6 and after that decreases, from 32 dwarfs of later spectral sub-types only 13 have emissions. This complex relation is determined by the combination of several factors: the observable stars, because both the flares and the active chromospheres are easier to find on later stars, the possible longer duration of the evolution phase with existing emissions in the less massive stars (Herbst & Miller, 1989; Hawley et al., 1996) and the real decrease of the activity of the coolest M stars. However, Herbig (1956) discovered a flare on the low mass star VB 10 several orders more powerful than the most powerful ones ever observed on the sun. Later, Linsky et al. (1995) registered an ultra-violet flare on the same star and Fleming et al. (2000) - an X-ray flare. Tinney et al. (1997) suspected variable emission in H_{α} on a very cool and fast-rotating dwarf BRI 0021-0214 with a spectral type $>M9.5$. Also, on the star 2MASSW J0149090+295613 with a spectral type dM9.5e, a flare was registered with amplitude of the equivalent width of H_{α} of about 30 (Liebert et al., 1999). The discovered spots on stars with very low masses (Terndrup et al., 1999; Krishnamurthi et al., 2001) and the X-ray flares on the LHS2065 (Schmitt & Liefke, 2002) suggest, in line with the aforementioned facts, that this type of stellar activity takes place on the stars at least till the end of the main sequence.

Gizis et al. (2000) executed a systematic study of the chromospheric activity of the faintest stars on the main sequence. They studied 60 M7–L dwarfs and found that around M7 almost 100% of the stars have emission in H_{α} and it decreases to 60% in L0 and to 8% in L4 dwarf stars. However, the ratio of the luminosities $L_{H_{\alpha}}/L_{bol} = R_{H_{\alpha}}$ in these ultra-cool stars never reaches the values typical for the

earlier M dwarfs. The decrease of this ratio begins on M6 and continues to the late L dwarfs. Based on the variations of H_{α} in the discussed set Gizis et al. (2000) concluded that the flare activity is a common of the M7–M9.5 dwarfs and that up to half of their fluxes in H_{α} could be due to the flares.

More than 30% of the known stars of the UV Ceti type are members of a double or multiple star system. Moreover, the lower the luminosity of these objects, the more probable it is that they are members of such a system (Pettersen, 1991). But, among all the spectral types, there exist definitely single flare stars. Therefore, being a member of a double or multiple star system is not a necessary condition for this type of activity, however it may be beneficial.

Nonactive M dwarfs are the slowest rotating stars on the main sequence. Their rotational velocities usually do not exceed 2 km/s (Marcy & Chen, 1992) but the rotational speeds of the flare stars as a rule significantly exceed this number. In 40% of the single UV Ceti type variables this velocity is around 10km/s. Out of 29 dMe (dwarfs with emission) stars discussed by Stauffer & Hartmann (1986) 11 have rotational speed higher than 10km/s, while out of 170 dM (dwarfs without emission) stars only 1 or 2 have rotational speeds close to that value. Also, in the non-synchronized double stars the rotational velocities are significantly higher. In Gl 890 (dM1.5e) which is a suspected double $V_{\text{ sini}}=70\text{km/s}$ (Pettersen et al., 1987). In the K2 dwarf BD+08°102 which is in a system with a white dwarf $V_{\text{ sini}} \approx 90\text{km/s}$ (Kellett et al., 1995). According to Bopp & Espenak (1977) and Bopp & Fekel (1977) a strong chromospheric emission and the star spots appear at rotational velocities $>5\text{km/s}$. But this criteria is not strict - there are emission dwarfs with rotational speed around 4km/s (Torres et al., 1985). The stars with rotational speeds less than 1-2 km/s do not flare and have very low chromospheric activity (Pettersen, 1991). While in G and K dwarfs there is a good correlation between the level of activity and the rotational velocity (Hartmann & Noyes, 1987) in M dwarfs this correlation diminishes or even disappears. In the flare stars Proxima Centauri $V_{\text{ sini}}=0.5\text{km/s}$ and in Gl 890 $V_{\text{ sini}}=70\text{km/s}$, however $\lg(L_{H_{\alpha}}/L_{\text{bol}})$ which characterizes the emission of the calm chromosphere in these stars differ only by 0.4. It has to be mentioned that the low value of $V_{\text{ sini}}$ for Proxima Centauri is due to the real rotational speed and not due to the angle i , as its rotational period is about 42 days (Benedict et al., 1993). According to Basri (2001) after M5 the share of the stars with high rotational velocity increases and almost reaches 100% in M9.5 and stays like that in the L dwarfs. All of the above is a confirmation of the role of the rotational velocity in the level of the permanent chromospheric and coronal emissions in the lower right part of the main sequence.

The difference between the G0 dwarfs (stars with a structure similar to the sun) and the latest M dwarfs is quite significant. In this range of spectral types the effective temperature is in the interval from 6000K to 2500K, the masses of the stars are from $1M_{\odot}$ to $0.06M_{\odot}$, the radii from $1R_{\odot}$ to $0.1R_{\odot}$, and the luminosities from $1L_{\odot}$ to $0.0008L_{\odot}$. Along with these considerable quantitative apparent differences, there are important qualitative differences in the internal structure. In the G dwarfs in the central regions a nuclear fusion of the hydrogen takes place and the energy transmission is radiative, the convection zone reaches depths of only about 30% of the stellar radius from the surface, while in stars of spectral types close to M3.5 with masses $0.35M_{\odot}$ and effective temperature about 3500K the layer between the core and the convection zone (the radiative zone) disappears and the stars become fully convective.

The magnetic field topology differs significantly for the fully convective and not fully convective stars. Donati et al. (2008) studied 6 non fully convective dwarfs with spectral types between M0–M2.5 and masses between $0.48M_{\odot}$ and $0.75M_{\odot}$, four of them with significant differential rotation. The results show that for the stars with masses $>0.5M_{\odot}$ the toroidal component dominates over the axisymmetric poloidal component of the magnetic field. On the other hand the stars with masses $<0.5M_{\odot}$ the axisymmetric poloidal component is dominant. A study by Morin et al. (2008) of five stars close to the threshold of full convectiveness with spectral types between M3–M4.5 and masses around $0.35M_{\odot}$ shows that the magnetic fields of these stars are mostly axisymmetric poloidal fields. Another sample of 11 fully convective M dwarfs is studied by Morin et al. (2010). The stars are with spectral types between M5 and M8 and masses between $0.08M_{\odot}$ and $0.22M_{\odot}$. All of the stars in the sample have a dominant poloidal component, however they are divided in two groups: one group has axisymmetric poloidal dipole fields and the other has more complex fields with noticeable toroidal component. These studies show that the stars more massive than $0.5M_{\odot}$ have magnetic fields with topologies similar to the hotter K or G stars which are predominantly generated in the area with the highest rate of differential rotation, located between the radiative zone and the convection zone, called tachocline. However the stars with lower masses with almost rigid rotation are also capable of sustaining a magnetic dynamo, but its operation is significantly different – it operates in the convection zone.

Close to M9 the red dwarfs are replaced by brown dwarfs at a mass about $0.07M_{\odot}$. The temperature in the core of these stars is not enough to sustain the hydrogen fusion and therefore there are no nuclear sources of energy. However, the transition from the main sequence dwarfs to brown dwarfs may not be accompanied by a considerable change of activity (Gershberg, 2002) as long as they also have

convective interior and considerable axial rotation, and these are among the main factors causing the generation of the magnetic fields in the small and middle mass stars and their chromospheric activity. The discovery of the X-ray radiation in the young brown dwarfs apparently supports this assumption (Neuhauser & Comeron, 2001).

High Speed Photometry

2.1 Brief overview of the common photo detectors used in Astronomy

The photo detectors for high speed photometry should have several important features. Being high speed photometry, it is intended to study the high frequency features of the light intensity variations of the astronomical objects, therefore the detector should have high temporal resolution. On the other hand, the light flux from these objects is very low and often require longer integration times, so to be able to reduce the integration time a high quantum efficiency is needed. These two conditions, the short integration time and the low brightness of the studied objects, lead to a low output levels of the signal, which in turn adds another requirement – low detector noise. In terms of these requirements, some of the most common photo detectors in astronomy are discussed below.

2.1.1 Charge-coupled devices

Since its invention in 1969 at Bell Labs, the Charge-coupled device (CCD) quickly became popular because of its versatility and features such as image capture. Nowadays there are many variants of the CCD design and new are being developed. Some of these designs are optimized for different applications but in general the CCDs are very reliable, simple and can be used in large arrays.

In the CCDs designed for image capturing, there is a photosensitive region, an epitaxial layer of silicon, and a transmission region made out of an insensitive to light shift register. The image is projected on the photosensitive region which is basically a capacitor array. This results in accumulation of electric charge in each capacitor proportional to the light intensity hitting it. Once the array has been exposed, a control circuit causes each capacitor to transfer its charge to its neighbor (operating as a shift register). The last capacitor in the array dumps its charge into an amplifier, which converts the charge into a voltage. After that the the charge is shifted again and the charge of the next capacitor is converted to voltage and so on. This

sequence of voltages can be digitized and stored in a memory and can be used to reconstruct the original image.

This charge transfer poses several issues with the CCDs. One of them is the readout which sometimes takes seconds and even minutes for the large arrays. The newer CCDs implement different readout processes like reading a specified part of the whole CCD image to speed up the reading. This way the readout time can reach milliseconds. Another issue with the CCDs is the charge not being fully transferred. The ratio of the transferred charge to the total charge is called Charge Transfer Efficiency (CTE). For the recent CCDs the CTE may exceed 99%. However, CTE depends on the readout speed, the faster the readout the lower the CTE. So, to achieve a high CTE it is necessary to slow down the readout process and the digitization rate, thus making CCDs not very good candidates for high speed photometry. However, there are several high-speed CCD based instruments like ULTRACAM (Dhillon et al., 2007). This instrument is a triple-beam CCD camera that can do up to 10 frames/second with 75% duty cycle and 40 frames/second with only 3% duty cycle in normal readout mode. To achieve higher performance several heuristic readout modes are implemented that allow ≈ 500 frames/second with 75% duty cycle. These modes increase immensely the complexity of the controller hardware and software, and the data produced is up to 50 GBytes per night, which makes it a very expensive instrument to build and to run, thus not very suitable for producing multiple copies needed for the synchronous network of telescopes.

CCDs are probably the most widely used photo detectors in astronomy, for they have many advantages, like high quantum efficiency, linearity and ability to register fine details, but their relatively slow readout speed makes them challenging to use for high speed photometry.

2.1.2 Avalanche photodiodes

An avalanche photodiode (APD) is a highly sensitive semiconductor device which operate using the photoelectric effect to convert light to electricity. APDs are photo detectors that provide a built-in gain through avalanche multiplication. Functionally they can be regarded as the semiconductor analog to photomultiplier tubes (See Section 2.1.3). Due to the impact ionization also known as avalanche effect, by applying a reverse bias voltage, APDs show an internal current gain effect. The typical reverse voltage of operation is around 100-200V and the gain is around 100, though some APDs are designed so that they allow greater voltage to be applied (more than 1500 V) before breakdown is reached and greater operating gain is

achieved (greater than 1000). In general, the higher the reverse voltage the higher the gain.

The gain varies strongly with the applied electric field strength, the temperature, and the doping profile. because of that it is necessary to control the reverse bias voltage to keep a stable gain. For even more stable gain a temperature control has to be utilized too.

However, for some applications this gain is not sufficient like the high speed photometry in astronomy. For that reason another type of APDs is developed with gain in the range of 10^5 to 10^6 , this APDs are usually dubbed single-photon avalanche diodes (SPAD) or Geiger-mode APDs in analogy with the Geiger counter. SPADs are also based on a p-n junction but it is reverse-biased at higher voltage V_a that exceeds breakdown voltage V_b of the junction. At this bias, the electric field is so high, higher than 3×10^5 V/cm, so that a single charge carrier injected into the depletion layer can trigger a self-sustaining avalanche. The current rises with a sub-nanosecond rise-time to a level in the milliampere range. If the primary carrier is photo-generated, the leading edge of the avalanche pulse marks, with picosecond time jitter, the arrival time of the detected photon (Zappa et al., 1996). This current continues until the avalanche is quenched by lowering down the bias voltage V_a below V_b . This way the lower electric field is no longer able to accelerate carriers to impact-ionize with lattice atoms, therefore the current ceases. In order to be able to detect another photon, the bias voltage must be raised again above V_b (Zappa et al., 1996). To achieve this an additional circuit is necessary. It needs to be triggered by the edge of the avalanche current and to drop the V_a . The simplest is the passive circuit which is a single resistor in series with the SPAD, so as the current rises the voltage on the resistor rises this way dropping the voltage on the SPAD. Once the voltage can not sustain the avalanche the current stops and the voltage on the resistor decreases, raising the voltage on the SPAD making it ready to be triggered again. More complicated active circuits can be used to quench the avalanche much faster this way reducing the time between the possible triggers.

In this mode of operation the intensity of the signal is estimated by counting the number of pulses within a defined time slot. However while the avalanche recovery circuit is quenching the avalanche and restoring the bias, the SPAD can not detect photons and if another photon reaches the sensor during this time it will not be counted. If the number of photons is such that the time between them is close to the avalanche recovery time, the missing counts are statistically significant and the increase of the count rate is not in linear relationship with the light level any more. If the light level is increased more the saturation will occur, the SPAD im-

mediately avalanches the moment the recovery circuit restores bias. This is the maximum count that that can be reached. So the maximum count is purely limited by the recovery time, however working close to the saturation maybe harmful to the device.

Besides photon-generated avalanches, the generation and recombination processes within the semiconductor can also trigger the avalanche process. The resulting average number of counts per second is called dark count rate. The dark count rate is the most important parameter in defining the noise of the APD. The higher the noise the lower the biased time, which in turn limits the time a real photon can be detected. Therefore, in order to work as a single-photon detector, the dark count rate should be low enough, well under a thousand counts per second.

Avalanche photodiodes are the most sensitive semiconductor light detectors. Their use in astronomy is increasing and for some application are already replacing the photo multiplier tubes.

2.1.3 Photo multiplier tubes

A photomultiplier tube (PMT) is a light detector built as vacuum tube consisting of an input window, a photocathode, focusing electrodes, several stage electron multiplier and an anode usually sealed into an evacuated glass tube. There are several possible layouts. The most common layouts are the linear type shown on Figure 2.1 and the circular-cage shown on Figure 2.2. They are extremely sensitive detectors of light in the ultraviolet, visible, and near-infrared ranges. These detectors have exceptionally high internal gain up to about 10^8 and individual photons can be detected when the incident flux of light is very low. These vacuum tubes are among the few that are not obsolete yet. The high gain, the low noise, the ultra-fast response and the large photo sensitive area (unlike APDs) has maintained their place in Astronomy and nuclear and particle physics.

The operation of the PMT can be describes as follows (see Figure 2.1): Light passes through the input window and excites the electrons in the photocathode and photoelectrons are emitted into the vacuum due to the external photoelectric effect, then photoelectrons are accelerated and focused by the focusing electrode onto the first dynode where the secondary electron emission takes pace and they are multiplied. The secondary emission is repeated at each of the successive dynodes. Each dynode is held at a more positive potential, by about 100 V or more, than the preceding one. This electric field accelerates the photoelectrons towards the next dynode, and

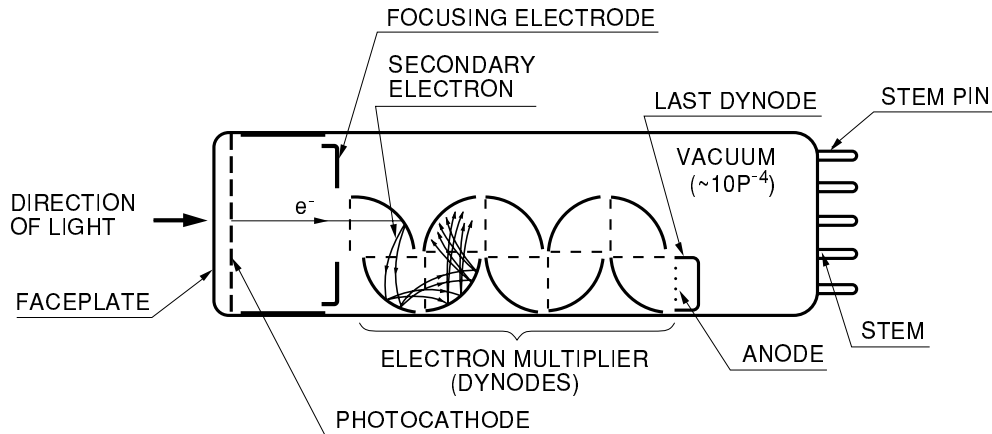


Figure 2.1. The internal structure of a linear photo multiplier tube (Hamamatsu, 2006)

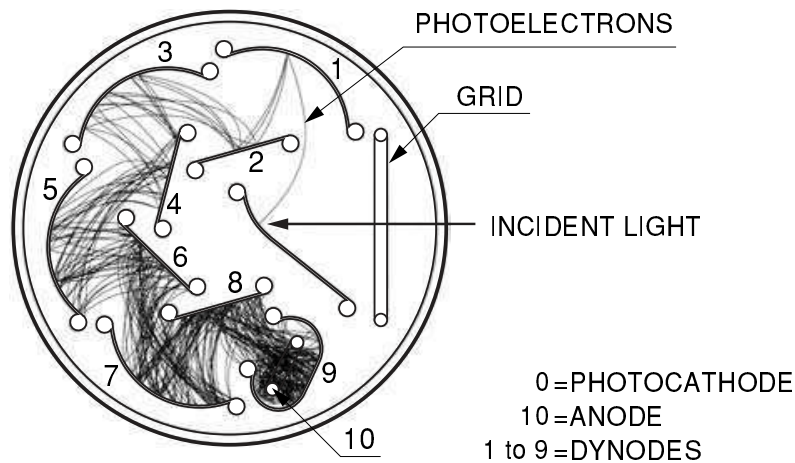


Figure 2.2. The internal structure of a circular-cage photo multiplier tube (Hamamatsu, 2006)

at the end the multiplied secondary electrons emitted from the last dynode reach the anode, where they are collected.

The PMT can operate in two modes: electric current measuring and Photon counting mode. In the electric current measuring mode the PMT produces an output current proportional to the flux of the input light. This mode is adequate for relatively high to moderate light levels. However if the light levels are very low the photon counting method is more adequate. This way each photon that managed to trigger emission of photoelectrons produces a negative pulse at the anode. By counting this pulses for a certain amount of time the level of the light can be estimated. However, false pulses can be triggered even if the PMT is in complete darkness, just like in the APDs. This can obscure the measurements but the level of dark counts per second here is usually around 100-150 or less than that at room temperature, and can be decreased significantly by cooling the PMT.

2.2 Choice of the detector

The discussed detectors have their strengths and weaknesses, but as mentioned before the most important features for this study are: the fast response time, the low noise level and the high sensitivity. A relative comparison between the described detectors is given in the Table 2.1. According to it the best choice is the photomultiplier tube. On the other hand the better sensitivity in the near ultraviolet makes the PMT even more preferable. Besides these quantitative advantages the PMT has one purely subjective advantage, namely a PMT based photometers are available on all of the telescopes planned to be used in this study.

Table 2.1. Detector comparison

Detector	Sensitivity	Response time	Noise level
CCD	high	slow	low
SPAD	high	fast	moderate
PMT	high	fast	low

2.3 Principles of photon counting with PMT

A diagram of PMT in photon counting mode is given on Figure 2.3. When a single photon strikes the photocathode of the PMT, single photoelectron is emitted. This photoelectron is multiplied by the cascade process of secondary emission through the dynodes (normally about 10^7 times). When the secondary electrons reach the anode, they produce output pulse that can be counted by the processing circuit. As mentioned before this operation is possible only in extremely low light levels.

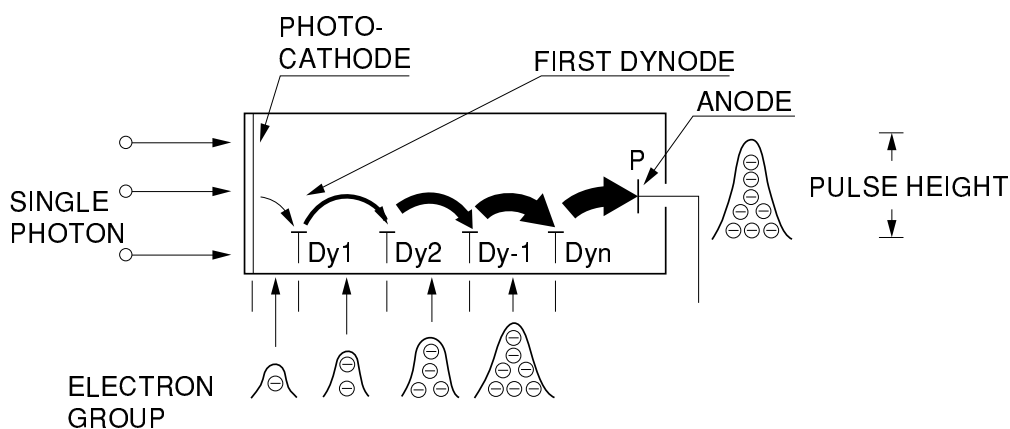


Figure 2.3. PMT in photon counting mode (Hamamatsu, 2006).

When the light level is very low and no more than two photoelectrons are emitted within the pulse width of the photomultiplier tube, the photon counting is possible. This light level is called “single photoelectron region”.

2.3.1 Efficiency and pulse heights

For the photon counting the quantum efficiency is an important parameter. It gives the probability of photoelectron emission when a single photon strikes the photocathode. In this single photoelectron region, when a photon hits the photocathode the number of emitted photoelectrons is either one or zero. The quantum efficiency is the ratio of the number of photoelectrons emitted from the photocathode to the number of incident photons per unit time. Sometimes the photoelectrons emitted from the photocathode (the primary electrons) deviate from the normal trajectories and are not collected by the first dynode, the probability that they will reach the first dynode and contribute to gain is known as collection efficiency. Thus, the overall efficiency in photon counting mode is given by the ratio of the number of counted pulses to the number of incident photons and is called detection efficiency or PMT counting efficiency. It is given by the relation:

$$DE = N_d/N_p = \eta \times \alpha \quad (2.1)$$

where N_d is the counted value, N_p is the number of photons, η is the quantum efficiency and α is the collection efficiency of the dynodes. It is worth noting that the detection efficiency greatly depends on the threshold level used in the discrimination process, which is described later.

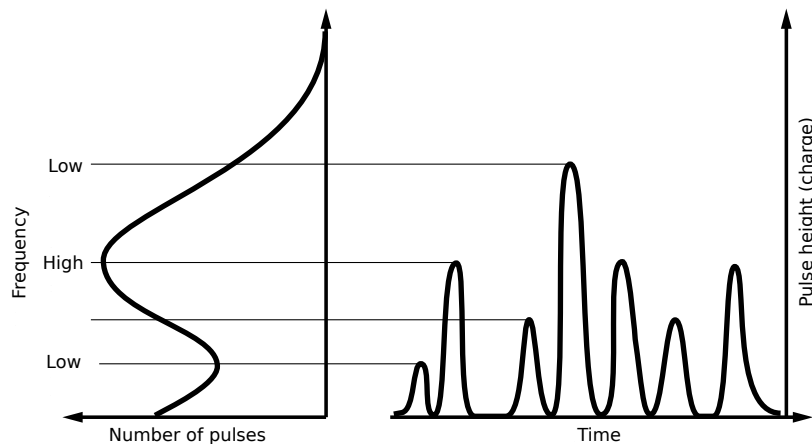


Figure 2.4. Typical pulse height distribution of a PMT and its output.

The number of secondary electrons released from the dynodes is not constant. They are several per primary electron with a broad probability roughly seen as a Poisson distribution. The average number of secondary electrons δ per primary electron corresponds to the multiplication factor of the dynode. This way if the PMT has n stages the average number of electrons at the photocathode is δ^n . As this photon count varies, each pulse at the anode exhibits a certain distribution in pulse height because of fluctuations in the secondary multiplication factor at each dynode which depends on the dynode position and electrons deviating from their trajectories. Figure 2.4 shows a histogram of PMT output pulse heights. It can be seen that a certain pulse height is most probable and the probability of lower or higher pulses decrease. However, the probability of low pulse heights increase as they get lower. There are output pulses even if no light falls on the PMT called dark current pulses or noise pulses. They mainly originate from the thermal electron emission at the photocathode and at the dynodes. The electrons from the dynodes are multiplied less than those from the photocathode and this explains the higher probability of the pulses with lower height. Figure 2.5 shows the pulse height distribution of the total signal (solid line) and of the dark current (dashed line). It can be seen that the lower the pulse height the more probably it is a dark current pulse. This way by discarding the pulses with lowest amplitudes one can increase the signal to noise ratio. This is achieved by setting a certain level of discrimination L (see Figure 2.5). On the other hand setting very high L the detection efficiency is decreased. Basically the best value of L is a matter of balance between the dark counts and the photon detection efficiency. As a rule of thumb, good value for L is at the left side (at the beginning) of the dark current plateau.

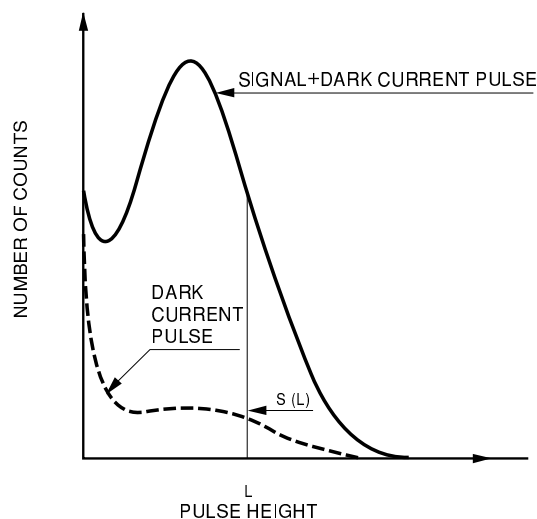


Figure 2.5. Typical pulse height distribution of a PMT (Hamamatsu, 2006).

2.3.2 Photon counting circuit

Figure 2.6 shows typical configuration of the circuit for photon counting. The pulses from the PMT are amplified to more manageable levels by the amplifier AMP. Then according to the discrimination level, the pulses lower than LLD threshold (and optionally higher than the ULD threshold) are discarded by the discriminator. Later the pulses are shaped and leveled so that they can be counted by a standard binary pulse counter, usually requiring Transistor-Transistor Logic (TTL) levels at the input.

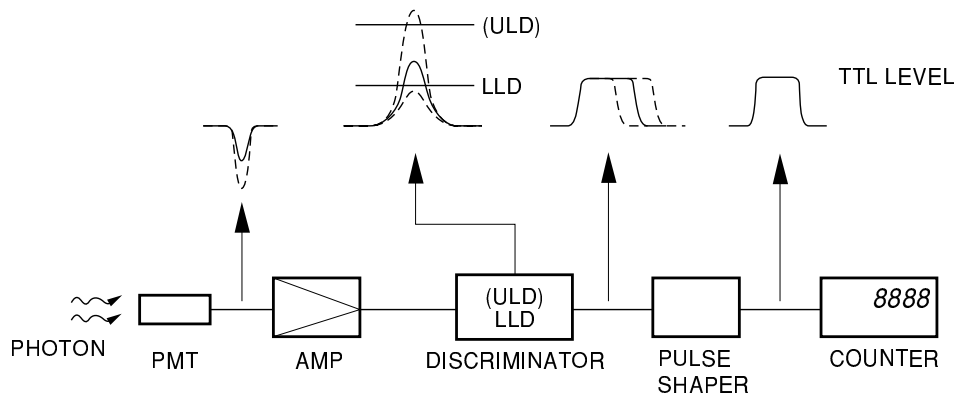


Figure 2.6. Example circuit configuration for photon counting with PMT(Hamamatsu, 2006)

Another important parameter of the PMT operation is the supply voltage V_s . The Figure 2.7 shows the curves of the noise, the signal-to-noise ratio and the signal by varying the PMT supply voltage V_s . This figure implies that the PMT should be operated in the range between the voltage V_0 at which the plateau region begins and the maximum supply voltage. These plots are called the plateau characteristics (Hamamatsu, 2006). It can also be seen that in the plateau range, the change in the number of counts depends less on the supply voltage V_s .

2.3.3 Linearity of the photon counting

The photon counting mode is linear over a wide range. The lower limit of linearity is determined by the number of dark current pulses, and the upper limit by the maximum count rate. The maximum count rate depends on the minimum time interval at which two pulse can be separated. The reciprocal of this time is the maximum count rate. However, since the photons usually arrive at random, the counted pulses may possibly overlap. Considering this probability of pulse overlapping (count error caused by pulse overlapping), the actual maximum count rate will be about one tenth of the calculated above (Hamamatsu, 2006). Here, if the true count rate is N ,

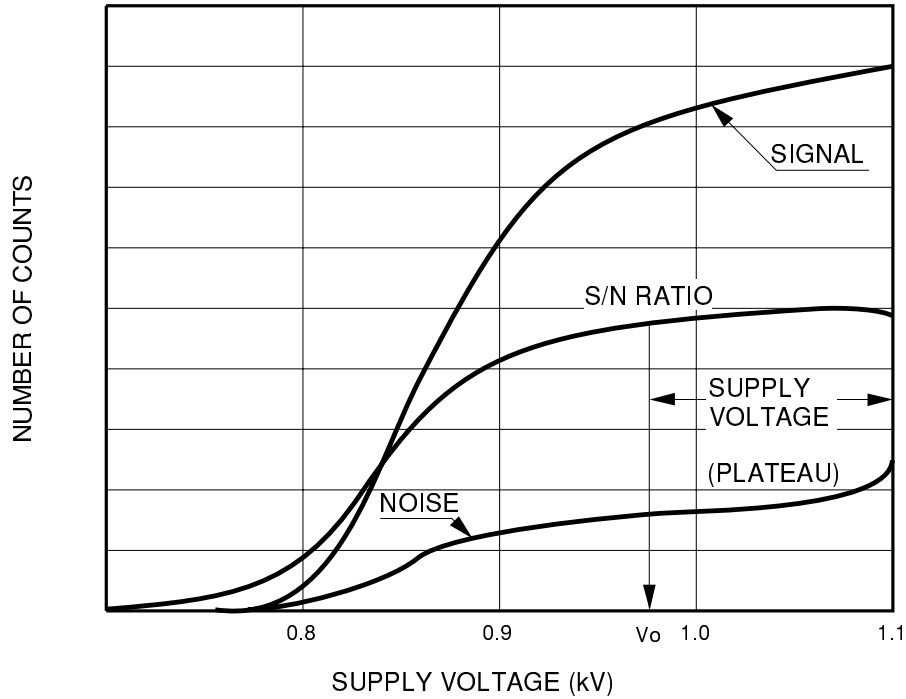


Figure 2.7. Plateau characteristics of a PMT (Hamamatsu, 2006)

the measured count rate is M and the time resolution is t , the loss of count rate $N - M$ can be expressed using the dead time Mt caused by pulse overlapping, as follows:

$$N - M = NMt \quad (2.2)$$

Thus the true count rate can be calculated:

$$N = \frac{M}{1 - Mt} \quad (2.3)$$

This formula can be used to correct the count error. According Hamamatsu (2006) if $t = 18ns$. The count error is corrected to within 1% even at a count rate exceeding $10^7 s^{-1}$. The photon counting mode of the PMT is very similar to the photon counting mode of the SPAD therefore this correction applies to the SPADs too.

2.3.4 Signal-to-noise ratio

As shown before the number of photoelectrons produced per unit time and also the number of secondary electrons produced, are determined by statistical probability of events which can be represented by a Poisson distribution, but this is not the only source of noise in the measurement. The signal itself is also noisy and one of the sources of noise in the signal is the earth atmosphere. Being impossible to isolate the signal from the background light at the time of measurement, makes

the background light the third source of noise. Therefore besides measuring the light from the object, the sky background light and the noise from the PMT (the dark counts) should also be measured. Using the three main components of noise: noise from the signal itself, noise from the background light and the noise from the PMT, the signal-to-noise ratio (SNR) can be estimated:

$$SNR = \frac{N_s \sqrt{T}}{\sqrt{N_s + 2(N_b + N_d)}} \quad (2.4)$$

where N_s is number of counts per second resulting from incident light, N_b is number of counts per second resulting from background light, N_d is the number of counts per second resulting from dark current and T is measurement duration (integration time) in seconds. Here the number of counts per second of the true signal N_s is obtained by subtracting $N_b + N_d$ from the total number of counts N_{ts} . As it can be seen there is no need to measure N_d and N_b separately to evaluate the SNR as they are used as a sum. It is easier to measure them as a sum by measuring the total sky background $N_{tb} = N_b + N_d$. Thus, only by using the measured values N_{ts} and N_{tb} the SNR can be estimated:

$$SNR = \frac{(N_{ts} - N_{tb}) \sqrt{T}}{\sqrt{N_{ts} + N_{tb}}} \quad (2.5)$$

Goals of the study

The flaring red dwarfs are the most numerous variable stars, and one of their important features is producing sporadic flares. They were detected within the whole wavelength range from hard X-ray to decimeters in the radio range. Sometimes during the flares, these stars show fine structures in the light curves like optical oscillations, which are not well studied but are believed to be associated with the magnetic loops on the surface of the star. Studying this fine features in the light curves will reveal some of the magnetic structures on the stellar surface and explain some of the processes taking place in the stellar chromospheres.

Two stars are selected for this study EV Lacertae and AD Leonis. Both of them are very active M dwarfs that show indication of a very complex surface magnetic topology and pretty high flare frequency. High frequency oscillations in the optical region were detected before only on EV Lacertae by Zhilyaev et al. (2000). What comes to AD Leonis there were only evidences for such in the radio wavelengths (Stepanov et al., 2001; Zaitsev et al., 2004) but no optical oscillations have been detected before.

These optical oscillations have very low amplitudes and they are very short, from several seconds to several dozens of seconds. Some of the other phenomena, like flickering, have similar characteristics, which makes them very difficult to observe and study. So the observation of these transient events require relatively high time resolution (in some cases <0.1 sec), to be able to resolve the fine structure, and being subtle require multi-telescope time synchronous simultaneous observations, to discard the features introduced by the local environment such as the earth atmosphere. On the other hand the flares are the most prominent in the shorter wavelengths such as near ultraviolet. Which makes this portion of the electromagnetic the best candidate for the study. To meet these somewhat contradicting requirements a new photometric equipment has been developed and described here (see Parts II and Appendices). These factors were considered in order to choose the photo detector. The main choices were charge-coupled device (CCD) and the photo-multiplier tube(PMT), as they were already available for use on most of the telescopes planned to be used in this network. Because of the high sensitivity especially in the Ultraviolet and the virtually unlimited time resolution the PMT is chosen. However, the system design allows another sensors that react to single photons

to be used without modification, such as avalanche photo diodes and multi-pixel photon counters.

Part II

Network–based Synchronous System for High Speed Photometry with Distant Telescopes

” *Starlight is falling on every square mile of the earth’s surface, and the best we can do at present is to gather up and concentrate the rays that strike at area 100 inches in diameter.*

— **George Ellery Hale**
Harpers magazine, April 1928

System overview

The system described here is designed to address the requirements of the observations of high frequency phenomena during stellar flares. It provides short integration time up to 0.001s. There is no dead time between the integrations. It provides high sensitivity in the ultraviolet band as it uses Photo Multiplier Tube (in photon counting mode) as a light detector. It also provides remote automated and centralized control of the photometric equipment in the network, as well as remote monitoring. It provides the ability to carry out simultaneous and synchronous observations on many telescopes of the same object synchronized to several microseconds. Some preliminary data analysis can be performed in real time while data is gathered and visually represented on the computer screen. It makes use of the GPS technology to achieve the accurate time synchronization between the observing sites and it allows instant exchange of the data between the sites through a computer network (Internet or local area network) while providing a mechanism for remote control.

Figure 4.1 shows a diagram of the system. The common use cases of the system are described below. The telescopes at Observatory A and Observatory B are observing the same object at precisely the same time, using their own GPS receivers for time synchronization. Both observations can be controlled from a single place either one of the observatories or a third place called Control site. Another scenario is when each observation is controlled locally but in a synchronous way (the individual measurements are always started at precisely the same time) and only the data is exchanged in real time between the sites participating in the network. Third scenario is when Observatory A and Observatory B have no network connection between them. In this case no real time data exchange is possible. However time synchronization is still possible by prenegotiating the parameters of the observations and the use of GPS at each site will provide the precise timing. The system can also be used as a standalone self-sufficient photometric system on a single site only.

The core of the system is the Photon Counting Module (PCM) and its accompanying software. The system provides tools to control the telescope, the filter wheel and the photometer. The components of the system are described in more details in the next section.

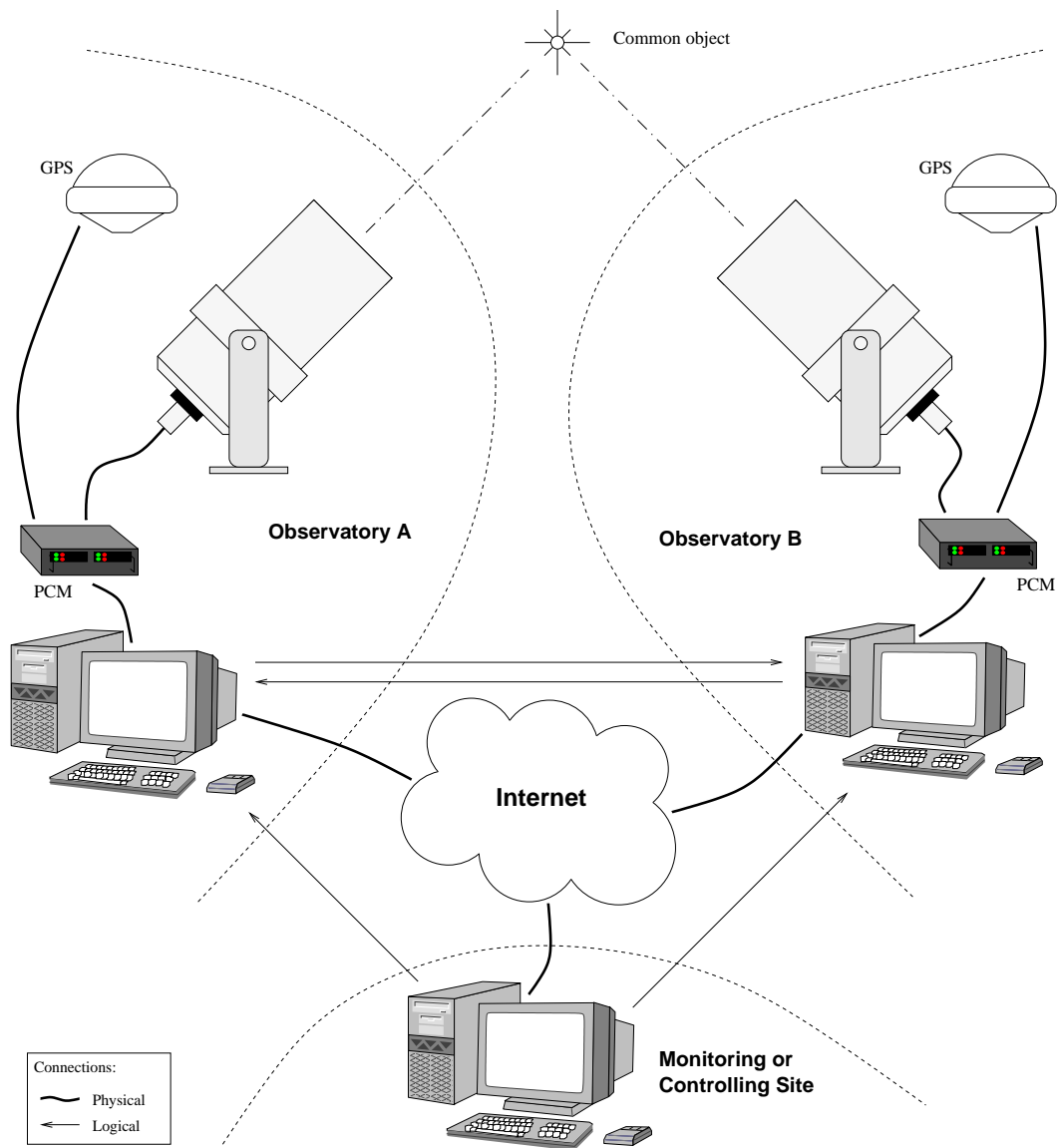


Figure 4.1. The architecture of the synchronous photometric network of telescopes

Hardware

5.1 Photon Counting Module

The Photon Counting Module (PCM) is the heart of the synchronous network of telescopes. It serves for light measurements and photometer control. It obtains the data, provides the accurate timing (synchronized with GPS), controls the filters and transfers the data to the computer. PCM can work with up to eight channel photometers. The specifications of PCM are given in Table 5.1 and its block diagram is shown on Figure 5.1.

Table 5.1. Specifications of The Photon Counting Module

Min. integration time	0.01s (0.001s with USB)
Max. integration time	655.35s
Integration time increment	0.01s (0.001s with USB)
Resolution of the internal RTC	0.001s
Time synchronization drift (with GPS)	$< \pm 2\mu\text{s}$
Time adjustment resolution	$0.1\ \mu\text{s}$
Counter max. value (per channel)	2^{24}
Input signal level	TTL or ECL
Communication interface	RS-232 at 115,2 kbps or USB
Power supply	AC/DC 9 – 24V 300mA

The PCM is synchronized with the GPS time by the Synchronization Unit. It controls the Photon Counters and strobes them precisely for each integration. The Control Unit is responsible for gathering the observational data from the Photon Counters, controlling the filter revolver, initializing the Timing Unit and sending the data to the computer through the Communication Unit. Further data transfer is carried out on a software level on the computer connected to PCM. Currently two versions of PCM are built. One five channel version is built for the AZT-11 telescope at Crimean Astrophysical observatory. And four 2 channel versions, two working on the 60cm Cassegrain telescopes in Belogradchik and Rozhen Observatories and two on the 2m Ritchey-Cretien telescopes in NAO Rozhen and Terskol Observatory. The user's guides of the PCM are provided in Appendix I and Appendix J.

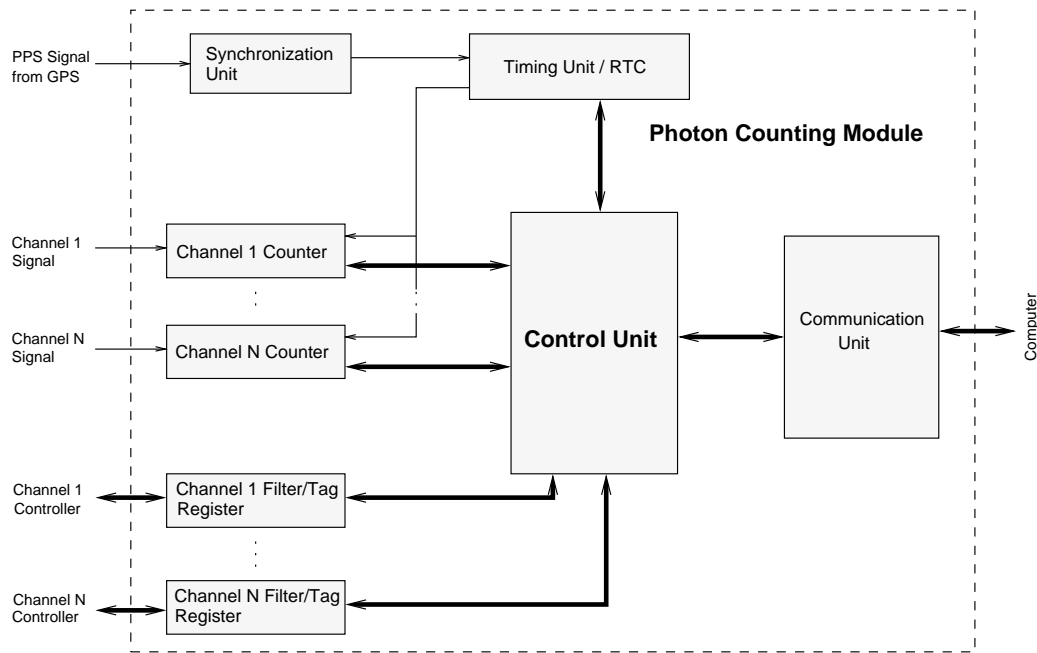


Figure 5.1. Block diagram of the Photon Counting Module

5.1.1 Synchronization Unit and Real Time Clock

Each measurement is tagged with an accurate time stamp provided by the Real Time Clock (RTC). The RTC itself is synchronized using the PPS (pulse per second) signal from the GPS receiver. The PPS accuracy for the used Accutime 2000 GPS receiver by Trimble is supposed to be $< \pm 100ns$ when doing over-determined fixes (Trimble Ltd., 2000). For that reason The internal clock resolution of the system is chosen to be $100ns$. And the synchronization is achieved by adding or subtracting $100ns$ quanta to the RTC. This time quantum value is small enough to provide short term stability of the photon counts of ± 2 counts/sec as the photon pulse length provided by the Photometer is $T_p \approx 40ns$.

The resolution of the time stamps provided by the RTC is $0.001s$, but this is not an issue as each measurement series are started precisely at a round second. This ensures that the accuracy of this time stamp is better than the designed long term stability of $< \pm 2\mu s$. However the tests performed show that the PCM's RTC compared to to GPS's RTC never exceeds $600ns$. Illustration of this is provided on Figure 7.1. Taking in to account that the PPS offset of the Acutime 2000 Receiver is $< \pm 100ns$, this yields total RTC accuracy of $\pm 700ns$ which is well in the design tolerance of $\pm 2\mu s$.

5.1.2 Channel Counters and Filter/Tag Registers

Each channel consists of a counter and a filter/tag registers. Each Channel counter is organized as a 16bit hardware counter which value is read by the Control Unit once every 1ms and the value is added to the accumulator register of 24bits size. The hardware counter is a free running counter and its value is never cleared and it is never stopped. All the channel counter values are read in precisely the same time. The control unit reads this value and subtracts the previous value to get the actual value of the counter and this value is added to the Accumulator register. The total value accumulated for a given period of time in the Channel accumulator is the total count of photons registered.

This counter design provides several benefits over the conventional design. One of them is that the dead time between measurements is 0. Which makes time synchronization of the integrations a desired side effect. Second, one can add safely several (let us say n) measurements of k seconds each together. The result will be precisely what what one would measure if he had made one measurement of nk seconds and the time synchronization will be preserved too.

Each Channel has a filter/tag register. It is used for controlling the filter wheel and Tag the object that is observed. By writing the Number of the filter in this register the PCM issues a command to the Filter Tag Control Unit (FTC) (see Appendix K and Appendix L) to set the desired filter. Reading this register will provide the actual value of the filter and the Tag that is currently set. The tag is a short abbreviation to give the observer an idea what is measured, like variable star (Var), comparison star (Comp), dark current (Dark), sky background (H) etc. It behaves the same way as for the filter, writing the number of the tag to this register, sets the desired tag in FTC.

5.1.3 Control and Communication Units

The PCM is built around the PIC18F452 micro-controller manufactured by Microchip. So the organization and control of the subsystems in PCM is done by the firmware running on this controller. In addition to these tasks this unit provides the communication with the controlling computer. The communication interface is RS-232 or USB, but currently only RS-232 Devices are used. For receiving commands and data transfer PCM uses PHOT protocol. This is a binary protocol optimized and designed specially to provide the functionality of PCM. Full description of the protocol is given in Appendix G.

5.2 Filter & Tag Control Unit

Filter and Tag Control Unit (FTC) is a remote control for the PCM and the filter wheel. It is located at the telescope and gives the observer quick and easy way to start/stop measurements, change filters and tags. It has a display to give an instant feedback of the actions taken by the operator and to provide information about the current state of the system.

Two versions of the FTC are developed. A detailed descriptions of the two versions (FTC01 and FTC02) are provided in Appendix K and Appendix L respectively.

The communication between FTC and PCM is done through a custom interface and protocol. A detailed description of which is available in Appendix M.

Software

The software is based on a client-server architecture which allows the system to be controlled or monitored from a distance, and also allows real time data exchange between the observing sites. The software consists of four different modules: `phot-srv` – server module, which must run on the computer physically connected to the hardware of the photometric system (PCM); `photclient` – the client software, which can be run on any site with a network connection to the site where the server is running; `devsim` – hardware simulation, which can be run everywhere for training, demonstration, software development or troubleshooting; and `photview` – an application used to visualize and edit already obtained data.

The communication between the server and the client is implemented using Transmission Control Protocol over Internet Protocol (TCP/IP). The connection is console oriented, so that many standard programs can be used such as `telnet` to send commands and receive the results of their execution. However the provided client software (`photclient`) uses Graphical User Interface and the user is not supposed to type commands.

6.1 Server Software: `photosrv`

The server software is designed to run on UNIX or UNIX-like operating systems. It is coded in C programming language using POSIX application programming interface. The data exchange protocol over the network is text-based, which makes it easy to use without the client part of the software. For example one can simply type commands and get the results using the standard `telnet` utility provided by many operating systems.

The server supports two types of incoming connections – Read-only (RO) and Read/Write(RW). The RW connections provide full control of the system, while the RO connections serve exclusively for monitoring and data collection. Only one RW connection is accepted at a time, whereas there can be more than one RO connections.

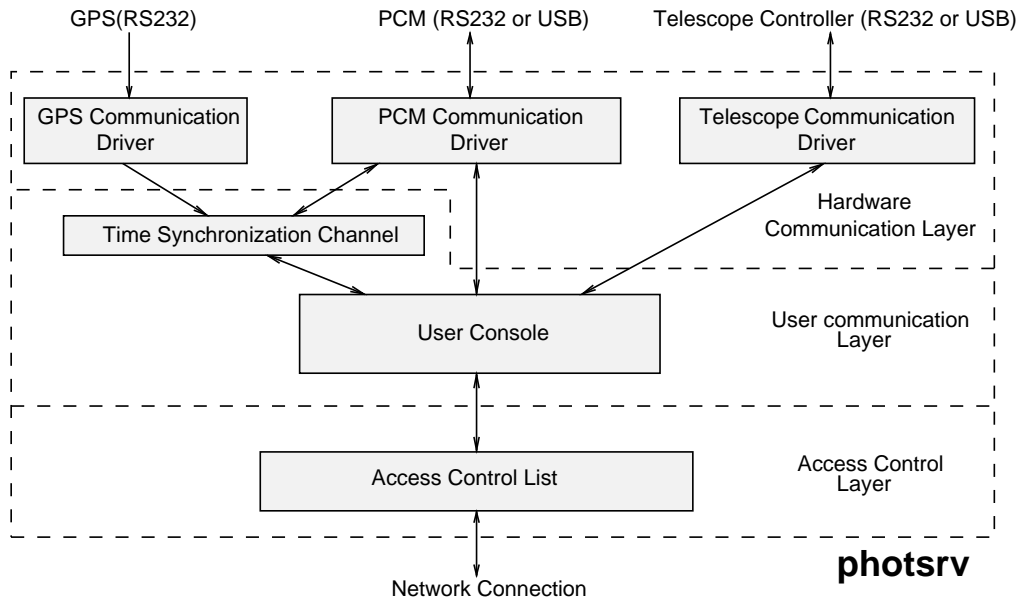


Figure 6.1. Block diagram of the server software: photsrv

The server software has three main layers (Figure 6.1): Access Control Layer, User Communication Layer and Hardware Communication Layer.

6.1.1 Access Control Layer

Photsrv uses access control list (ACL) with user specified rules to grant or refuse different types of connections to different users and sites. In addition, the maximum number of concurrent connections can be limited. The control can be done by IP address of the client computer or by its network address. Types of access are: read-only – used to obtain the data in real time; read-write – used to have full control over the system; and deny – denies access to the specified computer or network. Full specification of ACLs can be found in Appendix E.

6.1.2 User Communication Layer

This layer is responsible for parsing and dispatching the user commands to the appropriate driver in the Hardware Communication Layer and for delivering the results back to the user according to the PHOT console protocol (Appendix F). A Time Synchronization channel is implemented in this layer between the PCM driver and the GPS driver in order to ensure independence of the PCM firmware from the specific communication protocol of the GPS receiver.

6.1.3 Hardware Communication Layer

This layer includes drivers for communication with the hardware components of the photometric system – GPS driver, PCM driver and Telescope driver. More details are provided below.

GPS Communication Driver

This Driver is used for communication with the GPS receiver, it is used to access the receiver status number of satellites used and various information provided by the receiver, but its main purpose is to get the accurate time and the accurate time stamp of each Pulse Per Second (PPS) signal used by PCM for the precise time synchronization. Currently only Trimble Accutime 2000 GPS Smart Antenna is supported by the driver, but if necessary support for more GPS receivers can be added.

PCM Communication Driver

This driver implements the PHOT protocol described in Appendix G to communicate with the PCM device. It also implements the time synchronization with the GPS using a Proportional Integral (PI) controller described in section 6.1.4

Telescope Communication Driver

The last version of photsrv can directly communicate with and control the telescope. It can slew the telescope to a desired object or to desired coordinates. This is used to automate the observations with minimal input from the observer. For the time being two telescope control protocols are implemented, ASCOL protocol used by the 2m Ritchey-Cretien Coude at NAO Rozhen and Celestron Nexstar protocol used by a variety of amateur telescope mounts.

6.1.4 Time Synchronization

The PCM real time clock uses the clock pulses from the oscillator. But the oscillator frequency is not stable enough. It changes with the temperature, therefore continuous synchronization is needed. The RTC works according to Equation 6.1, where T_{tick} is the time resolution of the RTC, F_{osc} is the supposed frequency of

the oscillator and K is a constant so that $T_{tick} = \frac{K}{F_{osc}}$, However F_{osc} is not precise and its stability depends on the temperature, that is why the term n is introduced as a correction value, which is adjusted constantly to ensure the desired precision of the RTC timer.

$$T_{tick} = \frac{K + n}{F_{osc}} \quad (6.1)$$

The correction value is determined using a Proportional Integral Derivative (PID) controller implemented in photsrv. The common form of the controller is given by Equation 6.2.

$$MV(t) = K_p e(t) + K_i \int_0^t e(\tau) d\tau + K_d \frac{d}{dt} e(t) \quad (6.2)$$

Here $MV(t) = \frac{n(t)}{F_{osc}}$ is the manipulated variable, $e(t)$ is the offset from the desired value, in this case the offset of PCM time from the GPS time $T_{offset} = T_{GPS} - T_{PCM}$ at the given time, t is the integration period, and K_p , K_i and K_d are proportional, integral and derivative gains.

Based on the tests performed the derivative term can be dropped by setting $K_d = 0$. This way in photsrv a Proportional Integral (PI) controller is used. Also this form of the controller is not very convenient for this application as the time smoothness should be ensured, no two consecutive seconds should differ with more than $1/F_{osc}$, which is $100ns$ in this case. So the Equation 6.2 is slightly changed to take the form of Equation 6.3

$$MV(t) = K_p \left(e(t) + \frac{1}{T_i} \int_0^t e(\tau) d\tau \right) \quad (6.3)$$

Here $T_i = \frac{K_p}{K_i}$ is the integral time, this value has a physical meaning, which is that in the ideal case all errors accumulated within the integration period t should be fully compensated in time T_i . This makes possible to ensure the desired smoothness of time by adjusting T_i every integration period.

To adjust time on the PCM a command *adjrt* is used which accepts as a parameter the value of $MV(t)^{-1}$ calculated as shown above. To get an accurate value of the time offset T_{offset} the command *rdrt2* is used. These commands are to be used

by the photsrv and the user does not have to take care of the time synchronization. For detailed description of the commands see Appendix F and Appendix G.

Using this algorithm the offset of PCM time from the GPS time T_{offset} is never observed to exceed $\pm 0.6\mu s$ as illustrated on Figure 7.1.

6.2 Client Software: photclient

The client software runs on a variety of operating systems including MS Windows and a variety of UNIX clones like Linux, Solaris, FreeBSD etc. It is implemented in Perl programming language using Perl/Tk toolkit to build the graphical user interface. The client is used for system control, monitoring, data collection and real time data visualization. A screen shot of photclient is shown on Figure 6.2. Photclient can operate in two modes – manual mode, in which every measurement cycle is configured, started and stopped manually, and batch mode (Figure 6.3), which enables the observer to make a plan of the whole observation and let the system carry it out in automatic mode without user interaction. These two modes are available only for the read-write connections as they allow full control of the system.

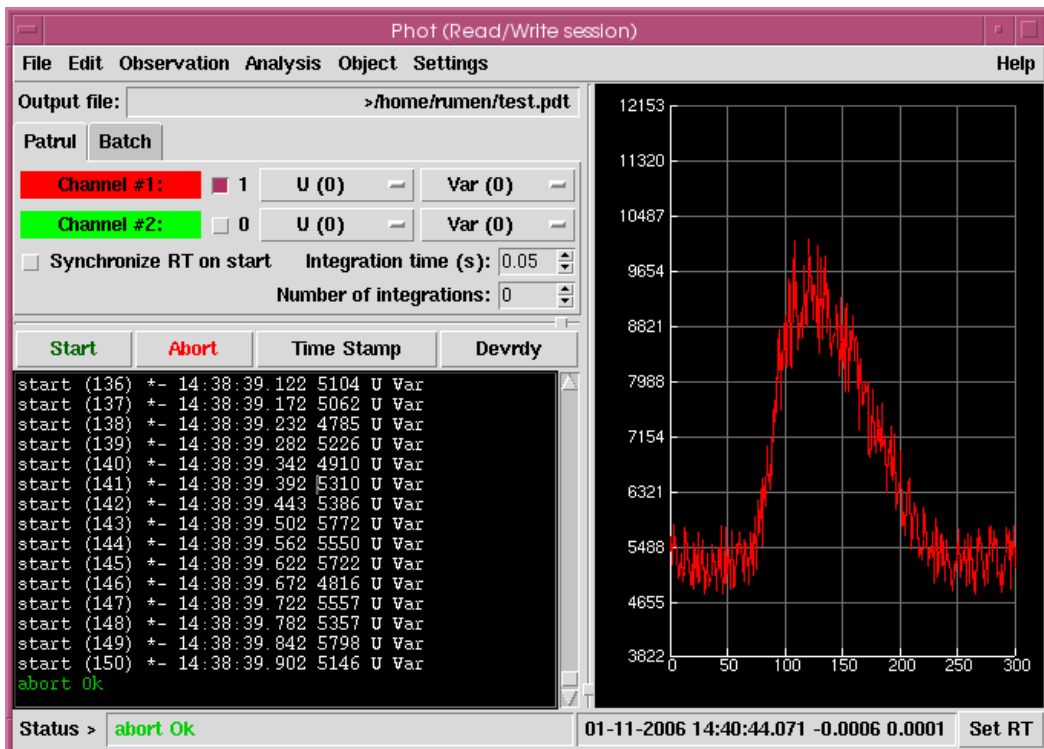


Figure 6.2. User interface of the client software running with devsim

For running photclient in batch mode the user must create a script as described in Appendix H. An example script is given below.

```
# UBV 10x1s, St1, Var, H (3 times).
integr 1 10

.repeat 3
    # filter U
    setft U St1
    .message Point the telescope to "St1"
    start

    setft U Var
    .messageb Point the telescope to "Var"
    start

    setft U H
    .messageb Point the telescope to "H"
    start

    # filter B
    setft B St1
    .messageb Point the telescope to "St1"
    start

    setft B Var
    .messageb Point the telescope to "Var"
    start

    setft B H
    .messageb Point the telescope to "H"
    start

    #filter V
    setft V St1
    .messageb Point the telescope to "St1"
    start

    setft V Var
    .messageb Point the telescope to "Var"
```

```

start

setft V H
.messageb Point the telescope to "H"
start

.end

```

Photclient has some useful additional features like monitoring of the GPS receiver status, different modes for data visualization (as a raw data graph or a Fourier spectrogram), support of user defined object database, displaying object hour angle and elevation and many others.

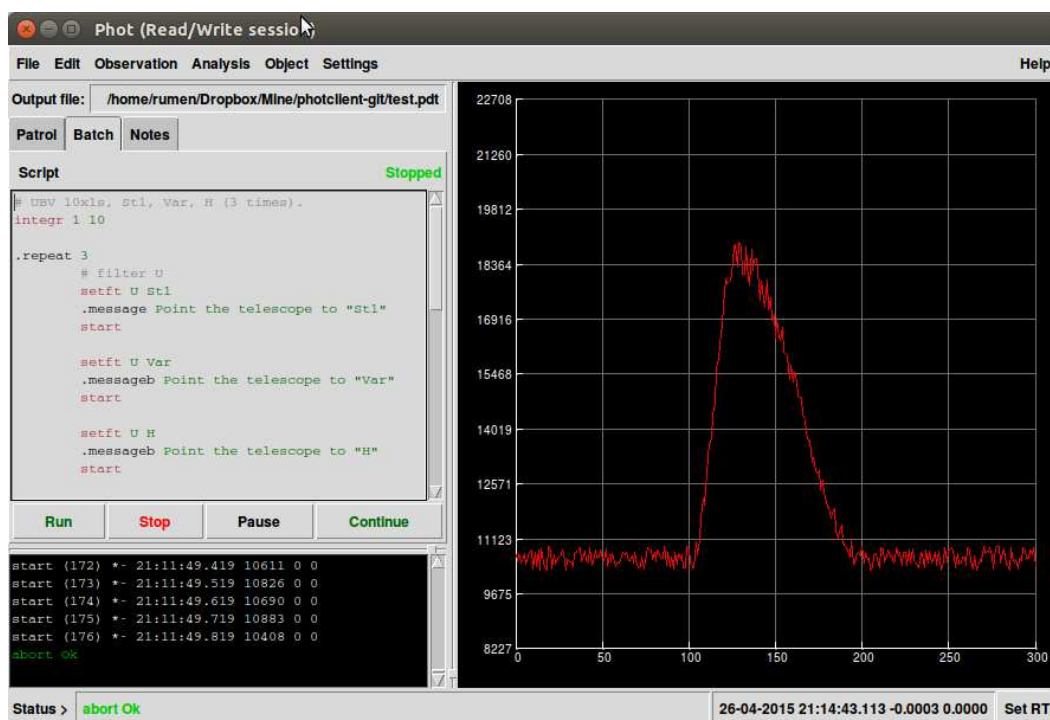


Figure 6.3. User interface of the client software running in batch mode with devsim

6.3 Data viewer: photview

This application is used for visualization and simple editing of the already acquired data. The user can copy some parts of the data and save them in a different file. All the measurements are presented in the top left panel (see Figure 6.4) along with some data like start time, photometric channels used and the integration time.

If the user selects one of them the data will be visualized as text in the bottom panel and as a graph for the selected channel in the right panel. If one clicks on the

graph the data point will be highlighted in the text representation of the data and vice versa.

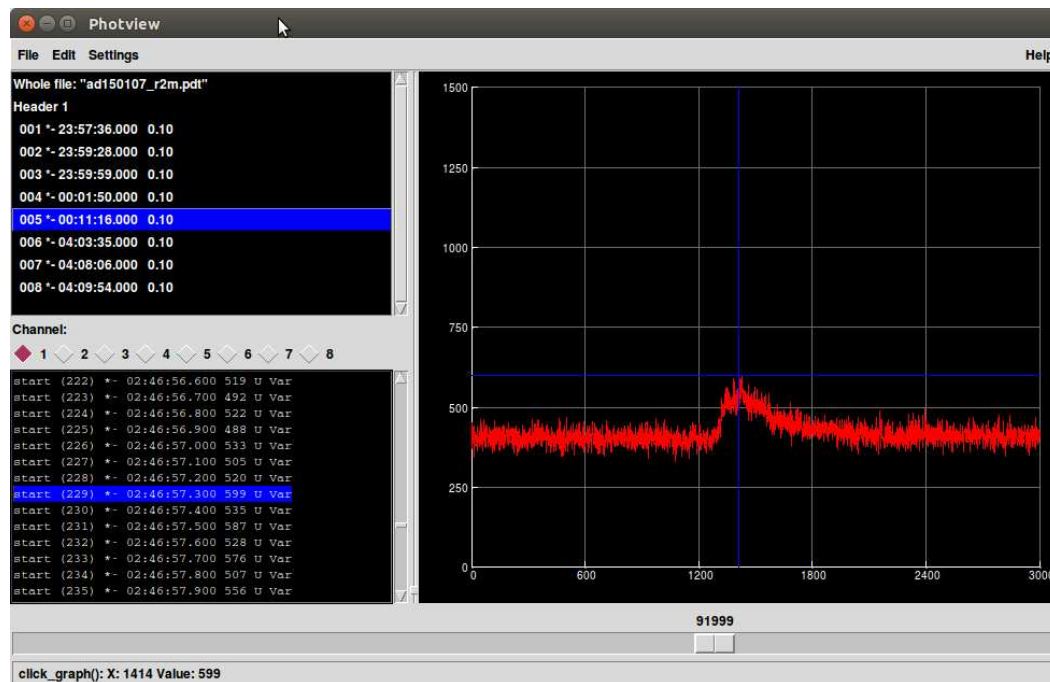


Figure 6.4. User interface of the data viewer – photview, showing real flare of AD Leonis observed at NAO Rozhen on January 16, 2007

6.4 PCM Simulator: devsim

The PCM hardware simulator is based on the source code of the PCM firmware. It can be used as a debugging tool and as a training tool for users without the need for access to the real system. The software can simulate a variable star that produces flares on a regular basis, it can also simulate comparison star, dark current, sky background etc. The level of noise in the simulated data is also configurable. Full documentation of the device simulator is available in Appendix A and Appendix B.

Tests and First Light

The first real tests of the system were performed at the National Observatory Rozhen on the 2-meter telescope during the synchronous observational campaign in September 2004 in collaboration with Terskol, Crimean and Stefanion observatories, in Russia, Ukraine and Greece respectively. PCM was attached to the Bulgarian-Ukrainian Photometer described in (Antov et al., 2001). Some of the flares observed during this campaign are analyzed and the results are given in Chapter 8.

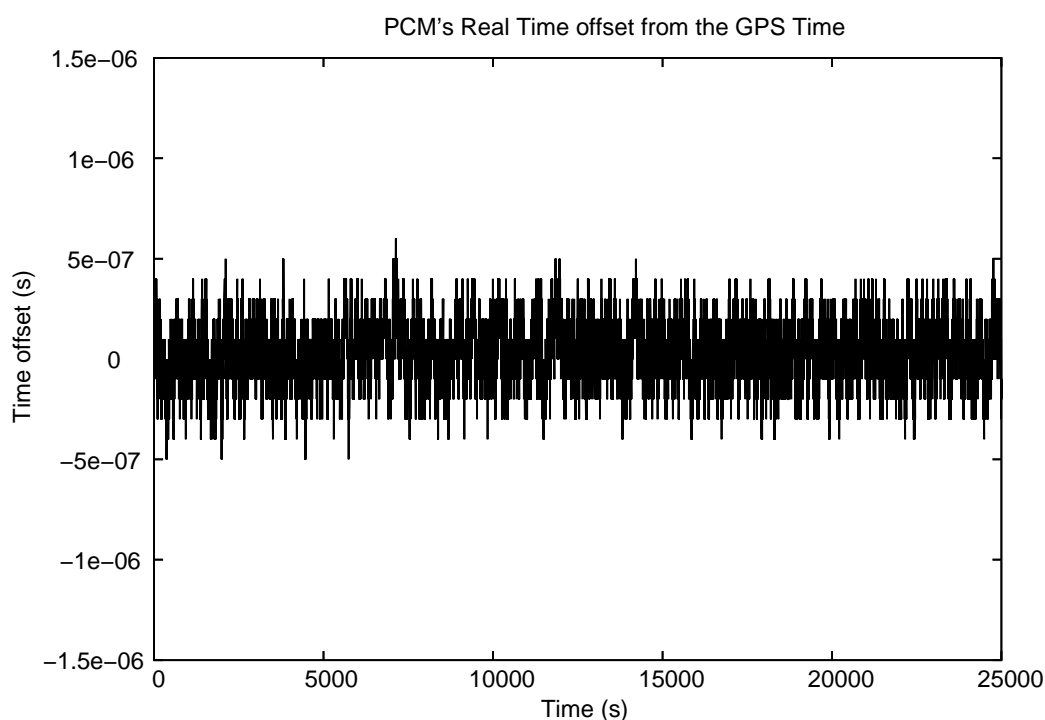


Figure 7.1. PCM's real time synchronization drift measured each second for 25000 seconds (about 7 hours).

All the data about AD Leonis used in Chapter 9 is obtained with with the described system and Figures 9.5 and 9.10 are a good illustration of the concept behind the synchronous observations. Figure 9.5 shows a good correlation of the light curves. It can be seen that the fluctuations superimposed on the flare, observed on the two telescopes have a high degree of coincidence in their structure. This is an empirical confirmation that the features observed during this flare are results of real events taking place on the star triggered by the flare, or they are direct result of the flare

itself. On the other hand Figure 9.10 shows that the light curves start to diverge on the descending slope of the flare, probably due to a transient decrease of the atmospheric transparency on one of the sites, therefore the dip on the descending slope observed on one of the telescopes is not a real feature of the flare.

Figure 7.1 shows the synchronization drift of the PCM time compared to the GPS time for an uninterrupted period of about 7 hours, measured every second. It is worth noting that the time difference does not exceed $0.6\mu\text{sec}$, which is well in the specified $1\mu\text{sec}$ limit. Multiple tests have been performed in different conditions and the results are consistent. Once the GPS is in high precision mode and doing over-determined fixes (Trimble Ltd., 2000), the time difference rarely exceeds $0.5\mu\text{sec}$ and never $0.6\mu\text{sec}$.

Part III

Study of the Flares of EV Lacertae and AD Leonis

” *Across the sea of space, the stars are other
suns.*

— **Carl Sagan**
American astronomer

Synchronous Observations of EV Lacertae

EV Lacertae is a red dwarf star with spectral type M3.5 (Osten et al., 2005). It is one of the brightest flare stars with $V = 10.26^m$ (Gliese & Jahreiss, 1991). The star has a $V \sin i = 4.5 \text{ km/s}$ (Johns-Krull & Valenti, 1996), which is relatively high for an M dwarf. The high activity of EV Lacertae supposes that the star has a strong magnetic field. Taking into account the radius of the star $R \approx 0.36 R_{\odot}$ (Chabrier & Baraffe, 1997), the rotational period of EV Lac is about 4 days, which is supported by the photometric period of 4.4 days determined by Pettersen & Sandmann (1992). The mass of the star is $M = 0.35 M_{\odot}$ (Phan-Bao et al., 2006).

Some studies from the 1970s and 1980s suggest that EV Lacerta has an unresolved companion. Rojzman (1984) suggested an eclipsing companion because there was no correlation between the flare frequency and the long term photometric light curve. Another study suggests that its mass is likely between 2 and 4 Jupiter masses, a period of 45 years and a high orbital eccentricity ($e \approx 0.5$) (Lippincott, 1983). An earlier astrometric study carried out by van de Kamp & Worth (1972) suggests way more massive companion with orbital period of 28.9 years and mass between 0.01 and $0.03 M_{\odot}$. So the question about the companion of EV Lacertae remains open.

High frequency optical oscillations during flares of EV Lacertae are reported before by Zhilyaev et al. (2000). At an early stage of the unfolding of the flare, an oscillation with a period of 25.7 seconds is reported and around its maximum an oscillation with a period of 12.8 seconds is reported. These observations were interpreted by Kouprianova et al. (2004) and they concluded that the source of such oscillations is located at the magnetic loop footpoint. The pulsations are determined by modulation of the flux of energetic particles descending along a loop with fast magnetoacoustic oscillations. Within the framework of the model, Kouprianova et al. (2004) have estimated that the loop height should be approximately 10^{10} cm , which is approximately $0.4 R_{*}$, the plasma density is approximately $2 \times 10^{11} \text{ cm}^{-3}$, the plasma temperature is approximately $4 \times 10^7 \text{ K}$ and magnetic field strength is 320 G.

8.1 Observations

EV Lacertae has declination of about $+44^\circ$ and it can be monitored continuously for up to 8 hours during autumn nights.

The Synchronous Network of Telescopes, involving telescopes at four observatories in Ukraine, Russia, Greece and Bulgaria is used to study the fast variability of active stars with high time resolution. The flare star EV Lac is observed from four separate sites for 14 nights in September 2004, using the following instruments: the 2-m Ritchey-Chretien and the 60-cm Cassegrain telescopes at Peak Terskol (North Caucasus) with a high-speed two-channel UBVR photometer (Zhilyaev et al., 1992), the 30-inch telescope at Stephanion Observatory in Greece, equipped with a single-channel photometer with digitized readings in the U band (Mavridis et al., 1982), the 1.25-m reflector AZT-11 at the Crimean Astrophysical Observatory with a five channel UBVR photometer-polarimeter (Kalmin & Shakhovskoy, 1995), the 2-m Ritchey-Chretien telescope at the Rozhen Observatory with the Bulgarian Ukrainian Universal Photometer (Antov et al., 2001) and the prototype of the PCM (see Chapter 5 and Appendix I) and the 60-cm Cassegrain telescope at the Belogradchik Observatory with a single-channel UBVR photon-counting photometer (Antov & Konstantinova–Antova, 1995).

The typical integration time was 0.1 s. The sky background was subtracted from all the data. The basic photometric package of the Crimean Astrophysical Observatory was used to transform the instrumental magnitudes to the standard UBVR system. It is worth mentioning that the prototype of the Photon Counting Module and the photometric system described in Part II is used for the first time for real scientific data acquisition in this observational campaign at the 2-m telescope at NAO-Rozhen.

8.2 Methods

To increase the signal-to-noise ratio, digital filtering of the available photometric data is performed. Kaiser convolution is used to obtain a low-frequency outburst light curve from the sets of EV Lacertae data and a moving-average is used to suppress high-frequency noises. Detailed description is available in Zhilyaev et al. (2000). Filtering in the frequency domain can be performed by convolving the series $n(i)$ with the pulse response characteristic coefficients of the filter $h(i)$:

$$n_f(k) = \sum_{i=-l}^l h(i)n(k-i). \quad (8.1)$$

The filter coefficients are

$$h(k) = h(-k) = \frac{\sin(\pi\nu_c k)}{\pi k} \cdot \frac{I_0(\eta\sqrt{1 - (k/l)^2})}{I_0(\eta)}, \quad (8.2)$$

where $I_0(x)$ is the modified Bessel function of the zero order, η is the parameter that enters the filter's model, l the number of coefficient pairs of the filter. Three basic input parameters, the pass band ν_c , the width of transition band and the stop-band attenuation of the filter in the decibel scale, completely determine quantities η , l and the filter as a whole (for more details see Kaiser & Reed, 1977). This way with a Kaiser filter one can set limits on the signal that would have been aliased through the side lobes of the stop-band of the filter. The filtering procedure decreases covariance of the noise proportionally to the pass band of the filter.

8.3 Search for High-frequency optical oscillations during flares

More than a dozen flare events have been registered in UBVR bands during the September 2004 campaign, but only two flares are discussed here. These events were registered on more than one telescope with time synchronization better than 0.1 s.

8.3.1 The flare on September 14, 2004

Figure 8.1 shows a portion of the outburst light curves of EV Lac (upper panel) and the high-pass filtered light curves of the flare (lower panel) registered during the synchronized observations from three telescopes at the Crimean and at the Terskol observatories on September 14, 2004. The light curves in the U band are not smoothed, but only normalized to a unit intensity. There is only weak indication of HFO presence in the original photometric data. But the lower panel clearly shows presence of HFO after an appropriate high-pass digital filtering. The numerical values for the Kaiser filter used were: the cutoff frequency $f = 0.167 Hz$, the width of transition band $\Delta f = 0.1 Hz$ and the stop band attenuation is 50 dB. A moving-average filter with an effective bandwidth of 1.5 s is also applied in order to reduce the noise fluctuations. As can be seen there is an obvious correlation between the data obtained by the different instruments at the three sites, which supports the assumption that the oscillations are a real feature of this flare.

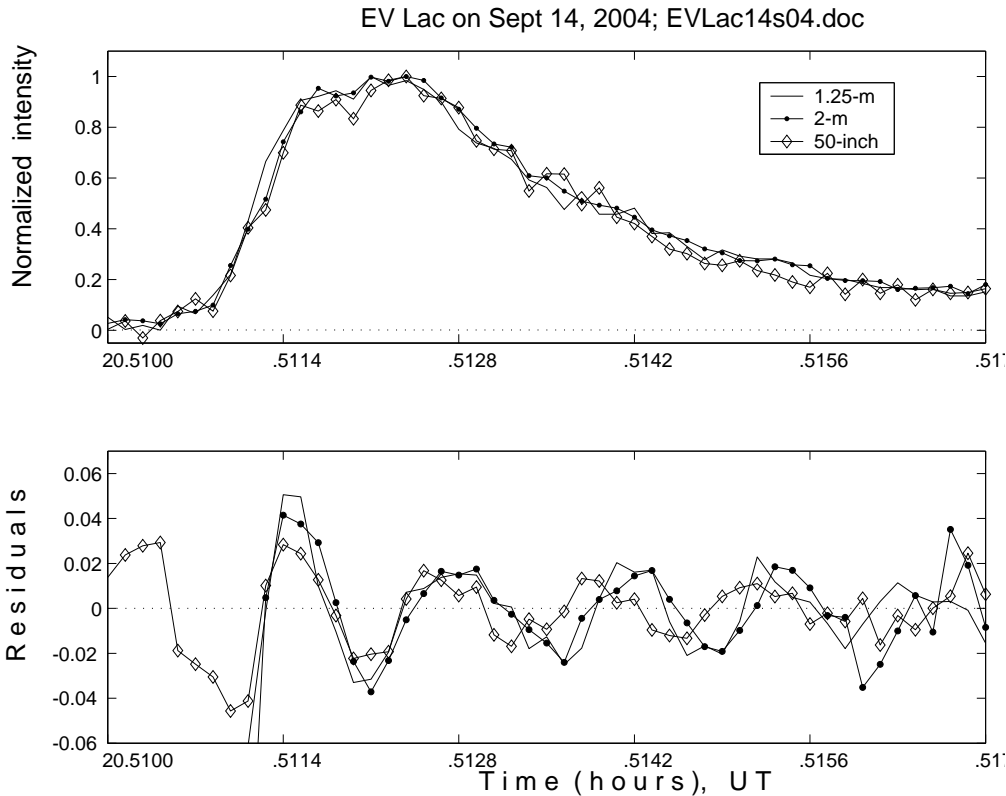


Figure 8.1. A flare event of EV Lac, September 14, 2004, 20:31 UT (max), the U band, based on the multi-site synchronous observations with the Terskol 2-m, Crimean 50-inch and 1.25-m telescopes (upper panel). The lower panel shows HFO revealed after the high-pass digital filtering.

Figure 8.2 shows the light curves in the U and I bands and their least-square polynomial fits. The polynomial fit is considered to be a representative of the light curve of the flare. Thus the residuals are analyzed in order to detect any HFO exceeding the noise levels. To investigate frequency spectra of the oscillations, the high-frequency residuals in the U and I bands were subjected to a power spectrum analysis with the Tukey spectral window (Jenkins & Watts, 1969). The power spectra of the residuals in the bottom row of Figure 8.2 show low-coherent oscillations in the U and I wavelengths during the outburst, with periods $P_U = 4.5 \pm 0.1 s$ and $P_I = 6.3 \pm 0.1 s$, respectively. It is likely that only one frequency is strongly excited at a time. It must also be noted that there is a clear difference in frequencies of the the oscillations registered in the U and I bands.

8.3.2 The flare on September 12, 2004

Figures 8.3 and 8.5 represent the light curves and color index tracks of the flare registered on September 12, 2004. The flare duration is 107s. All sites in Ukraine,

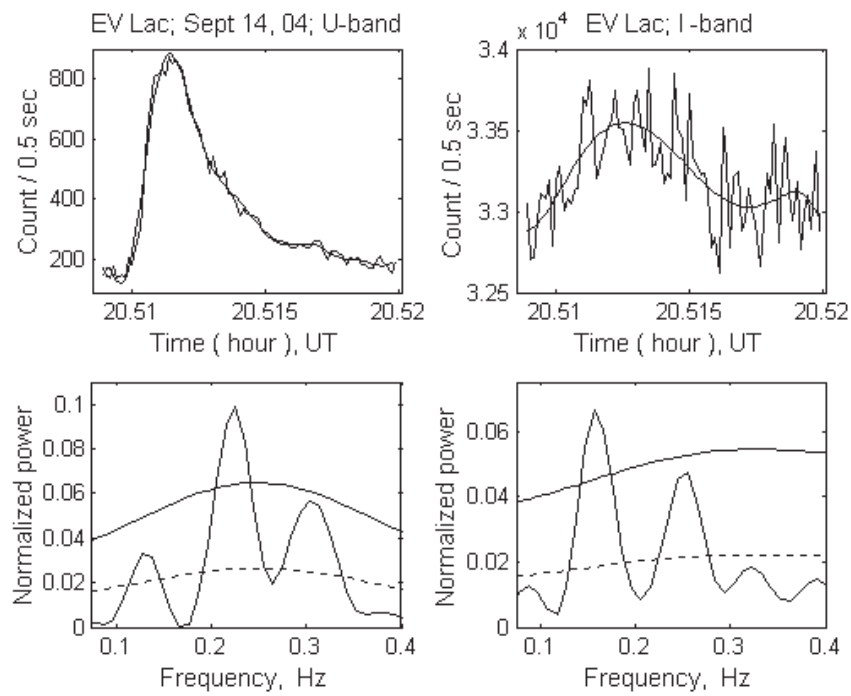


Figure 8.2. The light curves of the flare on September 14, 2004 in the U (top left) and I (top right) filters and their polynomial fits. Power spectra of the residuals (the bottom row) show low-coherent oscillations in the U and I wavelengths during the outburst, with periods of 4.5 and 6.3 sec, respectively. A 99% confidence level for data dominated by a Poisson noise is marked by solid lines.

Russia, Greece and Bulgaria have observed this flare event. Figure 8.3 shows the remarkable consistency of the U-band light curves simultaneously obtained by three instruments of the Crimean, Stephanion and Belogradchik observatories. The smoothed data show clear presence of HFO in the descending slope of the flare light curve.

The color index diagrams are based on the data obtained with the Crimean 1.25-m reflector AZT-11. Figure 8.5 shows both the filtered UBV light curves and the color index tracks, thus visualizing the long-term trends and the color index variation during the flare. The 95% confidence intervals for the color curves were determined under assumption of a Poisson noise. It can be seen that the U-B and B-V color indices are in opposite phases (Figure 8.5 lower panels).

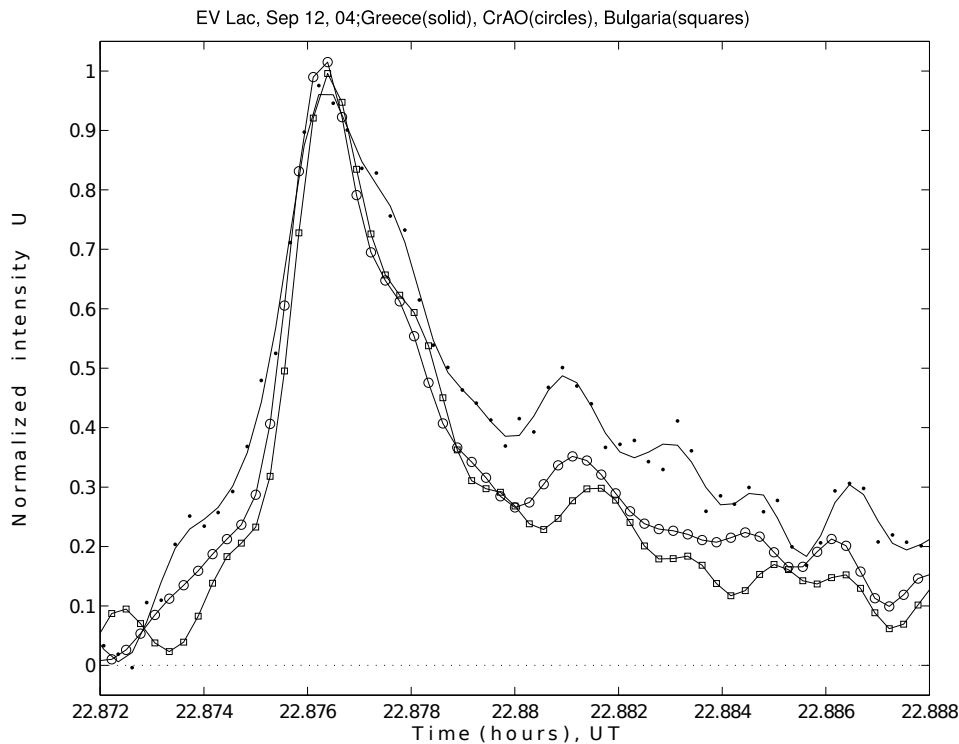


Figure 8.3. Multi-site photometry of the flare on September 12, 2004, 22.876 UT (max), as simultaneously seen by the three telescopes: AZT-11 CrAO, Ukraine (circles), 76cm Stephanion, Greece (solid) and 60cm Belogradchik, Bulgaria (squares).

Figure 8.4 shows the power spectra of high-frequency residuals calculated from the data simultaneously obtained by the three remote telescopes, AZT-11 (1.22-m) at CrAO, 76cm at Stephanion and 60cm at Belogradchik. All the three spectra show evidence of low-coherent oscillations with frequencies $F_0 = 0.06 \pm 0.01 Hz$, $F_1 = 0.12 \pm 0.01 Hz$ and $F_2 = 0.16 \pm 0.01 Hz$ and periods respectively $P_0 = 17 \pm 0.1 s$, $P_1 = 8 \pm 0.1 s$ and $P_2 = 6 \pm 0.1 s$, the most prominent of which being the lowest frequency

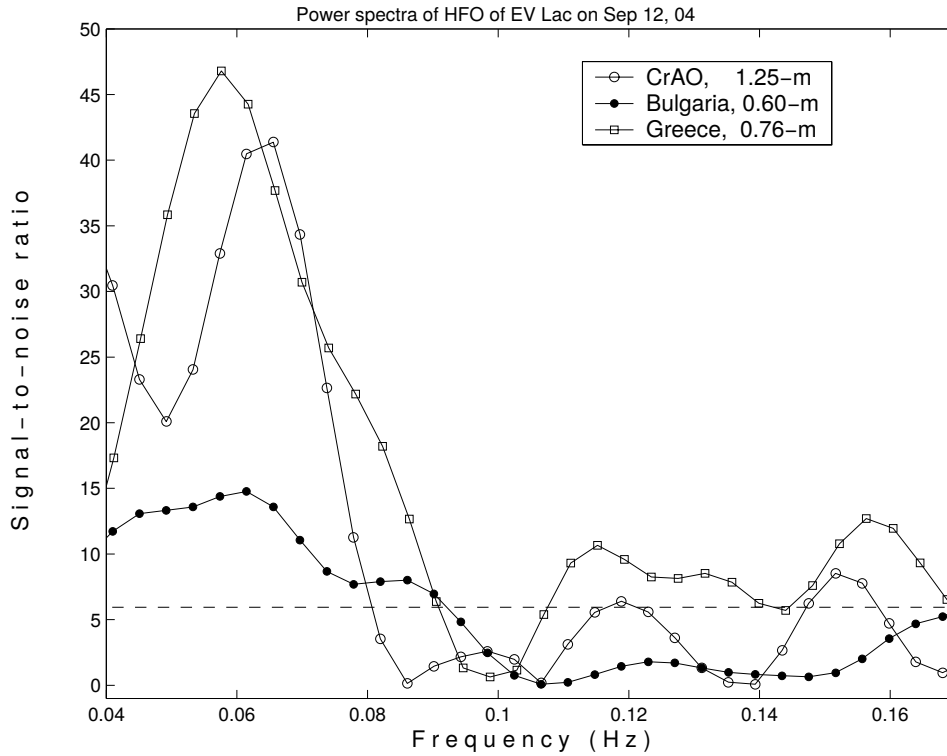


Figure 8.4. The power spectra of the flare on September 12, 2004 calculated on the data simultaneously obtained from three sites. The 99% confidence level for white noise data is shown as the dashed horizontal line according Zhilyaev et al. (2000).

one – F_0 . It has been detected in the data from all the three telescopes. However the higher frequency ones, F_1 and F_2 , are detected only by the bigger two telescopes. These frequencies are also visible in the Bulgarian data (the line with filled circles), though the peaks are less prominent and are below the credibility threshold, due to the smaller aperture of the telescope.

8.4 Some colorimetric results based on the data obtained during this campaign

Using the data obtained in this campaign Zhilyaev et al. (2007) executed an extensive colorimetric study of the observed events as described in Gershberg (2005). Two-colour diagrams were constructed for the flares. These diagrams show the colour changes of the radiation during the flare. By comparing the resulting colour tracks with the theoretical diagram the type of the radiation can be estimated at every point in time during the unfolding of the flare.

Based on the colorimetric results Zhilyaev et al. (2007) deduced that the radiation during the maximum of the flare has a black body spectrum. Thus using the black body model for the photosphere of EV Lac in a quiet state, and the colorimetric data for the flare Zhilyaev et al. (2007) estimated the temperature and the size of the flaring area. However, during the other phases of the event the radiation varies and is unique for each flare. For example after the maximum of the flare on September 14 the colours slowly drift from blackbody to radiation of hydrogen plasma optically thick in the Balmer continuum and then to optically thin hydrogen plasma radiation. On the other hand the flare on September 12 shows a different picture, after the maximum it shows complex oscillations between the radiation of optically thick and optically thin hydrogen plasma in the Balmer continuum while passing several times over the black body region. The moments of blackbody radiation are marked with stars on the bottom panel of Figure 8.5.

The U-band luminosities of the flare and photosphere are determined from a black body spectrum convoluted with the U filter response. The observed flare amplitudes in the U band were $\Delta U = 1.47^m$ on September 12 and $\Delta U = 2.10^m$ on September 14. Colours near the maxima of the flares were determined to be $U - B \approx -1.1^m$ and $B - V \approx -0.1^m$ and the temperature of the flaring layer reaches approximately 18500 K. The temperature of EV Lac in quiet state is assumed to be $T_{eff} = 3300$ K (Pettersen, 1980). Based on this, the sizes of the projected flare areas are estimated to be approximately 1.1% of the apparent stellar disk for the flare from September 12 and approximately 1.3% for the flare on September 14, 2004. These values are in agreement with the values reported by Alekseev & Gershberg (1997) for nine strong flares of EV Lacertae with $\Delta U > 1.8^m$.

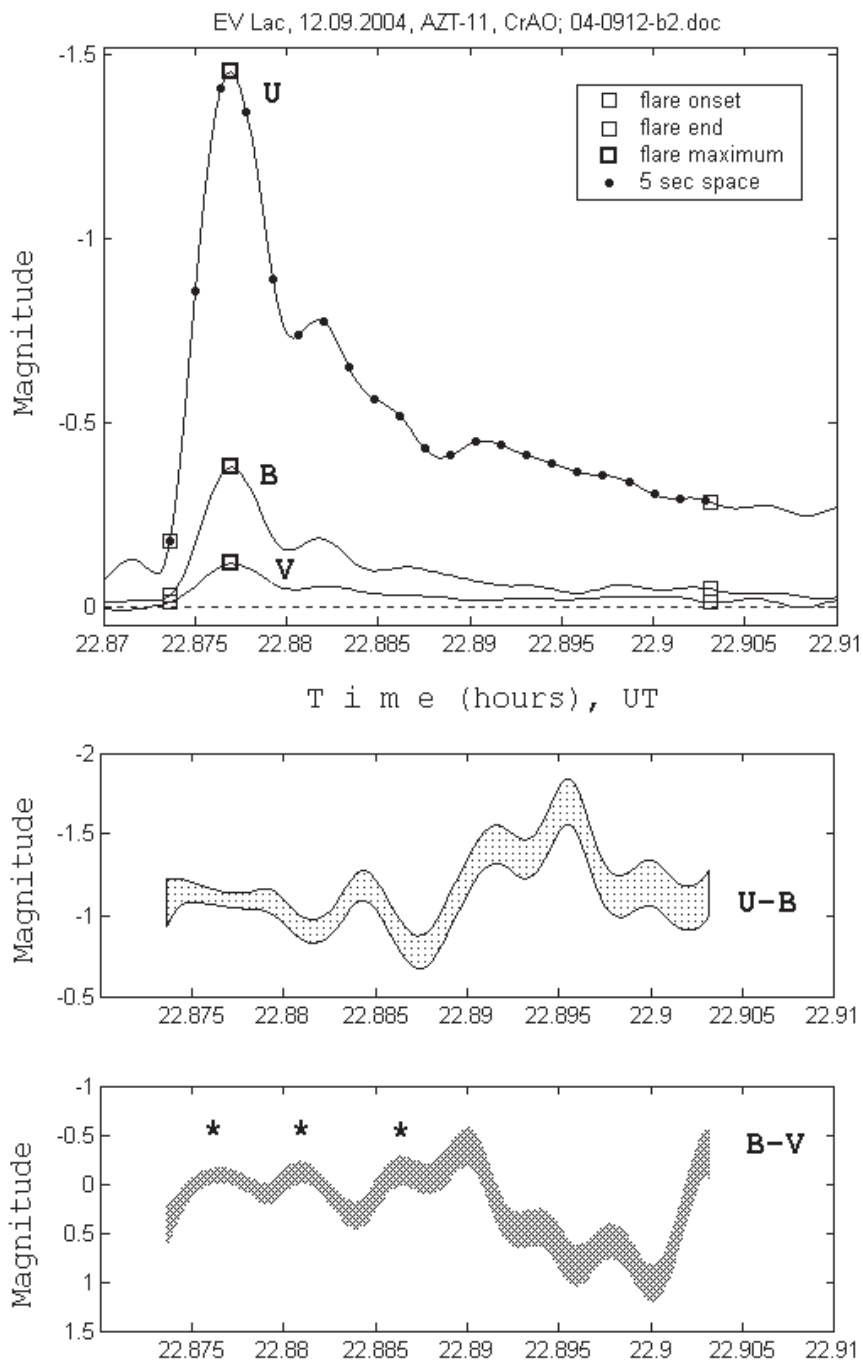


Figure 8.5. The filtered UB light curves (upper panel) and the corresponding colors (lower panel, with 95% confidence intervals) visualizing the long-term fluctuations with $P \sim 17$ s.

Photometric study of the flare activity of AD Leonis

AD Leo is a well-known main sequence active M-dwarf star with a spectral type M3.5eV (Shkolnik et al., 2009), residing in the solar vicinity. The distance to the star is 16 light years (van Altena et al., 1995). The surface temperature is $3,390K$ (Rojas-Ayala et al., 2012), the apparent magnitude $V = 9.4^m$ (Gliese & Jahreiss, 1991) and the absolute magnitude $M_v = 10.9^m$ (Gliese & Jahreiss, 1991). The radius of the star is determined to be $0.39R_{\odot}$ (Reiners et al., 2009), the mass is $0.42M_{\odot}$ (Reiners et al., 2009) and the luminosity $0.024L_{\odot}$ (Pettersen & Coleman, 1981). The mass and spectral type of AD Leo suggest that the star is very close to the threshold of being fully convective.

During a proper motion study held in 1943 AD Leonis was suspected of having a companion (Reuyl, 1943). However, Lippincott (1969) was unable to confirm this result. More recent search with a near-infrared speckle interferometer failed to detect a companion orbiting 1–10 AU from the star (Leinert, 1997). In 2001, an optical coronagraph was used, but no companion was found (Oppenheimer et al., 2001). Pettersen & Coleman (1981) detected no sign of variability in the radial velocity of the star, which also does not support the presence of the suspected by Reuyl (1943) companion.

Different aspects of its activity have been studied for more than six decades. Most of these studies concern the activity of the star. The variability of AD Leonis is first observed in 1949 at Lick Observatory by Gordon & Kron (1949) and today is one of the most active flare stars known. The net magnetic flux at the surface of the star is about 3kG (Reiners, 2007) and according to the study carried out by Crespo-Chacon et al. (2006) about 73% of its surface is covered by magnetically active regions. Another studies of the X-ray coronal emission of AD Leonis have found compact loop structures with sizes of about 30% of the star's radius (Favata et al., 1999; Sciortino et al., 1999). Pettersen et al. (1986) and Konstantinova–Antova & Antov (1995), suspected activity cycle, analogous to the solar activity cycle with a period of about 8 years.

Table 9.1. Data for the monitoring intervals and detected flares

Date	Time interval UT	Telescope*	No. of flares	Flares per hour
30/31.01.2006	00 ^h 02 ^m – 02 ^h 56 ^m	R2m	3	1.03
31.01/01.02.2006	23 ^h 14 ^m – 02 ^h 56 ^m	R2m, B60	4	1.08
01/02.02.2006	23 ^h 10 ^m – 03 ^h 01 ^m	R2m, B60	5	1.30
02/03.02.2006	22 ^h 05 ^m – 03 ^h 05 ^m	R2m, R60, B60	5	1.00
01/02.03.2006	21 ^h 30 ^m – 00 ^h 01 ^m	R2m	3	1.20
13/14.01.2007	00 ^h 17 ^m – 04 ^h 02 ^m	R60	2	0.53
15/16.01.2007	23 ^h 44 ^m – 03 ^h 59 ^m	R2m, R60	2	0.47
07/08.03.2007	20 ^h 00 ^m – 02 ^h 38 ^m	R60	1	0.15
08/09.03.2007	19 ^h 49 ^m – 02 ^h 25 ^m	R60	4	0.6
09/10.03.2007	21 ^h 08 ^m – 01 ^h 10 ^m	R2m, R60	2	0.5
11/12.03.2007	22 ^h 59 ^m – 00 ^h 39 ^m	R2m, R60	2	1.2
12/13.03.2007	20 ^h 48 ^m – 22 ^h 20 ^m	R2m, R60	0	0
13/14.02.2008	21 ^h 05 ^m – 01 ^h 30 ^m	R2m	2	0.45

* R2m - NAO-Rozhen 2m, R60 - NAO-Rozhen 60cm, B60 - AO-Belogradchik 60cm

9.1 Observations

The observations were carried out at BNAO–Rozhen and AO–Belogradchik in January–March 2006, January–March 2007 and February 2008. Zeiss 2m RCC telescope and Zeiss 60cm telescope at Rozhen and Zeiss 60cm telescope at Belogradchik were used. The observations were executed in the ultraviolet (U) band of the Johnson’s UBVR system with high-speed electrophotometers: Bulgarian–Ukrainian electrophotometer (BUF) (Antov et al., 2001) attached to the 2m telescope, the photon counting electrophotometer attached to the 60-cm telescope at Rozhen and photon counting electrophotometer attached to the 60cm telescope (Antov & Konstantinova–Antova, 1995) at Belogradchik. All the photometers were equipped with PCMs (see Chapter 5 and Appendix I). For accurate time synchronization a GPS was used. The monitoring intervals are presented in Table 9.1. The integration time for the 60cm telescopes was 1 s and 0.1 s for the 2m telescope.

9.2 Flare frequency and activity cycle

There were 20 flares detected during the 17.95 hours of effective observational time in 2006, 13 during the 28.45 hours in 2007 and 2 during the 4.42 hours in 2008 (Table 9.1). This data gives a flare frequency of 1.11 ± 0.25 flares/hour for 2006, 0.46 ± 0.12 flares/hour for 2007 and 0.45 ± 0.32 for 2008. The errors are cal-

Table 9.2. Flare frequency of AD Leonis from 1971 to 2008

Year	Flares/hour	Source [†]
1971.1	0.53±0.18	PET
1974.1	0.76±0.19	PET
1974.96	0.78±0.20	PET
1979.25	0.71±0.58	PET
1979.95	0.58±0.13	PET
1982.2	0.89±0.22	PET
1983.3	0.63±0.14	PET
1984.3	0.65±0.11	PET
1985.2	0.48±0.13	PET
1989.95	0.95±0.47	ANT*
1990.2	0.70±0.16	ANT*
1991.2	0.58±0.20	ANT*
1992.2	0.33±0.15	ANT*
1993.2	0.29±0.28	ANT*
1994.2	0.36±0.18	ANT*
2006.2	1.11±0.25	This work
2007.2	0.46±0.12	This work
2008.2	0.45±0.32	This work

[†] PET – Pettersen et al. (1986), ANT – Konstantinova–Antova & Antov (1995)

* Only the year of the observation was published in the paper, for better time resolution the month was determined in a personal discussion with the author.

culated as $F_{error} = \sqrt{n}/T$, where n is the number of flares observed during the monitoring time T . The significant change in the flare rate for 2006 and 2007 has to be mentioned also.

According to Pettersen et al. (1986) maxima in the flare activity are observed in 1974 (0.77 flares per hour) and in 1982 (0.89 flares per hour). They have calculated average flare activity for the years from 1971 to 1985 to be 0.66 flares per hour and suggested an activity cycle with period of about 8 years. More evidences for this period to be true are presented by Konstantinova–Antova & Antov (1995). They reported the somewhat unreliable, due to a short monitoring time, flare activity of 0.95 (± 0.47) flares per hour for 1989 and 0.70 flares per hour for 1990. A comparison with data published before suggests that AD Leo should be at the maximum of its activity cycle somewhere in 2005–2006. The observations presented here are in agreement with this assumption. Also the rapid decrease of the flare activity from 2006 to 2007 repeats the rapid decrease reported by Konstantinova–Antova & Antov (1995) from 1990 to 1992.

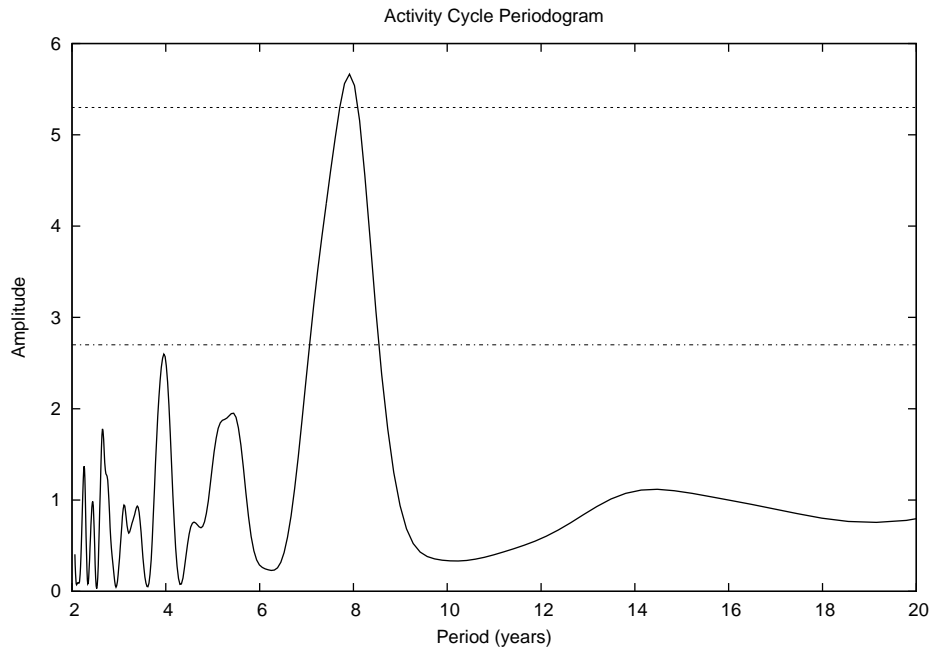


Figure 9.1. The Lomb-Scargle periodogram of the flare frequencies of AD Leonis from 1971 to 2008 shown in Table 9.2. The periodogram shows reliable activity cycle $P_{ac} = 7.91^{+0.11}_{-0.10}$ years. Below the dash-dot line the false alarm probability is $>99\%$ and above the dashed line it is $< 20\%$.

This motivated a period search for the activity cycle of the star. Lomb-Scargle period search is performed on the available flare frequency data: nine data points from Pettersen et al. (1986), six points from Konstantinova–Antova & Antov (1995) and three points determined above. Konstantinova–Antova & Antov (1995) published only the year of the observation, which is not enough for accurate period search, therefore more accurate timing data was requested from the authors. This data combined with the available data is shown in Table 9.2. The Lomb-Scargle method is described in details in Scargle (1982). The periodogram showed a definitive peak (see Figure 9.1) at $P_{ac} = 7.91^{+0.11}_{-0.10}$ years with $<20\%$ false alarm probability. This result is well in agreement with the suspected activity cycle $P_{ac} \approx 8$ years reported by Pettersen et al. (1986).

An analysis of the distribution of the flares in regard of the rotational period of the star was also performed. We tried the 2.7 days rotational period (Spiesman & Hawley, 1986) and the more recently determined value of 1.7 days (Gudel et al., 2001). However this two periods are discarded by Morin et al. (2008) and they determined a period of 2.24 days. Well in agreement with this period is the one of 2.23 days determined from the data obtained with Microvariability and Oscillations of Stars (MOST) Satellite (Hunt-Walker et al., 2012).

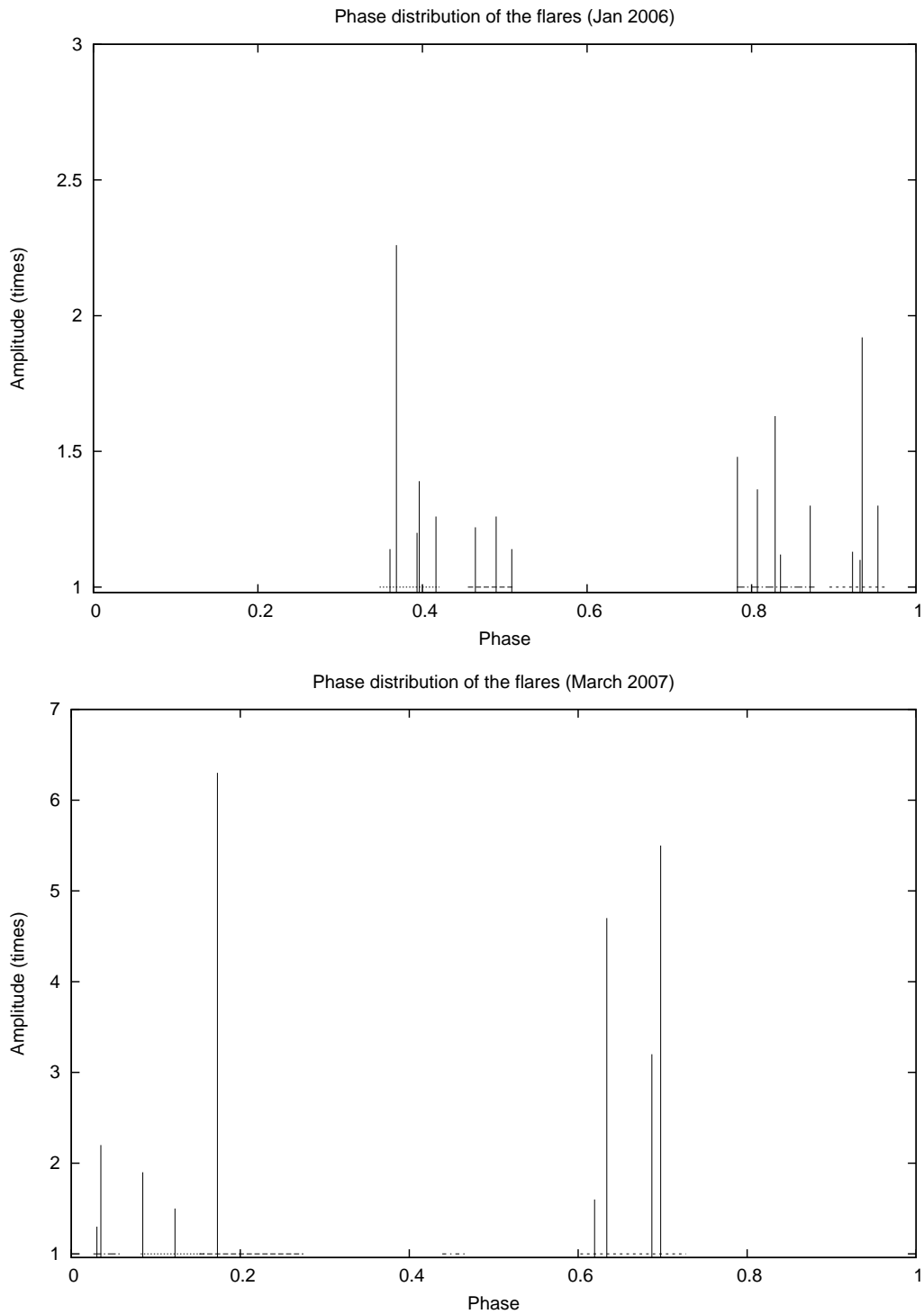


Figure 9.2. Phase distribution of the flares of AD Leo in January 2006 (upper panel) and March 2007 (lower panel) using a rotational period of 2.2d. (Dashed lines indicate the monitored intervals and the amplitudes are in times relative to the brightness in quiet state)

No distinct pattern in the flare distribution could be found for both 2006 and 2007 (Figure 9.2). This may be due to the almost pole on angle which should be about 20° (taking into account $V \sin i = 3.0 \text{ km/s}$ (Reiners, 2007), $R = 0.38 R_\odot$ and $P = 2.2d$).

9.3 Using wavelets to search for high–frequency optical oscillations

The wavelet transform can be a useful tool for analyzing time series with non-stationary power at many frequencies as shown in (Daubechies, 1990). This is why in this work wavelets are used to search for high–frequency transient optical oscillations in the AD Leonis observational data. A detailed practical guide of the wavelet technique is given in Torrence & Compo (1998). Here only a short overview of the used technique is given.

9.3.1 The Wavelet transform used for the performed analysis

A given function $\Psi(\eta)$, dependent on nondimensional time parameter η is admissible for a wavelet basis if it has zero mean and if it is localized in both time and frequency domains (Farge, 1992). In this work a Morlet wavelet (9.1) is used for several reasons. It is complex, because of that it has a single localized peak in frequency domain (Figure 9.3). The symmetry of the frequency domain representation, together with the definition of the continuous wavelet transform (9.2) makes it effective time localized band pass filter. This makes it a good choice for searching for transient oscillatory features in the stellar light curves, as long as the data points x_n are with equal time spacing δt .

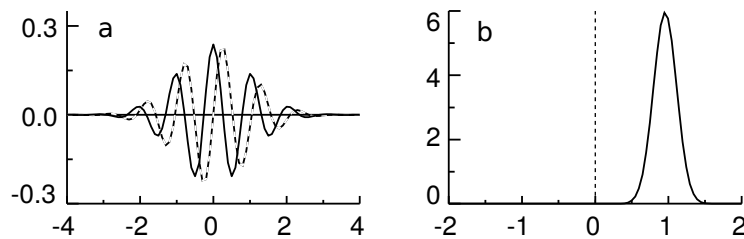


Figure 9.3. a. Morlet base in the time domain $\Psi(t/s)$ with $\omega_0 = 6$ (real part shown as solid line, imaginary as dashed).
b. The same wavelet base in the frequency domain $\widehat{\Psi}(s\omega)$.

The Morlet wavelet is essentially a wave modulated by a Gaussian and is defined as:

$$\Psi_0(\eta) = \pi^{-\frac{1}{4}} e^{i\omega_0\eta} e^{-\frac{\eta^2}{2}} \quad (9.1)$$

where ω_0 is the nondimensional frequency (here $\omega_0 = 6$ to satisfy the localization condition). This wavelet is non orthogonal which makes it possible to be used with continuous wavelet transform.

The continuous wavelet transform $W_n(s)$ of the discrete series x_n , $n = 0 \dots N-1$ is defined as the convolution of x_n with a scaled and translated function $\Psi_0(\eta)$:

$$W_n(s) = \sum_{n'=0}^{N-1} x_{n'} \Psi^* \left[\frac{(n' - n) \delta t}{s} \right] \quad (9.2)$$

where Ψ^* is the complex conjugate of Ψ and the subscript 0 is dropped to represent that Ψ has been normalized (9.6), n is localized time index and s is the wavelet scale. By varying n and s , a picture can be constructed to show the amplitude of the features versus the wavelet scale and how they change with time. However approximating the continuous wavelet transform using (9.2) is inefficient as the convolution has to be done N times for each scale (Kaiser, 1994). The convolution theorem allows all N convolutions to be done at the same time in the frequency domain. To do so one needs to use the Fourier transform $\hat{\Psi}(s\omega)$ of the $\Psi\left(\frac{t}{s}\right)$ and Discrete Fourier Transform (DFT) should be performed on the time series x_n :

$$\hat{X}_n = \frac{1}{N} \sum_{n=0}^{N-1} x_n e^{-\frac{2\pi i k n}{N}} \quad (9.3)$$

According to the convolution theorem $W_n(s)$ can be calculated by applying inverse Fourier transform to the product:

$$W_n(s) = \sum_{k=0}^{N-1} \hat{x}_k \hat{\Psi}^*(s\omega_k) e^{i\omega_k n \delta t} \quad (9.4)$$

here ω_k is the angular frequency given by:

$$\omega_k = \begin{cases} \frac{2\pi k}{N\delta t} & : k \leq \frac{N}{2} \\ \frac{-2\pi k}{N\delta t} & : k > \frac{N}{2} \end{cases} \quad (9.5)$$

In order to provide direct comparability between the wavelet transforms (9.4) of different scales s and the transforms of other time series, the wavelet function $\widehat{\Psi}_0(s\omega)$ has to be normalized to have unit energy at each scale:

$$\widehat{\Psi}(s\omega_k) = \left(\frac{2\pi s}{\delta t}\right)^{\frac{1}{2}} \widehat{\Psi}_0(s\omega_k) \quad (9.6)$$

For each scale s with this normalization one has $\sum_{k=0}^{N-1} |\widehat{\Psi}(s\omega_k)|^2 = N$, which means that the wavelet transform is not weighted by the wavelet function, but only by the amplitude of the \widehat{x}_k .

To calculate the wavelet power spectrum one has to bear in mind that the Morlet basis (used here) is a complex function therefore the transform is also complex. So $W_n(s)$ has real part $\Re\{W_n(s)\}$ and imaginary part $\Im\{W_n(s)\}$. Taking this into account the amplitude of $W_n(s)$ is $|W_n(s)|$, the phase is $\tan^{-1} [\Im\{W_n(s)\}/\Re\{W_n(s)\}]$, and the power spectrum can be defined as $|W_n(s)|^2$.

In order to perform the wavelet transform, an adequate set of scales should be chosen. For non-orthogonal wavelets like Morlet an arbitrary set of scales can be used. For convenience these scales are written as fractional powers of two:

$$s_j = s_0 2^{j\delta j}, j = 0, 1, \dots, J \quad (9.7)$$

$$J = \delta j^{-1} \log_2 (N\delta t/s_0) \quad (9.8)$$

where J is the largest scale and s_0 is the smallest resolvable scale. For the Morlet wavelet the largest reasonable value for δj that gives adequate sampling is 0.5 and s_0 should be chosen so that $s_0 \approx 2\delta t$, where δt is the equivalent Fourier period. For determining the relationship between the scale and the Fourier period the method of Meyers et al. (1993) can be used. The method is quite straightforward, a cosine wave with known period λ is fed to the wavelet transformation (9.4) and the scale s at which there is a maximum in the wavelet power spectrum corresponds to λ . For the Morlet wavelet $\lambda = 1.03s$ if $\omega_0 = 6$.

9.3.2 Reconstruction of the original time series

Wavelet transform, being a strictly defined and known band-pass filter, permits reconstruction of the original time series. This can be achieved by using the inverse filter or deconvolution. For orthogonal basis wavelets it is easy achievable by us-

ing the orthogonal basis function. However for the continuous wavelets with non orthogonal basis, as in the case described here it is not as easy, but still possible by using a different wavelet function. Farge (1992) gives a solution by using a δ function:

$$x_n = \frac{\delta_j \delta t^{1/2}}{C_\delta \Psi_0(0)} \sum_{j=0}^J \frac{\Re\{W_n(s_j)\}}{s_j^{1/2}} \quad (9.9)$$

To convert the wavelet to energy density $s_j^{1/2}$ is used and $\Psi_0(0)$ removes the energy scaling. C_δ is a constant for the used wavelet basis. C_δ can be calculated by reconstructing the δ function from its transform using the same basis. For Morlet with $\omega_0 = 6$, $C_\delta = 0.60$.

9.3.3 Significance levels

It is assumed that the power spectrum of the given time series can be modelled with red or white noise, therefore a null hypothesis is defined by assuming that the time series has a mean power spectrum given by:

$$x_n = \alpha x_{n-1} + z_n \quad (9.10)$$

where α is assumed to be lag-1 autocorrelation, $x_0 = 0$ and z_n is Gaussian white noise, so if $\alpha = 0$ it is pure white noise.

Thus if a given peak in the power spectrum is significantly above the average background spectrum it can represent a real feature with a certain degree of confidence. If one defines 99% confidence level (as used in this research) this means that if the value of the peak in the spectrum is above the 99th percentile of the simulated values for this frequency using the model, it is assumed to be real as it is significant at the 1% level.

A formal definition and how to compute the significance level can be found in Torrence & Compo (1998).

9.4 Search for High-frequency optical oscillations during flares

No optical oscillations have been detected on AD Leo before. There are evidences for such in the radio wavelengths only (Stepanov et al., 2001; Zaitsev et al., 2004). The wavelet technique described in section 9.3 is applied to the data set obtained

in Johnson ultraviolet (U) band in the years from 2006 to 2008 during the observations carried out on the 2m Ritchey-Cretien and 60cm Cassegrain telescope at Bulgarian National Observatory Rozhen, and the 60cm telescope at Belogradchik observatory. Morlet basis function with $\omega_0 = 6$ is used for the wavelet transform.

The wavelet transformations are depicted as time versus period plots and colour represents amplitude. In this representation the constant frequency oscillations should usually (but not necessarily) look like isolated "islands" elongated in time direction (parallel to X-axis). To consider a given wave a real oscillation it should repeat at least three times. So only the "islands" on the plot with length in time greater than three times the period at which they are located (Y-axis) and with maximum amplitude above certain confidence level (see Section 9.3.3) are considered to represent real oscillations.

For the flares observed on one telescope, a confidence level of 99% is used. This is rather conservative confidence level, but the lack of possibility to cross check the results with data from another telescope motivated the choice of this confidence level. Another reason to try to avoid false detection as much as possible, is the fact that no optical oscillations on AD Leo have been reported before. For the flares observed on more than one telescope there was no detection even with confidence level of 95%.

The stroked areas around the top edges on the wavelet diagrams represent the cone of influence. Within this region the edge effect is very strong and the features that present there should not be taken in consideration while analyzing the results.

The light curve of the flare is depicted on top of the wavelet diagram with the same timescale to make it easy to determine on what phase of the unfolding of the flare the oscillations start and seize. The light curve shows the relative flux in times the flux in quiet state (when the star is not flaring).

The wavelet plots of seven more unusually shaped flares are presented here (Table 9.3). All of them show complex structure except flare №6 (Figure 9.11), which displays rather "classical" shape for a flare with fast ascending and slowly descending slope. The dip in the descending slope is not confirmed by the second telescope (Figure 9.10) and can be attributed to a temporary atmospheric transparency deterioration. Taking this in to consideration the data from the 2m telescope is shown, because of the better signal to noise ratio. The data from the 60cm telescope is used only to confirm any suspected oscillations. However no oscillations are de-

Table 9.3. Details of the discussed flares

№	Date	UT start	UT Max	Duration	ΔU	Figure
1	14.01.2007	02:07:25	02:08:14	10 min	$1.54^m \pm 0.07$	9.4
2	15.01.2007	02:40:40	02:43:42	36 min	$0.24^m \pm 0.05$	9.6
			02:46:57	43 sec	$0.62^m \pm 0.05$	
3	08.03.2007	21:25:58	21:33:34	48 min	$1.42^m \pm 0.06$	9.7
4	09.03.2007	00:17:33	00:17:56	8 min	$1.24^m \pm 0.07$	9.8
5	09.03.2007	00:49:35	00:58:59	43 min	$1.86^m \pm 0.07$	9.9
6	11.03.2007	23:26:45	23:27:22	4 min	$0.85^m \pm 0.07$	9.11
			22:55:23	5 min	$1.26^m \pm 0.08$	
			22:56:32			$2.38^m \pm 0.08$

tected on both data sets for this flare. Very few of the detected flares of AD Leo exhibited this "classical" shape.

Flare №1 (Figure 9.4) and flare №3 (Figure 9.7) show multiple maxima and a gradual release of energy, which is an evidence for multiple magnetic reconnections in a very complex structure of one or more active regions producing the flares. The light curves of these flares show very similar morphology to the light curves of some homologous solar flares like the ones published by Zhang & Wang (2002), Liu et al. (2014) and Guo et al. (2012). Homologous flares are series of flares originating in the same active area usually showing gradual release of energy. Woodgate et al. (1984) were the first to use this term for solar flares.

On the other hand each of the flares: №2 (Figure 9.6) and №4 (Figure 9.8) show two separate "classical" flares superimposed on each other. Flare №2 consists of a slowly unfolding low amplitude flare which lasts for 36 minutes and a fast higher amplitude one, shown in details on Figure 9.5, that lasts for only 42 seconds. Flare №4 shows two almost identical sub-flares. It is possible that the two pairs of flares are sympathetic – flares that do not coincide by chance, but are a result of a physical connection between the erupting regions. Some flares initiate various kinds of disturbances in distant regions on the stellar surface after a time proportional to the propagation speed of the disturbing agents, which in turn may result in a sympathetic flare (Svestka, 1976). An example of such disturbances are the flare waves proven by direct optical observations of the Sun by Moreton & Ramsey (1960) and Athay & Moreton (1961).

The double flare №7 (Figure 9.12) has two equally probable explanations. The first one is that the two flares are homologous, as they have similar morphology and the stronger one happens immediately after the first less energetic one, so they may be a result of two consecutive magnetic reconnections happening in the same active region. The other plausible scenario is a sympathetic flare. In this scenario the smaller flare provokes another active region to produce the bigger one. It is somehow unusual that the two sub-flares exhibit almost symmetrical ascending and descending slopes and the event is quite short lived for the achieved amplitude. From the onset of the first flare to the end of the second flare it took only 5 minutes and the first one achieved amplitude of 1.26^m while the second achieved maximum of 2.38^m . This is by far the strongest flare in the observed set of 35 flares and at the same time one of the most short lived. However, the most interesting flare is the second largest of the observed flares (flare №5) with amplitude of 1.86^m and duration of 43 minutes. This event is shown on Figure 9.9 and is discussed in detail in Section 9.5.

The presence of overlapping flares, probably sympathetic, and to some extent the complex morphology of many of the flares are indication of a complex magnetic structure which does not support the suggested by Morin et al. (2008) simple magnetic structure (dipole). A probable explanation is that AD Leonis has a relatively low $V_{\text{sin}i}$ of 3.0 km/s which leads to the reduced resolution of the Zeeman-Doppler Imaging (ZDI) map. Therefore ZDI can not resolve the fine features of the magnetic structure at the surface of AD Leonis.

9.5 Optical oscillations during flares

All the observed flares have been examined and only several of them showed indications of oscillations. The flare with the most definitive oscillation detection is given on Figure 9.9. This is a big flare with amplitude of 1.86^m observed on March 09, 2007 on the 60cm telescope at NAO Rozhen. The event starts at 0:49:35 UT, the maximum is reached at 0:58:59 UT and the duration is 43 minutes. This is the only flare with reliable detection of oscillations. The longest period damped oscillation starts with the flare and has a period of about $80 \pm 4_s$ (12.5mHz). Soon after this oscillation reaches its first maximum, about 25 seconds after it starts, the fastest oscillation starts, amplifying over the time, with a period of $45 \pm 2_s$ (22.2mHz). It can be assumed that the second oscillation is a result of an excitation provoked by the 80s oscillation. Around the maximum of the flare these two oscillations cease and another damped oscillation with a period of $60 \pm 2_s$ (16.7mHz) begins. The peak to peak amplitudes of the oscillations measured from the reconstructed series are

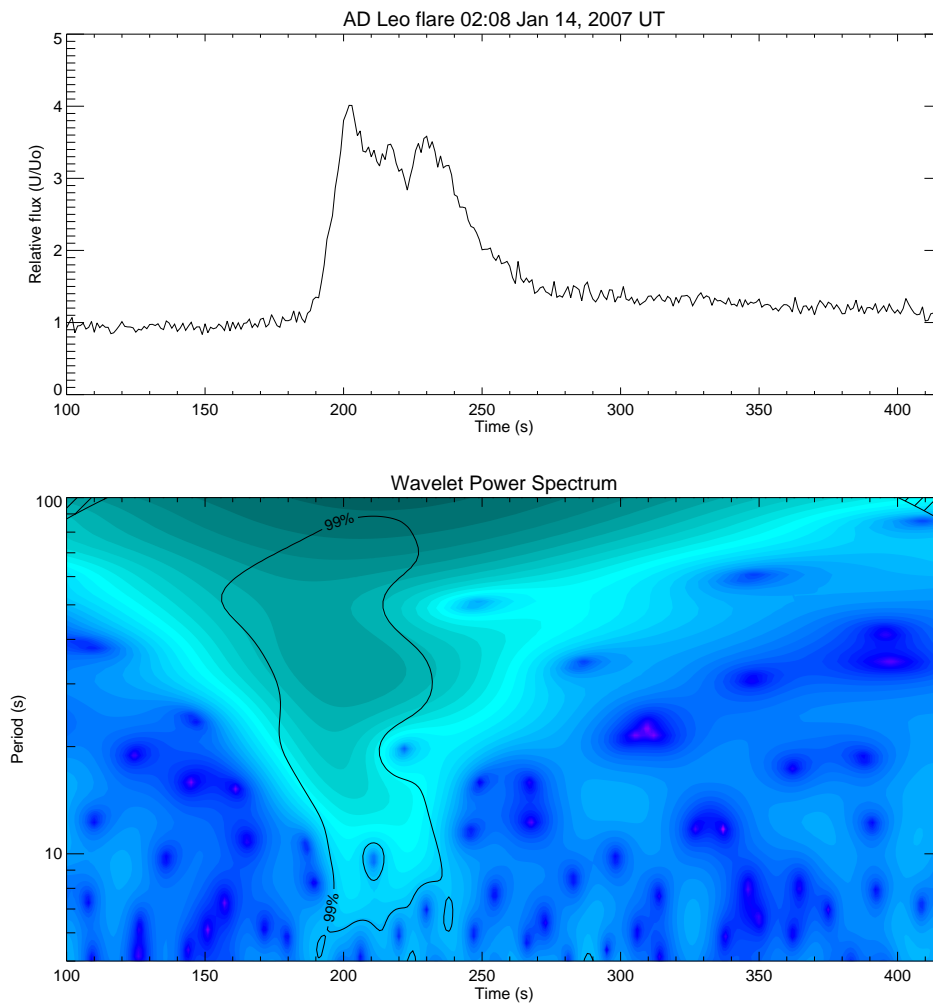


Figure 9.4. The light curve and the wavelet analysis of the flare of AD Leonis observed on the 60cm telescope at NAO Rozhen on 14.01.2007 starting at 02:07:25 UT with duration of 10 minutes. The maximum is at 02:08:14 UT with amplitude of 1.54^m .

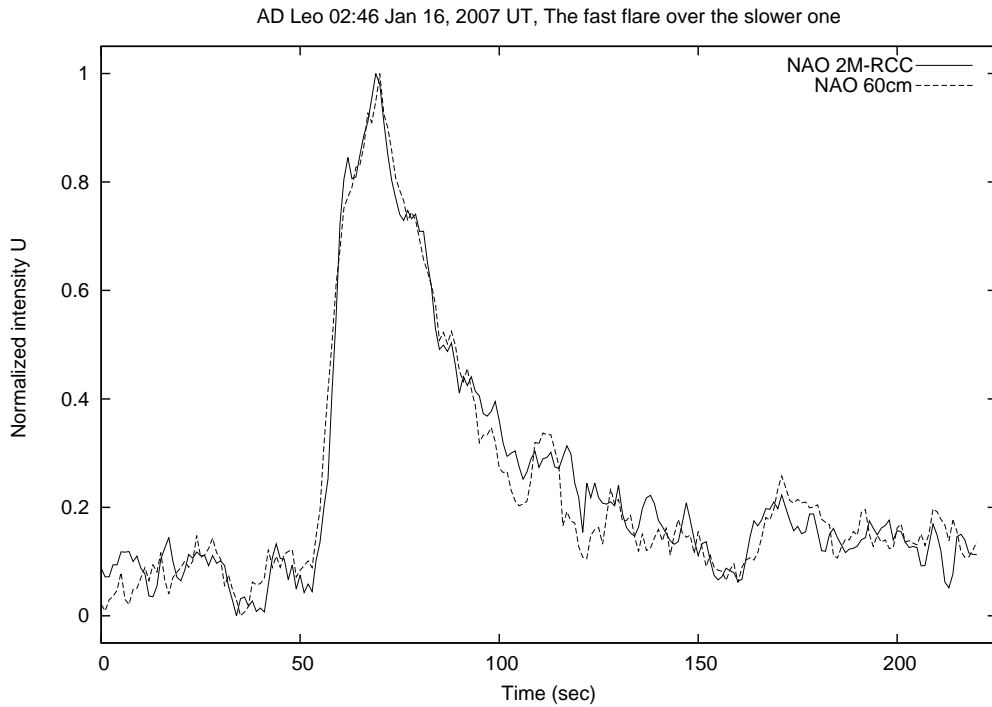


Figure 9.5. The flare of AD Leonis observed on 16.01.2007 on the 2m and the 60cm telescope at NAO Rozhen. The light curve shows a good correlation of the fine structure observed on the two telescopes. This is the faster of the two overlapping flares shown on Figure.9.6

approximately $\Delta U_{pp} \approx 0.12^m$ for the one with period of 80s, $\Delta U_{pp} \approx 0.10^m$ for the 45s one and $\Delta U_{pp} \approx 0.09^m$ for the 60s one.

The unusual shape of the light curve (slow ascending slope and fast descending slope with a bump at maximum) and the presence of multiple oscillations during this flare, is an indication of interaction of magnetic loops in an active area with a complex structure. Another possibility is that there are several separate active areas interacting. However the short time between the first and the second oscillation and the fact that the 60s oscillation starts around the maximum of the flare, suggest small distances between the oscillating loops. Also the damped 80s oscillation looks like transferring energy to the amplifying 45s oscillation somewhat resembling, as the frequencies are not the same, coupled oscillators. All this supports the assumption that only one active area is involved. A possible explanation of the phenomenon is the presence of arcade – a series of close by magnetic loops. Assuming that all other conditions are equal, the loops with different diameters will oscillate at different frequencies, the smaller the diameter of the magnetic loop, the higher the frequency of the oscillation. Therefore it can be assumed that magnetic loops with at least three different diameters are involved in this flare event.

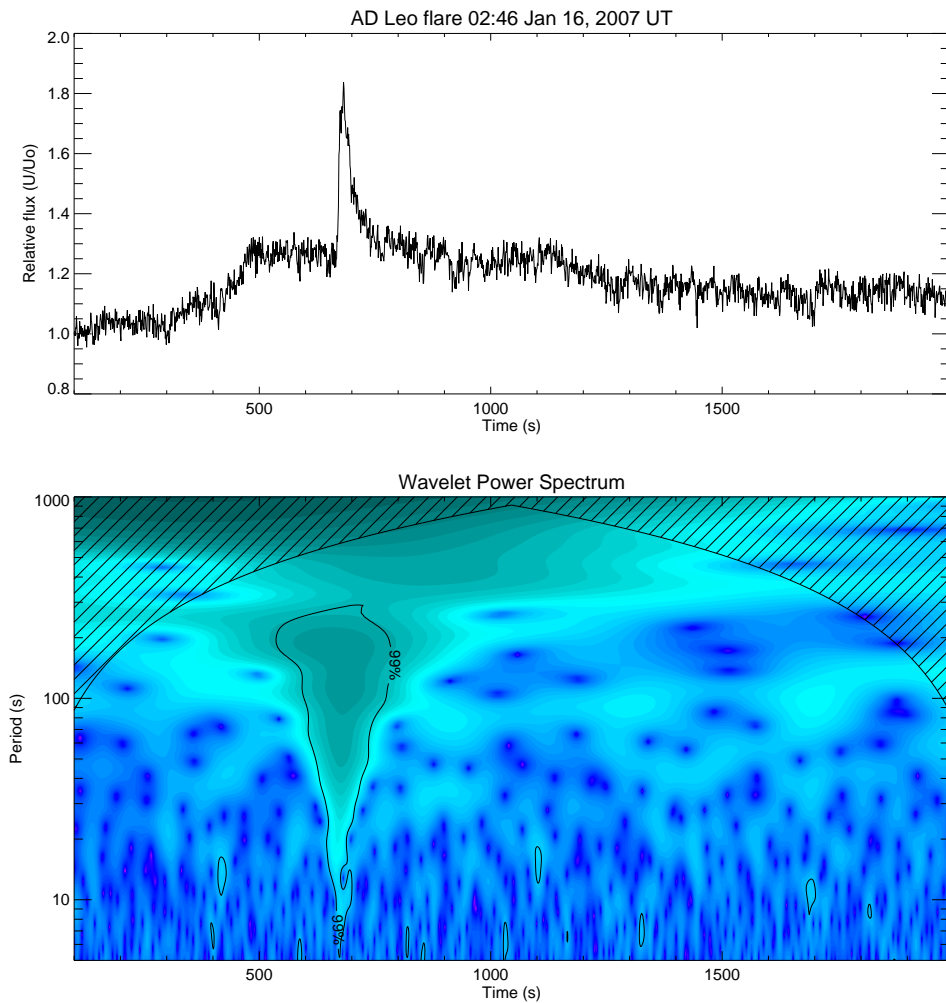


Figure 9.6. The light curve and the wavelet analysis of the flare of AD Leonis observed on 16.01.2007 on the 2M telescope at NAO Rozhen starting at 02:40:40 UT. This flare consists of two separate flares. One is slower with amplitude of 0.24^m with maximum at 02:43:42 UT and duration of 36min. While this event is unfolding, a second faster flare was observed with amplitude of 0.62^m shown on Figure 9.5. The maximum is at 02:46:57 UT and the duration is 43 seconds. The whole event has also been observed on the 60cm telescope at NAO.

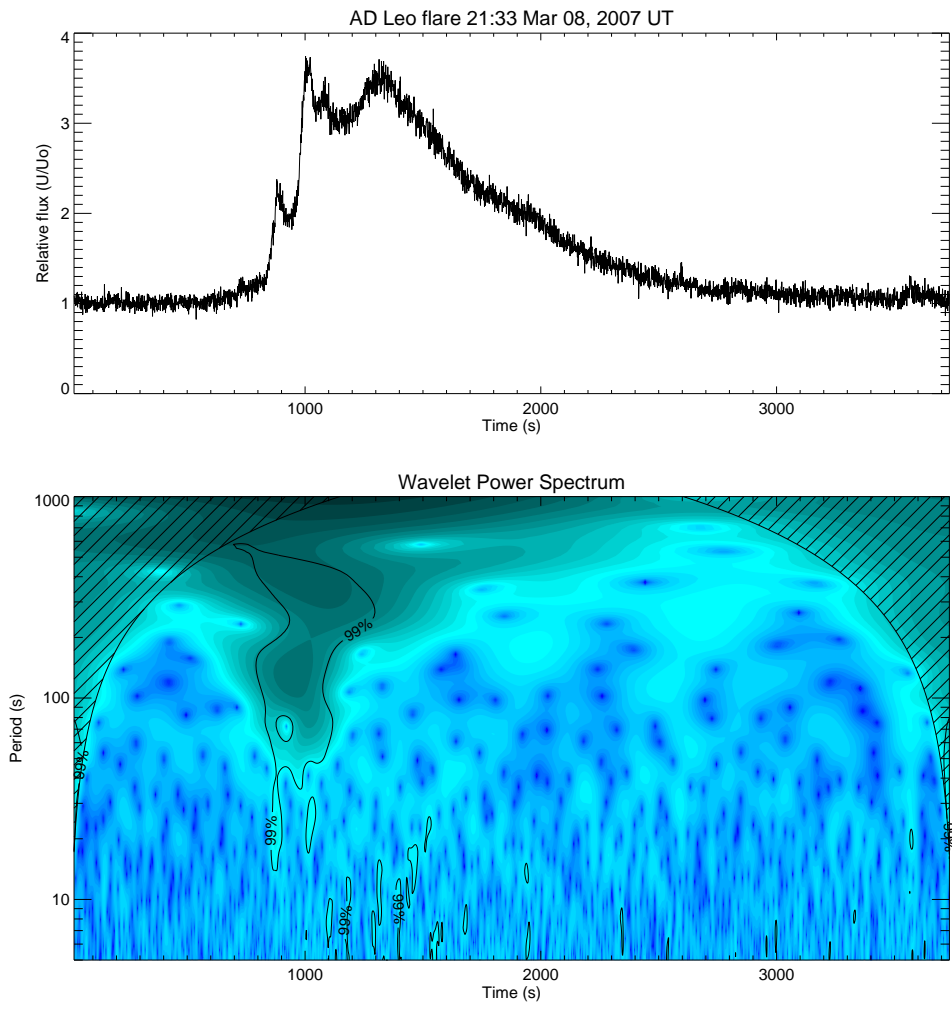


Figure 9.7. The light curve and the wavelet analysis of the flare of AD Leonis observed on the 60cm telescope at NAO Rozhen on 08.03.2007. The event starts at 21:25:58 UT, It shows a complex structure suggesting a chain of flares with maxima at 21:31:32 UT, 21:33:34 UT, 21:34:54 UT and 21:38:46 UT. The highest peak is 1.42^m and the whole event lasted for 48 minutes.

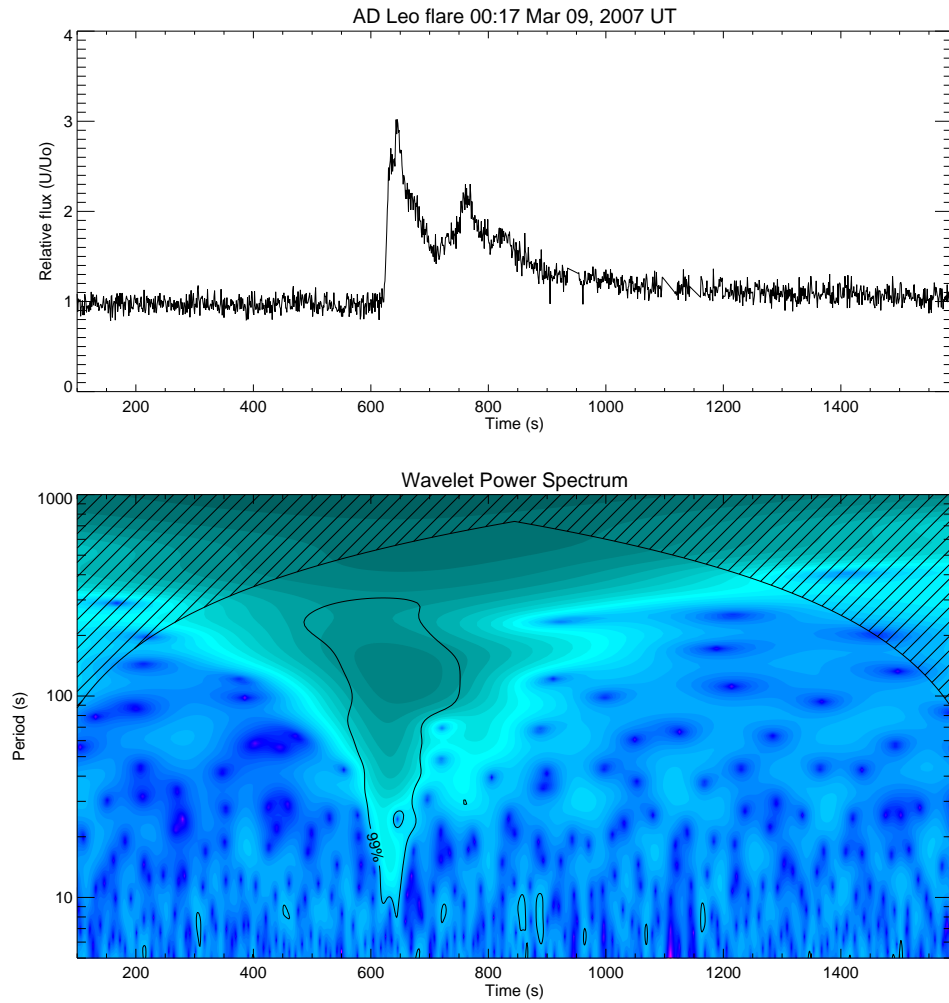


Figure 9.8. The light curve and the wavelet analysis of the flare detected on 09.03.2007 on the 60cm telescope at NAO Rozhen. The event starts at 0:17:33 UT. It shows two possibly sympathetic flares the first one with maximum at 0:17:56 UT triggered the second one with maximum at 0:19:53 UT. The maximum amplitude is 1.24^m and the duration is 8 minutes.

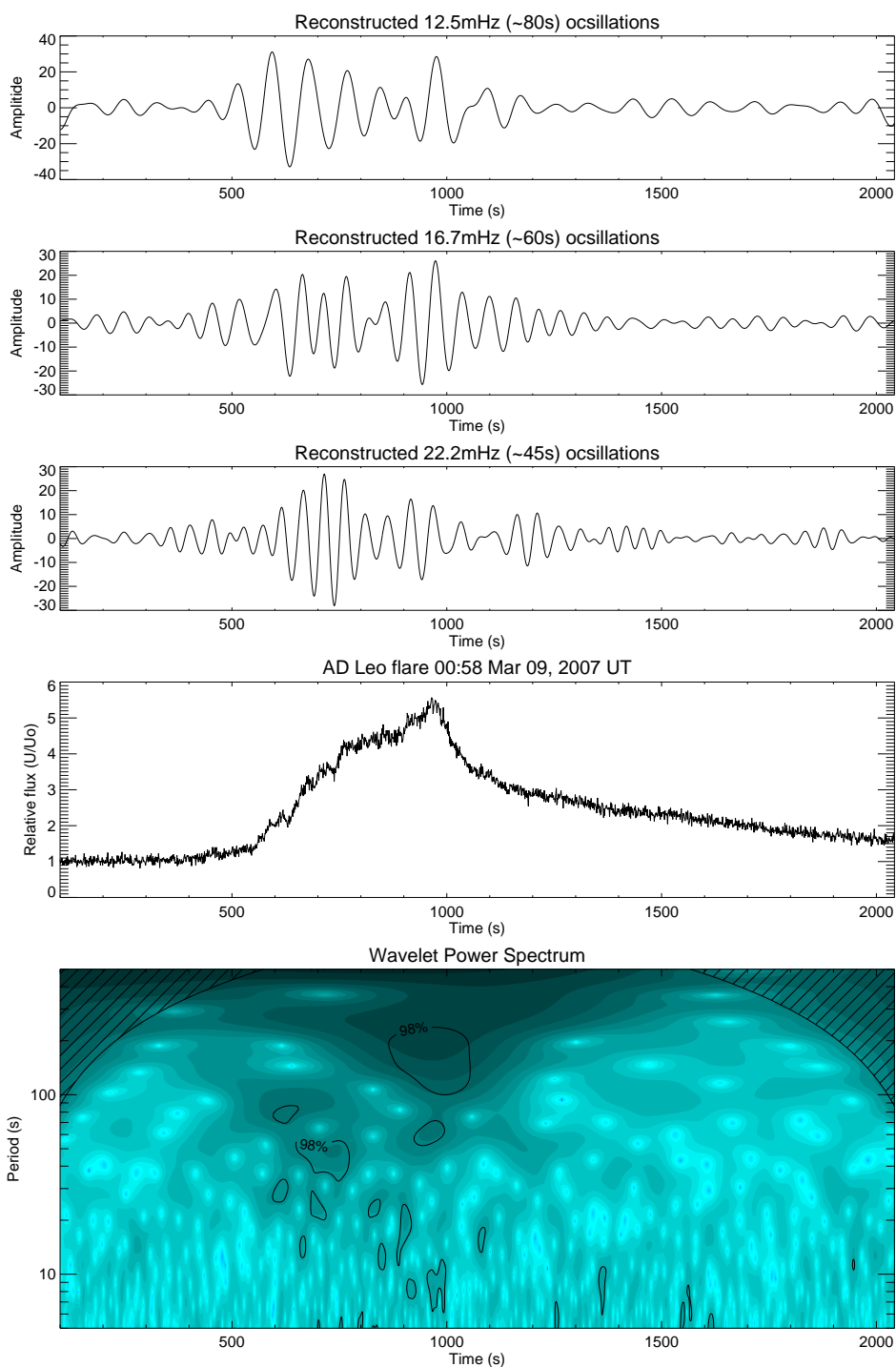


Figure 9.9. The light curve and the wavelet analysis of the flare detected on 09.03.2007 on the 60cm telescope at NAO Rozhen. The event starts at 0:49:35 UT, the maximum is at 0:58:59 UT, the amplitude is 1.86^m and the duration is 43 minutes. This is the only flare with reliable detection of oscillations. The longest period oscillation starts with the flare and has a period of about 80s. About 25 seconds later the shortest period (45s) oscillation starts. And at maximum the these oscillations end and another oscillation with a period of 60s is detected. The reconstructed oscillations are shown on the top panels.

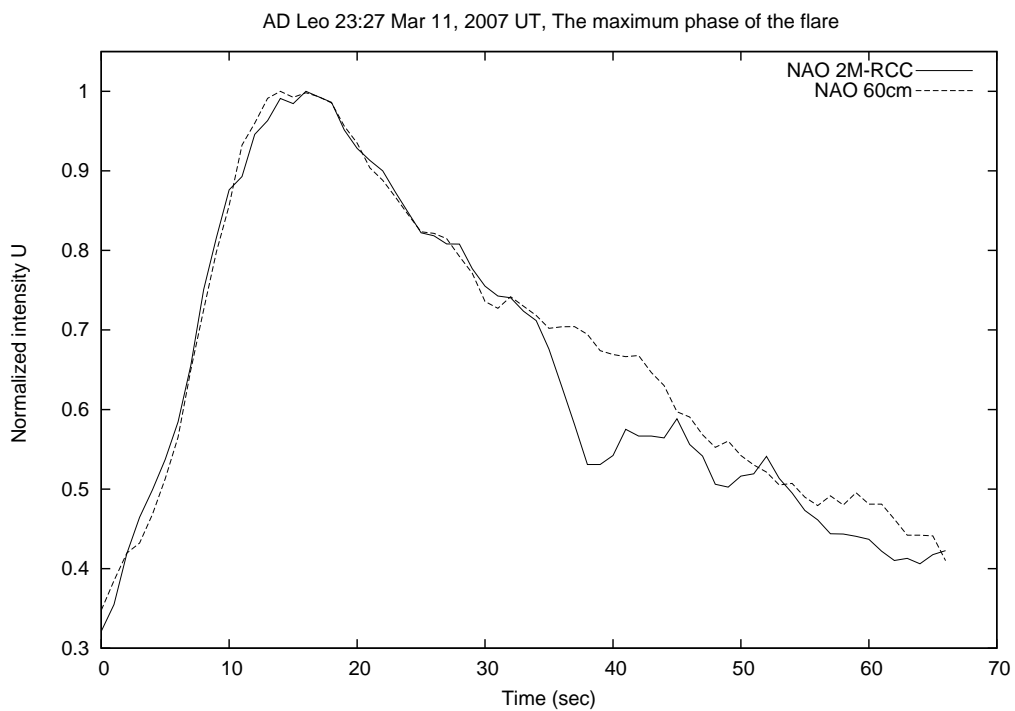


Figure 9.10. The maximum phase of the flare of AD Leonis observed on 11.03.2007 on the 2m and the 60cm telescope at NAO Rozhen. The light curve from the two telescopes shows a good correlation of the fine structure around the maximum. However 18 seconds after the maximum the transparency of the atmosphere for the 2m telescope is deteriorated, which is clearly seen.

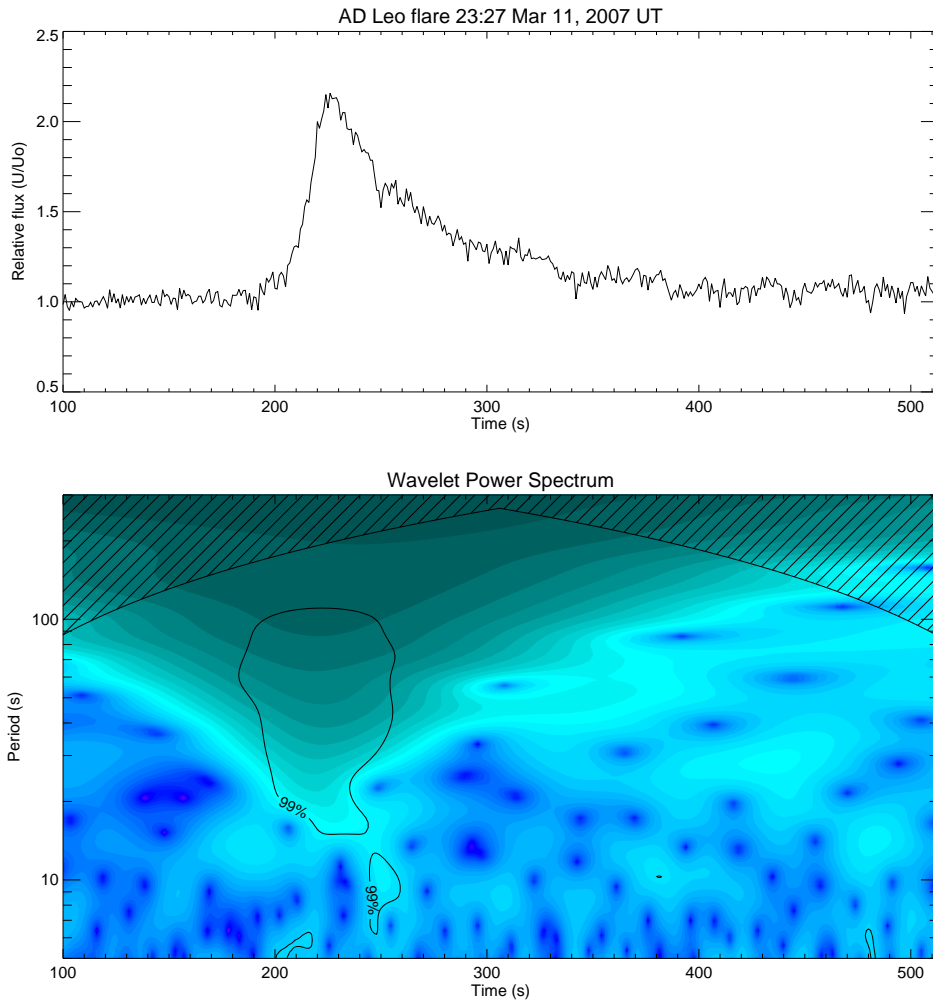


Figure 9.11. The light curve and the wavelet analysis of the flare detected on 11.03.2007 observed on the 2m telescope at NAO Rozhen. The event starts at 23:26:45 UT, the maximum is at 23:27:22 UT, the amplitude is 0.85^m and the duration is 4 minutes. The dip on the descending slope is not real as shown on Figure 9.10, but because of the bigger aperture and higher signal to noise ration the data from the 2 meter telescope is shown.

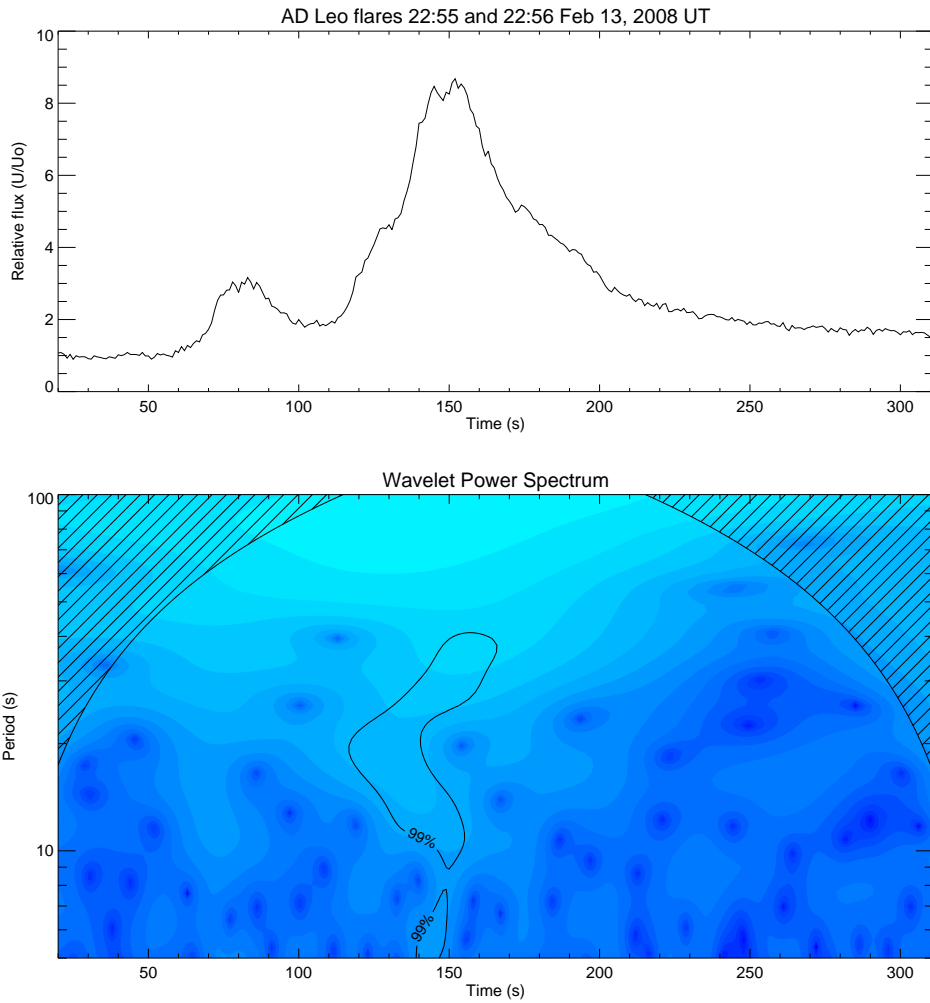


Figure 9.12. The light curve and the wavelet analysis of the big double flare detected on 13.02.2008 observed on the 2m telescope at NAO Rozhen. The event starts at 22:54:56 UT. The first maximum is at 22:55:23 UT and the amplitude is 1.26^m . The second maximum is at 22:56:32 UT and the amplitude is 2.38^m . The duration of the whole event is 5 minutes.

Conclusion

Although electro-photometry is available for more than fifty years, it still has advantages over the other photometric methods for some applications. It has high sensitivity, especially in the near ultraviolet, which allows, shorter integration times with relatively small telescopes. Another advantage is the nonexistence of dead time between the measurements. This gives a higher temporal resolution which is very useful for studying the high frequency structure of the light curves of various astronomical objects with small or relatively small telescopes. In particular, its high sensitivity in the ultraviolet part of the spectrum makes it very effective in studying the flares of chromospherically active stars, as the flares are more prominent in this part of the spectrum. The time synchronized simultaneous observations bring the electrophotometric data to a new level making it more accurate and reliable. The photometric system described here is already installed at the most of the sites that took part in the observational campaign in September 2004: three telescopes in Bulgaria – one at Belogradchik Observatory on the 60cm telescope equipped with a single-channel photometer and two at NAO Rozhen on the 2 meter and 60cm telescopes both equipped with a single-channel photometer, one at the Crimean Astrophysical Observatory on the 1.25 meter telescope (AZT-11) with a five-channel UBVRI photo-polarimeter and one at Terskol Observatory on the 2 meter telescope with a two-channel photometer.

The application of the new observational technique, high-speed, multi-site time synchronous monitoring and advanced data processing like wavelet analysis, proved to be fruitful. The existence of high frequency oscillations during the stellar flares are confirmed and fast colour variations of the radiation during the flare is discovered and it is shown that this is a typical feature of the flare. It is confirmed that the general tendency of a flare emission is to shift from a blackbody emission in maximum to a hydrogen plasma emission during the decay.

The existence of high frequency oscillations proves that flares are not always monotonous relaxation processes, but they have internal structure and nontrivial devel-

opment. As mentioned before the first description of the optical oscillations during a flare of EV Lacertae by Zhilyaev et al. (2000) was interpreted by Kouprianova et al. (2004) and they have estimated the loop height, the plasma density, the plasma temperature, the magnetic field strength and the cause of the oscillations. So, the next necessary step to understand the nature of the high frequency oscillations is to unite the magnetohydrodynamics (Kouprianova et al., 2004) and the radiative hydrodynamical approaches (Katsova et al., 1997; Allred et al., 2006).

The sheer number of hours spent monitoring AD Leonis from 2006 to 2008 and the number of the registered flares allowed the estimation of the flare frequencies of the star for these years. The highest frequency of 1.11 flares per hour for 2006.2 is the highest ever published flare frequency for this star. Using this data combined with the data for previous years, published in the literature, confirmed the suspected by Pettersen et al. (1986) activity cycle of AD Leonis and is estimated to be 7.91 years long.

Main Contributions

1. High frequency optical oscillations, with periods from 4.5 sec to 17 sec, during flares were detected on three telescopes during the synchronous observations of EV Lacertae.
2. The suspected activity cycle of ≈ 8 years (Pettersen et al., 1986) of AD Leonis was confirmed and measured to be 7.91 years.
3. For the first time wavelet analysis was used to search for transient high frequency optical oscillations during the flares of the chromospherically active dwarf stars. This method has several helpful features such as: good sensitivity to short transient events, as their power in the frequency domain is not washed out and remains significant even if they are very short; it is easy to estimate the start and the end moments of a particular short time event, as it has convenient time versus frequency representation etc.
4. For the first time optical oscillations (periods: 45 sec, 60 sec and 80 sec) were detected during a flare of AD Leonis.
5. A new photometric system for synchronous observations of the single object with distant telescopes was developed. It allows the study of the low-amplitude high-frequency transient events in the stellar variability. This system currently works on the 60cm telescope and 2m telescope at Bulgarian National Observatory Rozhen, on the 60cm telescope at AO Belogradchik, on the AZT-11 telescope at Crimean Astrophysical Observatory with the five channel photopolarimeter and on the 2m telescope at Terskol Observatory with the two channel electrophotometer.

List of publications on the topic, talks and posters

This work is based on the following publications:

“Network–based synchronous system for high-speed stellar photometry with distant telescopes”

Bogdanovski, R.

2006, Bulgarian Astronomical Journal, Vol. 8, p. 117

“Fast colorimetry of the flare star EV Lacertae from UBVRI observations in 2004”

Zhilyaev, B. E.; Romanyuk, Ya. O.; Svyatogorov, O. A.; Verlyuk, I. A.; Kaminsky, B.; Andreev, M.; Sergeev, A. V.; Gershberg, R. E.; Lovkaya, M. N.; Avgoloupis, S. J.; Seiradakis, J. H.; Contadakis, M. E.; Antov, A. P.; Konstantinova-Antova, R. K.; *Bogdanovski, R.*

2007, Astronomy and Astrophysics, Volume 465, 1, P.235-240

“Flare Activity of AD Leo in the Period 2006 - 2007”

Konstantinova-Antova, R.; *Bogdanovski, R.*; Antov, A.; Spassov, B.

2008, Romanian Astronomical Journal, Vol. 18, Supplement, p. 55-60

“Synchronous network of distant telescopes”

Zhilyaev, B.; Svyatogorov, O.; Verlyuk, I.; Andreev, M.; Sergeev, A.; Lovkaya, M.; Antov, A.; Konstantinova-Antova, R.; *Bogdanovski, R.*; Avgoloupis, S.; Seiradakis, J.; Contadakis, M. E.

2012, Bulgarian Astronomical Journal, V.18, No. 1, P.62

Talks and posters:

VI Serbian-Bulgarian Astronomical Conference 2008, Belgrade

Bogdanovski, R., Konstantinova-Antova, R.: “Photoelectric study of the flare activity of AD Leo”

SREAC, 2007, Athens

Konstantinova-Antova, R., Bogdanovski, R., Antov, A., Spassov, B.: “Flare Activity of AD Leo in the Period 2006 – 2007”

25 years NAO- Rozhen, SAB, 2006, Sofia

Bogdanovski, R., “Synchronous network of distant telescopes”

Citations found in ADS

“Fast colorimetry of the flare star EV Lacertae from UBVRI observations in 2004” – Zhilyaev et al., 2007

1. Godunova et al., 2008, *Communicating Astronomy with the Public 2007: Proceedings from the IAU/National Observatory of Athens/ESA/ESO Conference*, Athens, Greece, 8-11 October 2007, Christensen L. L., Zoulias M. & Robson, I. (eds.)
2. Kowalski et al., 2010, *ApJ Letters*, V.714, 1, P.L98-L102
3. Sharon et al., 2010, *ApJ*, V.718, 2, P.876-893
4. Hilton et al., 2010, *AJ*, V.140, 5, P.1402-1413
5. Dal & Evren, 2011, *AJ*, V.141, 2
6. Kowalski et al., 2011, *16-th Cambridge Workshop on Cool Stars, Stellar Systems, and the Sun. ASP Conference Series, Vol. 448*, proceedings of a conference held August 28- September 2, 2010 at the University of Washington, Seattle, Washington., Christopher M. Johns-Krull, Matthew K. Browning, and Andrew A. West. (eds), San Francisco: Astronomical Society of the Pacific, 2012., P.1157
7. Kowalski et al., 2012, *Solar Physics*, V.277, 1, P.21-29
8. Welsh et al., 2012, *New Horizons in Time-Domain Astronomy, Proceedings of the International Astronomical Union, IAU Symposium*, V.285, p.99-102
9. Kowalski et al., 2013, *ApJ Supplement*, V.207, 1

“Flare Activity of AD Leo in the Period 2006 - 2007” – Konstantinova-Antova et al, 2008

1. Buccino et al., 2014, ApJ Letters, V.781, 1, L9

“Synchronous network of distant telescopes” – Zhilyaev et al., 2012

1. Rieznik, K. & Rechetnyk, M., 2013, WDS'13 Proceedings of Contributed Papers, Part III, 13-18, ISBN 978-80-7378-252-8

Acknowledgements

I would like to express my deep respect to my advisor Prof. Dr. Renada Konstantinova–Antova for the encouragement and the invaluable help with this research. I also want to thank her and her husband Assoc. Prof. Dr. Alexander Antov for the warm welcome extended to me at the Belogradchik observatory when I showed up there as an eighth grader. They have been instrumental in guiding and supporting me in my astronomical endeavors ever since.

I want to thank Dr. Milcho Tsvetkov who was my first advisor and I want to apologize to him for not following his work.

I am grateful to Eng. Dr. Radik Gradinarski who helped me put together the first prototype of the Photon Counting Module and to Eng. Atanas Baldjiyski for the help with the hardware design and the assembly of the observational system described in this work.

I am grateful to Dr. Kostadinka Koleva and Assoc. Prof. Dr. Peter Duhlev for the fruitful discussions, to all the colleagues who helped with the observations and to the coauthors of the papers used in this work.

I want to express my gratitude to my parents Zdravka and Goshko Bogdanovski and my sister Biliana for their support during the years, but especially to my father who lit the spark of astronomy in me at a very young age.

I also want to express my deep respect, gratitude and love to my wife Mariana for her unconditional support and for being next to me no matter what. She endured many inconveniences because of my love for astronomy and yet was not resentful.

I want to say thank you to all the people not mentioned above, but who helped me with this thesis.

Appendices

” *An expert is a person who has made all the mistakes that can be made in a very narrow field.*

— **Niels Bohr**
Danish physicist

Manual of devsim

A

NAME

devsim – Software simulator of Photon Counting Module (PCM) for the Universal Electro photometer.

SYNOPSIS

```
devsim [options]  
devsim [options] >>logfile.log 2>&1 &
```

DESCRIPTION

This is a software simulator of the Photon Counting Module for the Universal Electro photometer. It is used for training. It is able to simulate variable star, check star, standard star, sky background etc. Different simulations are available by changing *integration tag* with command *setft* (see *photconsole(5)*). Here is the list of available tags:

- 0** Variable star simulation.
- 1** Standard star simulation.
- 2** Check star simulation.
- 3** Photometer dark current simulation.
- 4** Sky background light simulation.
- 5** Returns always 0.
- 6** Returns always 0x0000FF (in decimal).
- 7** Returns always 0xFF0000 (in decimal).

8 Returns always maximal 24-bit number in decimal.

9-14 Returns always 1010101.

OPTIONS

-s socket_file The socket file where devsim will listen. Default is /tmp/.s.phot

-v Verbose output, if not specified only errors will be printed.

-h Print simple help and exit.

EXAMPLES

The typical invocation of devsim: **devsim -v** To run it in background with output stored in photsrv.log: **devsim -v >>devsim.log 2>&1 &**

FILES

/etc/devsim.conf

SEE ALSO

devsimconf(5), photprotocol(5), photconsole(5)

BUGS

If you find any please contact the author.

AUTHOR

Rumen G.Bogdanovski
rumen@skyarchive.org

Configuration of devsim

NAME

devsim.conf – configuration file for devsim

SYNOPSIS

devsim.conf

DESCRIPTION

This file specifies the parameters of the output of the simulation of the Photon Counting Module for Universal Electro Photometer. The syntax of the file is simple. The format of the statements is:

keyword = value [comment]

or

keyword value [comment]

Both statements are equal. Keywords are case sensitive. The comment after the statement is optional. Comments may not start with # if they follow a statement on the same line. If comments are alone on the line # is necessary.

KEYWORDS

photometer.channels

Number of the channels of the simulated photometer (1 to 8).

photometer.chmap

Bitmap of the initially set to be used channels in decimal (value 3 (00000011 binary) represents channels 1 and 2).

var

Counts produced by the variable star when it is calm for integration of 0.01s.

var.flare.amplitude

Amplitude in counts of the flare of the variable star for integration of 0.01s.

var.flare.duration

Duration of the flare in 0.01 seconds (value of 100 represents 1s).

var.flare.symmetry

Symmetry of the flare is the ratio of fall/rise time. Value 1 indicates that the rise time is equal to the fall time.

var.flare.pause

The The pause between the flares in 0.01 seconds (value of 100 represents 1s). If this is set to 0 and **var.flare.symmetry** is set to 1, the output of the simulation will be sinusoidal.

standardstar

Counts produced by the standard star for integration of 0.01s.

checkstar

Counts produced by the check star for integration of 0.01s.

sky

Counts produced by the sky background for integration of 0.01s.

photometer.darkcurrent

Counts produced by the photometer dark current for integration of 0.01s.

noise

The amplitude of the random noise in percents (%) added to the integration data.

EXAMPLES

The typical devsim.conf file will look like:

```
# Example devsim.conf file
photometer.channels = 2
photometer.chmap = 1 # by default use only channel 1
photometer.darkcurrent = 30

var = 1000
var.flare.amplitude = 800
```

```
var.flare.duration = 1000  
var.flare.symmetry = 3  
var.flare.pause = 1000
```

```
standardstar = 800  
checkstar = 1000  
sky = 30  
noise = 3
```

SEE ALSO

devsim(8)

AUTHOR

Rumen G.Bogdanovski
rumen@skyarchive.org

Manual of photsrv

NAME

photsrv – server allowing TCP access to the Photon Counting Module for the Universal Electro photometer.

SYNOPSIS

```
photsrv [options]  
photsrv [options] >>logfile.log 2>&1 &
```

DESCRIPTION

photsrv is the user access server to the Photon counting module for Universal Electro photometer. It uses PHOT protocol (see photprotocol(5)) for the serial communication with the device and TCP protocol for the user access to the device. Only one user can control the device - the user with Read/Write access - usually the first one that is logged in to the system. All other users are Read Only and can only monitor the observation without the possibility to control it. If the user with Read/Write access closes the connection the next user who initiates connection will get the Read/Write access. For more information on the device console see photconsole(5).

OPTIONS

-p port

The TCP port where the server will listen. Default is 9090.

-r num

Maximum number of read only connections. Default is 5.

-d device

Device file of the serial port where Photon counting module is connected. Default on Linux is /dev/ttyS0, on SUN/Solaris is /dev/ttya.

-g gpsdevice/no

Device file of the serial port where Acutime 2000 GPS is connected. Default on Linux is /dev/ttyS1 on SUN/Solaris is /dev/ttyb. If **no** is specified, the GPS support is disabled. In this case the real time is received from the computer clock.

-l logfile

File where the server events will be stored. *YET NOT IMPLEMENTED*

-a yes/no

If **yes** IP access control list will be used. See photsrvacl(5). If the access control is not necessary, **no** should be specified.

-n yes/no

If **yes**, the types of the filters and the tags will be returned by the server as set in photsrvconf(5). If set to **no**, their numbers will be returned. In case there is no type set for a given filter or tag number the number will be returned regardless of this setting. Default is **yes**.

-j S/So/no

Configure auto adjustment of the speed of the device internal clock to minimize the difference with the GPS time. **S** is the number of seconds to wait between adjustments (use **no** or 0 to turn off auto adjustment). If **o** suffix of the number is used a single adjustment will be made **S** seconds after the photsrv startup. This option has effect only with GPS support enabled.

-J adjspeed

Set the convergence speed of the auto adjustment algorithm. This option accepts values between 0 and 1. The value of 1 means that the offset of the internal clock will be fully compensated in the time set by **autoadjust** or **-j** option. At value of 0.5 half of the offset will be compensated in the same time. The value of 0 invokes the old behavior of the algorithm with very slow compensation of the offset relying only on the rounding of the clock correction factor. This option has no effect if the auto adjustment is performed once or is disabled. The default value is **0.3**

-t delay

A floating point value to compensate the hardware time delays in micro seconds.

-s

Use software PCM device simulator. Not a real device. Option **-d** should be set to point the socket where devsim(8) listens. If **-d** not specified the default socket is used (/tmp/.s.phot). The **device** entry in photsrv.conf has no effect when **-s** switch is used. If this option is used, the GPS support is disabled, since devsim(8) can not control the GPS device.

-h

Print simple help and exit.

-v

Print version and build information and exit.

-D

Print debugging information.

EXAMPLES

The typical invocation of photsrv:

```
photosrv
```

To run it in background with output stored in photsrv.log:

```
photosrv >>photosrv.log 2>&1 &
```

FILES

/etc/photosrv.conf

/etc/photosrv.acl

SEE ALSO

photosrvconf(5), photosrvacl(5), photprotocol(5), photconsole(5), devsim(8)

BUGS

If you find any please contact the author.

AUTHOR

Rumen G.Bogdanovski
rumen@skyarchive.org

Configuration of photsrv

NAME

photsrv.conf – configuration file for photsrv

SYNOPSIS

photsrv.conf

DESCRIPTION

The syntax of the file is simple. The format of the statements is:

keyword = value [comment]

or

keyword value [comment]

Both statements are equal. Keywords are case sensitive. The comment after the statement is optional. Comments may not start with **#** if they follow a statement on the same line. If comments are alone on the line **#** is necessary. Exceptions are **observatory** and **equipment** keywords which are special kind of comments and no other comments are allowed on the same line after them.

KEYWORDS

port

The TCP port where the server will listen. Default is 9090.

roclients

Maximum number of read only connections. Default is 5.

device

Device file of the serial port where Photon counting module is connected. Default on Linux is `/dev/ttyS0`, on SUN/Solaris is `/dev/ttya`.

gpsdevice

Device file of the serial port where Acutime 2000 GPS receiver is connected. Default on Linux is /dev/ttyS0, on SUN/Solaris is /dev/ttya. If **gpsdevice** is set to **no**, the GPS support is disabled.

logfile

File where the server events will be stored. *YET NOT IMPLEMENTED*

autoadjust

Configure auto adjustment of the speed of the device internal clock to minimize the difference with the GPS time. **autoadjust** should be set to the number of the seconds between adjustments (use **no** or 0 to turn off auto adjustment). If **o** suffix of the number is used a single adjustment will be made **S** seconds after the photsrv startup. This keyword has effect only with GPS support enabled.

adjustspeed

Set the convergence speed of the auto adjustment algorithm. **adjustspeed** accepts values between 0 and 1. The value of 1 means that the offset of the internal clock will be fully compensated in the time set by **autoadjust** or **-j** option. At value of 0.5 half of the offset will be compensated in the same time. The value of 0 invokes the old behavior of the algorithm with very slow compensation of the offset relying only on the rounding of the clock correction factor. This option has no effect if the auto adjustment is performed once or is disabled. The default value is **0.3**

hwdelay

A floating point value to compensate the hardware time delays in micro seconds.

acl

If set to **yes** access control list will be used. See photsrvacl(5). If the access control is not necessary, **no** should be used (default).

returnfttypes

If **yes**, the types of the filters and the tags will be returned by the server, as set by **filter.n** and **tag.n**. If set to **no**, their numbers will be returned. In case there is no type set for a given filter or tag number the number will be returned regardless of this setting. Default is **yes**.

observatory

Description of the observatory, usually its name.

observatory.latitude

The observatory latitude in degrees. North is positive, South is negative. ([+-]dd:mm:ss.h)

observatory.longitude

The observatory longitude in degrees. East is positive, West is negative. ([+-]dd:mm:ss.h)

observatory.elevation

The observatory elevation in meters.

observatory.equipment

Description of the equipment used, telescope, photometer etc.

filter.n

String maximum 10 characters long representing the type of the filter installed on the position with number **n** on the filter holder. The value of **n** can be from 0 to 14. For example:

filter.3 = U

represents that on the third position of the filter holder U(ltraviolet) filter is installed. The filter type should not be a number.

tag.n

String maximum 10 characters long representing the type of the integration tag with number **n**, The value of **n** can be from 0 to 14. For example:

tag.0 = Var

represents that the tag number 3 is the tag of the Var(iable) star. The tag type should not be a number.

EXAMPLES

The typical photsrv.conf on SUN/Solaris will look like this:

```
# Example photsrv.conf
port = 9091
device = /dev/ttyb
gpsdevice = /dev/ttya
roclients = 0 do not allow read only clients
observatory A0 Belogradchik
observatory.equipment Zeiss600 & BUP1
```

```
observatory.latitude +1:00:00.0
observatory.longitude -1:00:00.0
observatory.elevation 0
filter.0 U
filter.3 B
filter.8 V
tag.0 Var
tag.1 H
tag.3 St1
tag.6 Dark
tag.2 Check
```

SEE ALSO

photosrv(8), photosrvac(5), photprotocol(5)

AUTHOR

Rumen G.Bogdanovski
rumen@skyarchive.org

Configuration of photsrv Access Control

NAME

photosrv.acl – Access control list configuration file for photsrv

SYNOPSIS

photosrv.acl

DESCRIPTION

The syntax of the file is simple. The format of the rules is:

keyword ip_address [ip_netmask]

or

keyword all

Keywords are case sensitive. The comment after the statement is not allowed. Comments should be alone on the line starting with # character. The policy is "deny", which means that all connections are denied if not explicitly allowed. The rules are processed in the order they appear in the file and the first matching rule will be applied. The keyword "all" is used to match all IP addresses. Maximum of 100 rules are allowed in the file.

KEYWORDS

rwallow

Allow read write connections from the host with specified IP address or network with specified network IP and netmask.

roallow

Allow read only connections from the host with specified IP address or network with specified network IP and netmask.

deny

Deny connections from the host with specified IP address or network with specified network IP and netmask.

EXAMPLES

The typical photsrv.acl will look like this:

```
# Example photsrv.conf

# allow RW connections
rwallow 127.0.0.1
rwallow 192.168.1.0 255.255.255.0

# allow RO connections
roallow 172.20.0.0 255.255.0.0

#deny any other connection
deny all
```

SEE ALSO

photosrv(8)

AUTHOR

Rumen G.Bogdanovski
rumen@skyarchive.org

Commands of photsrv

NAME

PHOT Console

DESCRIPTION

The PHOT console is provided by PHOT server (see `photosrv(8)`). The console is command line oriented. Only the Read/Write connection can execute commands. All other connections are Read Only and are not allowed to execute commands. They can only monitor the results.

On connect a welcome message is displayed and a configuration of the filters, integration tags and observatory data is dumped in the form described in `photosrvconf(5)` followed by a message describing the type of the initiated connection (read/write or read only).

SYNOPSIS

Each command is invoked by its name and the given parameters:

command [*param1*] [*param2*] ...

The result is presented by the command name followed by the returned values:

command [*result1*] [*result2*] ...

For example (see **devrdy**):

devrdy
devrdy Ok

The result of an unknown command invocation is the command typed followed by **Wrong Command**. For example:

foo

foo Wrong Command

The result of the invocation of a command with wrong parameters is the command typed followed by **Wrong Parameter**. For example (extra parameter in **integr** command):

integr 0.01 5 2

integr Wrong Parameter

The result of any command typed in Read Only session is **ro Session**. For example:

setft 2 6

ro Session

All commands are case sensitive and should be typed in lower case.

COMMANDS

devrdy

SYNOPSIS

devrdy

RETURNS

devrdy *Ok|Busy*

DESCRIPTION

Checks the status of the device. If the device is idle returns *Ok* else returns *Busy*.

devinfo

SYNOPSIS

devinfo

RETURNS

devinfo *ver.rev-nch*

ver – Firmware version.

rev – Firmware revision.

nch – number of channels supported by the device (from 1 to 8).

DESCRIPTION

The command returns version, revision and number of supported channels by the device.

chused

SYNOPSIS

chused

RETURNS

chused *chmap*

chmap – string containing "*" - for the channels set to be used and "-" - for the channels set not to be used. The length of the string is equal to the number of channels. "*—" shows that only channel 1 of total 4 channels will be used in the consequent integrations.

DESCRIPTION

Returns information of the channels which are set to be used in the next integrations.

usech

SYNOPSIS

usech *chstr*

chstr – string containing digits from 1 to number of channels supported. Each digit represents the number of the channel which is to be set to be used. Assuming 4 channel photometer, string "24" will set channel 2 and 4 to be used, and 1 and 3 will be set not be used.

RETURNS

usech *Ok|Busy*

DESCRIPTION

Sets the channels to be used and the channels not to be used in the consequent integrations according to *chstr*. On success *Ok* is returned. If the device is doing integrations or some other activity is performed *Busy* is returned.

integr

SYNOPSIS

integr *time num*

or

integr *time*

time – duration of the integrations in seconds (min 0.01, max 655.35).

num – number of repetitions (min 0 max 65535). 0 represents continuous integrations which can be stopped with **abort** command.

RETURNS

integr *Ok itime*

or

integr *Busy*

itime – integration time that is actually set with **integr** command.

DESCRIPTION

The command requests a number of marks of the object with a specified duration. If *num* is not specified continuous mode is assumed (*num* = 0). The execution begins with the **start** command. If the device is busy the command returns *Busy*. On success *Ok* and integration time is returned.

start

SYNOPSIS

start

RETURNS

start (000) *cm t_000 d_X_000 f_Xt_X [... d_Y_000 f_Yt_Y]*

start (001) *cm t_001 d_X_001 f_Xt_X [... d_Y_001 f_Yt_Y]*

...

start (*num*) *cm* *t_num* *d_X_num* *f_X* *m_X* [... *d_Y_num* *f_Y* *t_Y*]

start *Ready*

or

start *Busy*

001 - num – sequential numbers for each integration requested by **integr** used to find if there is any lost integration. The num will overflow at 255 and next mark will have num set to 0.

X - Y – growing numbers of channels presented in *cm*.

cm – used channel map. String of "*" and "-" characters with length equal to the total number of channels available. Used channels are shown with "*", unused with "-". Assuming 5 channel photometer string "-**-" represents that data is provided from channels 2,3 and 5. So *X* for this example will be 2 and *Y* will be 5.

t_000 - t_num – GMT time when each integration was made in format HH:MM:SS.FFF

d_X_000 - d_Y_num – data returned from each used channel for each integration.

f_X - f_Y – number or type of the filter used for the integrations for each used channel.

t_X - t_Y – number or type of the tag used for the integrations for each used channel.

DESCRIPTION

If the device is not busy the integrations requested with **integr** command are started. After each integration the data is returned. When all requested integrations are made *Ready* is returned. If the device is busy no integrations are made and *Busy* is returned.

abort

SYNOPSIS

abort

RETURNS **abort** *Ok*

DESCRIPTION

Aborts current actions and returns **Ok**.

rdram (OBSOLETE)

SYNOPSIS

rdram

RETURNS

nothing

DESCRIPTION

Does nothing.

rdft

SYNOPSIS

rdft *chstr*

or

rdft

chstr – string containing digits from 1 to number of channels supported. Each digit represents the number of the channel for which the data will be returned. Assuming 4 channel photometer, string "24" will return data for channels 2 and 4.

RETURNS

rdft *chmap* *f_X t_X* [... *f_Y t_Y*]

or

rdft *Error*

X – Y – growing numbers of channels listed in *champ*

chmap – channel map. String of "*" and "-" characters with length equal to the total number of channels available. Channels for which data is returned are shown with "*", all others with "-". Assuming 5 channel photometer string "-**-" represents that data is provided for channels 2,3 and 5. So *X* for this example will be 2 and *Y* will be 5.

$f_X - f_Y$ – numbers or types of the currently set filters for the requested channels.

$t_X - t_Y$ – numbers or types of the currently set integration tags for the requested channels.

DESCRIPTION

Returns the current filter and current tag for the channels specified in *chstr*. If *chstr* is omitted the data for the channels which are currently set to be used is returned.

setft

SYNOPSIS

setft *filter tag chstr*

or

setft *filter tag*

filter – number or type of the filter to be set. 15 represents the currently set one.

tag – number or type of the tag to be set. 15 represents the currently set one.

chstr – string containing digits from 1 to number of channels supported. Each digit represents the number of the channel for which the requested filter and tag will be applied.

RETURNS

setft *Ok|Busy|Error*

DESCRIPTION

The command sets the desired filter and integration tag for the channels listed in *chstr*. If *chstr* is omitted the filter and tag are set for the channels currently set to be used. If *filter* is 15 only *tag* is set (filter unchanged). If *tag* is 15 only the *filter* is set (tag unchanged). If the filter for some of the channels listed in *chstr* is not set and timeout occurs *Error* is returned. If the device is not idle *Busy* is returned. On success *Ok* is returned.

rdrt

SYNOPSIS

rdrt

RETURNS

rdrt *date time acc diff*

date – date from the device in format DD-MM-YYYY

time – GMT time from the device in format HH:MM:SS.FFF

acc – the accuracy of the device real time relative to the system real time in seconds.

diff – half of the time period from the command request till the the receiving of the result in seconds. If GPS support is enabled *diff* is in format "GPS:n" where n is the number of the state of the Accutime 2000 GPS receiver.

DESCRIPTION

Reads the device real time and calculates its offset from the system time.

setrt

SYNOPSIS

setrt

RETURNS

setrt *Ok diff*

or

setrt *Busy*

diff – half of the time period from the command request till the the receiving of the result in seconds. If GPS support is enabled *diff* is in format "GPS:n" where n is the number of the state of the Acutime 2000 GPS receiver.

DESCRIPTION

Sets the device real time if the device is not busy.

quit

SYNOPSIS

quit

RETURNS

nothing

DESCRIPTION

Closes the Read Write session.

SPECIAL COMMANDS

adjrt

SYNOPSIS

adjrt *factor*

factor – indicates in how many clock ticks (250us) the device internal clock should be corrected with a 100ns discrete. Positive values indicate addition, negative indicate subtraction.

RETURNS

Nothing. There is no reply from this command.

DESCRIPTION

This command is used by *photsrv* for the internal clock auto-adjustment. It sets the correction factor for the device internal clock and should be used to synchronize the device with a time standard. In clock auto-adjust mode *photsrv* uses this command to adjust the device internal clock speed.

rdrt2

SYNOPSIS

rdrt2

RETURNS

nothing

or

rdrt2 *date time acc diff adjfactor*

date – date from the device in format DD-MM-YYYY

time – GMT time from the device in format HH:MM:SS.FFF

acc – the accuracy of the device real time relative to the system real time in seconds.

diff – half of the time period from the command request till the the receiving of the result in seconds. If GPS support is enabled *diff* is in format "GPS:n" where n is the number of the state of the Acutime 2000 GPS receiver.

adjfactor – indicates in how many clock ticks (250us) the device internal clock is corrected with a 100ns discrete. Positive values indicate addition, negative indicate subtraction.

DESCRIPTION

This command is used by *photosrv* for the internal clock auto-adjustment. In clock auto-adjustment mode *photosrv* does not reply to this command but triggers adjustment procedure prematurely. If auto-adjustment is off, the command returns the data described above.

TELESCOPE COMMANDS

tc gotorade

SYNOPSIS

tc gotorade *ra de*

ra – righthascension in format HH:MM:SS.FFF

de – declination in format \pm DD:MM:SS.FFF

RETURNS

tc *Ok|Busy|Error*

DESCRIPTION

Slew the telescope to the specified *ra*, *de*. In case of invalid format or other error *Error* is returned. If the device is not idle *Busy* is returned. On success *Ok* is returned.

tc getrade

SYNOPSIS

tc getrade

RETURNS

tc *ra de*

or

tc *Error*

ra – right ascension in format HH:MM:SS.FFF

de – declination in format \pm DD:MM:SS.FFF

DESCRIPTION

Get the telescope current right ascension and declination. In case of error *Error* is returned. On success *Ok* is returned.

SEE ALSO

photosrv(8)

photprotocol(5)

AUTHOR

Rumen G. Bogdanovski
rumen@skyarchive.org.

NOTES

This page describes PHOT console version 1.1mc. Other versions may differ slightly.

Photon Counting Module (PCM) Communication Protocol

DESCRIPTION

This page describes the PHOT device protocol version 1.0 used by the Photon Counting Module for the Universal Electro photometer. The protocol supports up to 8 channel photometers.

DEVICE COMMANDS

DEVRDY - 0x01

PARAMETERS

–

RETURNS

OK, BUSY

DESCRIPTION

If the device is idle returns OK else returns BUSY.

DEVINFO - 0x21

PARAMETERS

–

RETURNS

1. *Firmware version.* – 8bit unsigned integer.
2. *Firmware revision.* – 8bit unsigned integer.
3. *Number of supported channels.* – 8bit unsigned integer. Valid values are from 1 to 8.

DESCRIPTION

This command returns the stated above information.

CHUSED - 0x22

PARAMETERS

–

RETURNS

1. *Channel Bitmap* – 8 bit. Each bit set indicates that the corresponding channel will be used when the consequent integrations are started. Bitmap 00000001 represents the first channel.

DESCRIPTION

The command returns a bitmap of the channels which are set to be used in the consequent integrations.

USECH - 0x23

PARAMETERS

1. *Channel Bitmap* – 8 bit. Each bit set indicates that the corresponding channel is requested to be set to be used when the consequent integrations are started. Bitmap 00000001 represents the first channel.

RETURNS

OK, BUSY

DESCRIPTION

The command sets the channels to be used in the consequent integrations. Those with bits set will be used and those with bits cleared will not be used. For example bitmap 00100101 requests only channels 1,3 and 6 to be used in the next integrations. On success the device returns OK. If integrations are performed or there is other activity, BUSY is returned.

INTEGR - 0x02

PARAMETERS

1. *Duration* – 16 bit fixed point in sec/100. The duration of each integration. (0.01 - 655.35 sec)

2. *Number of integrations (marks)* – 16 bit signed integer. If 0, repeat integrations until ABORT is received.

RETURNS

OK, BUSY

DESCRIPTION

The command requests a number of marks of the object with specified time. The execution begins with the START command. If the number of integrations is 0 the device loops marking till the ABORT command is received. If the device is busy the command returns BUSY.

START - 0x0B

PARAMETERS –

RETURNS

DATA, READY, BUSY

DATA:

0. *Channel bitmap* – 8 bit. Each bit set indicates that the data for the corresponding channel is present. Bitmap 00000001 represents the first channel. The Bitmap is located in the RID byte of the protocol.

1. *ID* – 8 bit integer. Number of the integration (0-255). If the number of integration is 255 next ID is 0.

2. *Time* – 32 bit fixed point in sec/1000. The offset in milliseconds from the last SETRT command.

3. *Data Array* of 32bit elements for each channel used for the integration specified in the channel bitmap. If channel bitmap is 00001010 the data array will contain 2 elements with data, one for channel 2 and one for channel 4. Each element contains: *Count* - 24 bit integer. Count of photons registered by the corresponding channel and *Filter and tag* - 8 bit, (4bit used filter code + 4bit data tag code).

DESCRIPTION

Starts the integrations requested with INTEGR command and returns DATA after each integration. When all integrations are over the device sends READY. If integrations are running, BUSY is returned.

ABORT - 0x04

PARAMETERS

–

RETURNS

OK

DESCRIPTION Aborts the started integration or series of integrations.

RDFT - 0x06

PARAMETERS

1. *Channel Bitmap* – Each bit set indicates that the data for the corresponding channel is requested. Bitmap 00000001 represents the first channel. Bitmap 00000000 requests data for the channels currently used. See USECH.

RETURNS I

1. *Channel Bitmap* – 8bit. Each bit set indicates that the data for the corresponding channel is present. Bitmap 00000001 represents the first channel.

2. *STATUS* – Array of 8bit elements One element per channel with its bit set in the channel bitmap. Each element represents current filter and integration tag for the channel - 8 bit (HI 4 bit filter + LO 4 bit integration tag). See START.

RETURNS II

ERROR

DESCRIPTION

Returns the current filter and integration tag (ie Dark current, Variable, Standard etc.) for each channel specified in the channel bitmap. If one or more filters were not properly set ERROR is returned.

SETFT - 0x07

PARAMETERS

1. *NEW STATUS* – 8 bit (4+4). See RDREG(STATUS).

2. *Channel bitmap* – 8bit. Each bit set indicates that the data should be applied for the corresponding channel. Bitmap 00000001 represents the first channel. Bitmap 00000000 applies the data to the channels currently used. See USECH.

RETURNS

OK, ERROR, BUSY

DESCRIPTION

The command sets the desired filter and integration tag for each channel with its bit set in the channel bitmap. If filter field is 0xf only the tag is set (filter unchanged). If tag field is 0xf only the filter is set (tag unchanged). If the filter is not set and the timeout occurs ERROR is returned. If the device is not idle, BUSY is returned and no action is performed.

RDRT - 0x08

PARAMETERS

–

RETURNS

1. *TIME* – The offset from the last execution of SETRT in seconds/1000 - 32 bit fixed point (sec/1000).

DESCRIPTION

Returns the pseudo-real time of the internal clock. See START->DATA(Time).

SETRT - 0x09

PARAMETERS

–

RETURNS

OK,BUSY

DESCRIPTION

Sets the pseudo-real time clock in the device to 0. If not idle fails with BUSY.

ADJRT - 0x24

PARAMETERS

1. *Correction factor* - 16bit signed integer. This is the factor indicating in how many clock ticks (250us) the device internal clock should be corrected with a 100ns discrete. Positive values indicate addition, negative indicate subtraction.

RETURNS

–

DESCRIPTION

Sets the correction factor for the device internal clock. This command should be used to synchronize the device clock speed with a time standard.

RDRT2 - 0x25

PARAMETERS

–

RETURNS

1. *TIME* – The offset from the last execution of SETRT in seconds/1000 - 32 bit fixed point (sec/1000).

2. *Correction factor* – 16bit signed integer. This factor indicates in how many clock ticks (250us) the device internal clock is corrected with a 100ns discrete. Positive values indicate addition, negative indicate subtraction.

DESCRIPTION

Returns the pseudo-real time of the internal clock and the correction factor for the device internal clock. This command should be used to provide data in order to synchronize the device with a time standard.

DEVICE REPLYs

Reply IDs (RID):

OK – 0x00

ERROR – 0x0B

BUSY - 0x0C

DATA - 0x0D

READY - 0x0E

COMMUNICATION PROTOCOL

Reply Packet Structure (device -> computer)

<DLE><CID><RID><data....><DLE><ETX>

DLE – 0x10

ETX – 0x03

CID – ID of the command which produced the packet (see **DEVICE COMMANDS**)

RID – Reply ID (see **DEVICE REPLY**)*

* START command is an exception it sets RID to Channel bitmap (instead of DATA) when data is returned.

Command Packet Structure (computer -> device)

<DLE><CID><data...><DLE><ETX>

DLE – 0x10

ETX – 0x03

CID – ID of the command which has to be executed (see **DEVICE COMMANDS**).

ADDITIONAL NOTES

2.1. Every <DLE> byte in the data string is preceded by an extra <DLE> byte ('stuffing'). These extra <DLE> bytes must be added ('stuffed') before sending a packet and removed ('unstuffed') after receiving the packet.

2.2. A simple <DLE><ETX> sequence does not necessarily signify the end of the packet, as these can be bytes in the middle of a data string. The end of a packet is <ETX> preceded by an odd number of <DLE> bytes.

2.3. Multiple-byte numbers (integer, fixed point) are sent least-significant-byte-first. This may involve switching the order of the bytes for some machines.

2.4. On wrong or unknown command device returns packet ERROR with CID also set to ERROR (see example 4).

EXAMPLES

1. OK reply from SETRT command:

```
<0x10><0x09><0x00><0x10><0x03>
```

2. Reply from start command when the second channel is used and 2 integrations are requested:

```
<0x10><0x0B><0x02><0x00><TIME><TIME><TIME><TIME><DATA><DATA>
```

```
<DATA><FILTER+TAG><0x10><0x03>
```

```
<0x10><0x0B><0x02><0x01><TIME><TIME><TIME><TIME><DATA><DATA>
```

```
<DATA><FILTER+TAG><0x10><0x03>
```

```
<0x10><0x0B><0x0E><0x10><0x03>
```

3. Request three 0.02 sec long integrations:

```
<0x10><0x02><0x02><0x00><0x03><0x00><0x10><0x03>
```

4. Unknown command reply:

```
<0x10><0x0B><0x0B><0x10><0x03>
```

AUTHOR

This protocol was developed by Rumen G. Bogdanovski.

Send your feedback to rumen@skyarchive.org.

NOTES

This page describes protocol version 1.0 from 22-Sep-2006. Other versions may differ slightly.

Batch Scripting for photclient

NAME

Writing batch scripts for photclient

DESCRIPTION

Batch scripts for photclient provide a way for automation of the observations using some of the PHOT console commands (see photconsole(5)) and several additional batch commands.

SYNOPSIS

Each command is invoked by its name and the given parameters:

command [*param1*] [*param2*] ...

All commands are case sensitive.

ALLOWED PHOTCONSOLE COMMANDS

usech

integr

start

setft

tc gotorade

tc gettrade

For description of the commands see Appendix F.

BATCH COMMANDS

All batch commands start with dot(.) to be distinguished by other commands.

.pause

SYNOPSIS

.pause

DESCRIPTION

The command stops batch execution while the button "Continue" is pressed.

.message

SYNOPSIS

.message *text*

text – text message to be displayed.

DESCRIPTION

The command stops batch execution and shows dialog window with the *text* given as parameter. After confirmation the execution resumes.

.messageb

SYNOPSIS

.messageb *text*

text – text message to be displayed.

DESCRIPTION

The command is the same as **.message**, but in addition the computer bell is ring.

LOOPS

The loops are constructed with the the combination of two keywords as shown below.

```
.repeat [N]  
    ...  
.end
```

The block enclosed between **.repeat** and **.end** is repeated *N* times. If 0 or no parameter is specified the loop will be endless and can be stopped by pressing "Abort" button. Nested loops are also possible.

COMMENTS

The lines starting with **#** are ignored by the batch processor and are considered as comments.

EXAMPLE SCRIPT

```
# The program makes three series of five
# measurements of the variable (Var) star
# in Ultraviolet (U) and Blue (B) bands using
# integration times of 1 sec.
integr 1 5
.message Point the telescope to Var!
.repeat 3
    setft U Var
    start
    setft B Var
    start
.end
```

SEE ALSO

photconsole(5)

AUTHOR

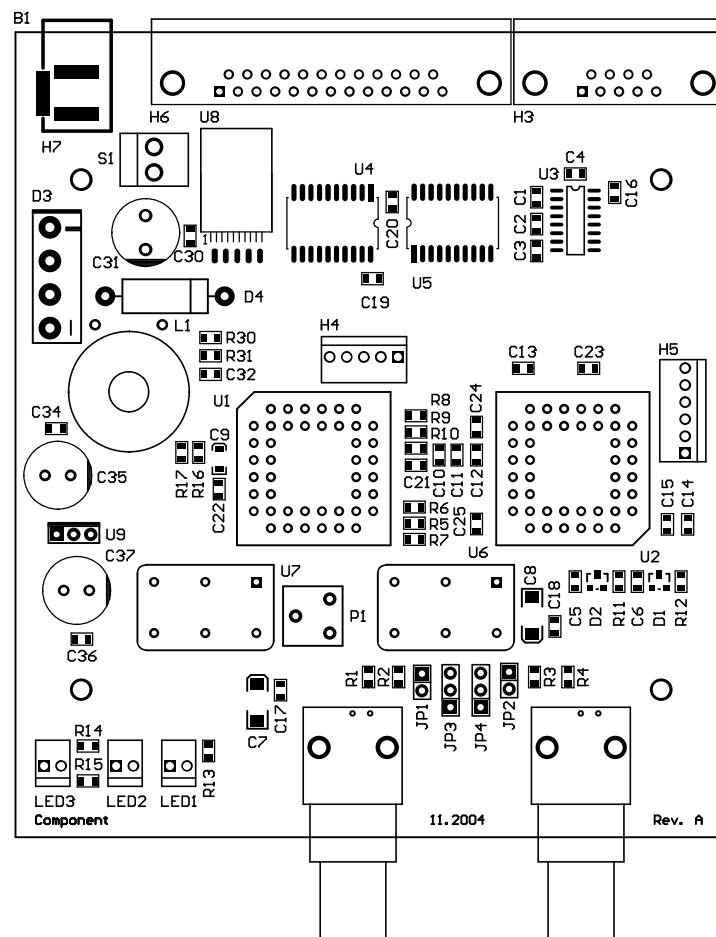
Rumen G.Bogdanovski
rumen@skyarchive.org.

NOTES

This page describes photclient batch scripting version 0.99. Other versions may differ slightly.

2 Channel Photon Counting Module (PCM2) Hardware User's Guide

Main board layout



External connectors

Input signal connectors(H1 H2)

BNC type connectors are used as input signal connectors. There is one connector for each channel. Inputs are configurable to accept ECL or TTL signals.

H1	Signal connector for channel 1
H2	Signal connector for channel 2

Data transfer interface(H3)

This interface is used to transfer data between the computer and the PCM using RS-232 serial line with standard DB-9 connector.

General purpose interface(H6)

This connector is used for several purposes, filter wheel control and signal transfer between the device and the Acutime 2000 GPS receiver.

Power connector(H7)

The device accepts AC or DC input voltage from 9V to 24V, 300mA.

Maintenance connectors

There are two maintenance connectors H4 and H5. H4 is used for the MCU (U1) software update and H5 is used for programming the CPLD (U2). For the software update special programming devices are required (not shipped with PCM).

Jumper configuration

Internal 50 Ω terminator (JP1 JP2)

PCM can operate with terminated and non-terminated BNC cables for the input signal. Each channel is configured separately, according to the following tables.

JP1	Channel 1
JP2	Channel 2

ON	Switch on the internal 50 Ω terminator
OFF	Switch off the internal terminator (if the cable is terminated)

Signal source selection (JP3 JP4)

Each channel of PCM can be configured to count the pulses from the Internal oscillator U6 (if it is present). This mode is only for test purposes.

JP3	Channel 1
JP4	Channel 2

1-2	BNC Connector
2-3	Internal generator (debugging mode)

PPS synchronized measurements mode

The PCM measurements can be synchronized with the PPS pulses from the GPS receiver. In this mode the PCM will always start the measurements precisely with the start of a new second.

To enable this mode, connect the PCM to the PPS output of the GPS receiver and switch the PCM on after the PPS pulses appear. If there are no PPS pulses on PCM startup this mode will not be activated and the measurements will start just after the measurement command has been sent. The PPS pulses must be compliant with the TTL levels with an active rising edge. Non TTL compliant pulses may damage the PCM.

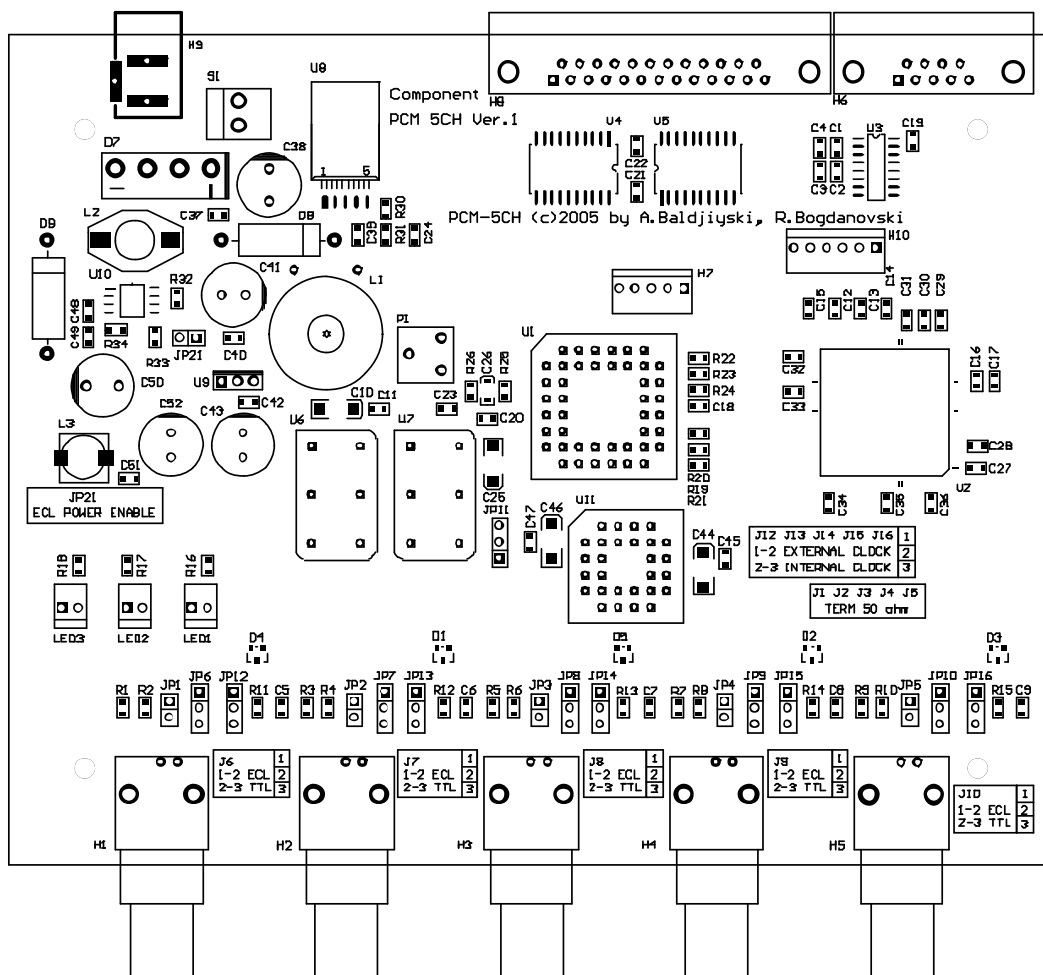
Specifications

Min. integration time	0.01 sec
Max. integration time	655.35 sec
Integration time increment	0.01 sec
Resolution of the internal real time clock	0.001 sec
Time synchronization drift (with GPS)	$< \pm 2\mu\text{sec}$ ($\leq \pm 0.6\mu\text{sec}^*$)
Time adjustment resolution	$0.1\mu\text{sec}$
Counter max. value (per channel)	2^{24}
Input signal level	TTL
Communication interface	9pin RS-232 at 115,2 kbps
Power supply	AC/DC 9 – 24V 300mA

* As measured, never seen to exceed this value.

5 Channel Photon Counting Module (PCM5) Hardware User's Guide

Main board layout



External connectors

Input signal connectors(H1 H2 H3 H4 H5)

BNC type connectors are used as input signal connectors. There is one connector for each channel. Inputs are configurable to accept ECL or TTL signals.

H1	Signal connector for channel 1
H2	Signal connector for channel 2
H3	Signal connector for channel 3
H4	Signal connector for channel 4
H5	Signal connector for channel 5

Data transfer interface(H6)

This interface is used to transfer data between the computer and the PCM using RS-232 serial line with standard DB9 connector.

General purpose interface(H8)

This connector is used for several purposes - filter wheel control and signal transfer between the device and the Acutime 2000 GPS receiver.

Power connector(H9)

The device accepts AC or DC input voltage from 9V to 24V, 300mA.

Maintenance connectors

There are two maintenance connectors H7 and H10. H7 is used for the MCU (U1) software update and H10 is used for programming the CPLD (U2). For the software update special programming devices are required (not shipped with PCM).

Jumper configuration

Internal 50 Ω terminator (JP1 JP2 JP3 JP4 JP5)

The PCM can operate with terminated and non-terminated BNC cables for the input signal. Each channel is configured separately, according to the following tables.

JP1	Channel 1
JP2	Channel 2
JP3	Channel 3
JP4	Channel 4
JP5	Channel 5

ON	Switch on the internal 50 Ω terminator
OFF	Switch off the internal terminator (if the cable is terminated)

Input signal logic levels selection (JP6 JP7 JP8 JP9 JP10)

ECL or TTL input signal levels are accepted. Signal levels are configurable separately for each channel, but all of the channels must be configured to accept the same type of signals, ECL and TTL must **not** be mixed. When JP6-JP10 settings are changed, JP11 must be changed also.

JP6	Channel 1
JP7	Channel 2
JP8	Channel 3
JP9	Channel 4
JP10	Channel 5

1-2	ECL input signal
2-3	TTL input signal

Signal source selection (JP12 JP13 JP14 JP15 JP16)

Each channel of the PCM5 can be configured to count the pulses from the Internal oscillator U6 (if it is present). This mode is only for test purposes.

JP12	Channel 1
JP13	Channel 2
JP14	Channel 3
JP15	Channel 4
JP16	Channel 5

1-2	BNC Connector
2-3	Internal generator (debugging mode)

Output enable/disable of the ECL to TTL converter (JP11)

If the PCM inputs are configured for TTL input signals this jumper must be set disabled, whereas for ECL it must be set enabled. This JP11 must be changed together with JP6-JP10.

1-2	Enable TTL output
2-3	Disable TTL output

NOTE: Pin 3 of JP11 is the one closest to C25.

Enable/Disable ECL circuit power (JP21)

If all channels are configured to work with TTL input levels, the power of the ECL circuit can be switched off by JP21.

ON	Enable ECL circuit power
OFF	Disable ECL circuit power

Configuring PCM to accept ECL or TTL input signals

Configuring inputs to accept ECL or TTL signals is achieved by setting seven jumpers according to the following table.

Jumper						ECL	TTL
JP6	JP7	JP8	JP9	JP10	JP11	1-2	2-3
JP21						ON	OFF*

* ON is also Ok, if JP11 is set to *disabled*(2-3).

IMPORTANT: The only valid combinations of JP6 – JP11 settings are listed in the above table, any other combinations may result in unpredictable behaviour and even in a device damage.

PPS synchronized measurements mode

The PCM measurements can be synchronized with the PPS pulses from the GPS receiver. In this mode the PCM will always start the measurements precisely with the start of a new second.

To enable this mode, connect the PCM to the PPS output of the GPS receiver and switch the PCM on after the PPS pulses appear. If there are no PPS pulses on PCM startup this mode will not be activated and the measurements will start just after the measurement command has been sent. The PPS pulses must be compliant with the TTL levels with an active rising edge. Non TTL compliant pulses may damage the PCM.

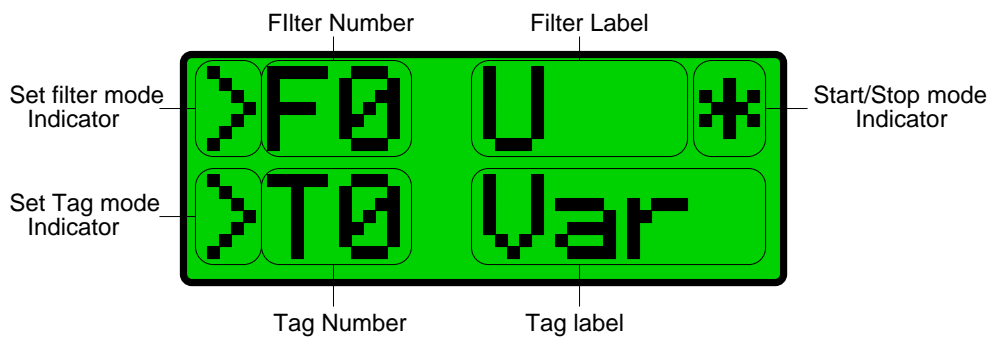
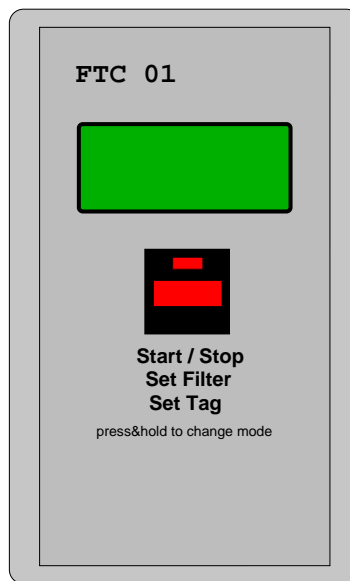
Specifications

Min. integration time	0.01 sec
Max. integration time	655.35 sec
Integration time increment	0.01 sec
Resolution of the internal real time clock	0.001 sec
Time synchronization drift (with GPS)	$< \pm 2\mu\text{sec}$ ($\leq \pm 0.6\mu\text{sec}^*$)
Time adjustment resolution	$0.1\mu\text{sec}$
Counter max. value (per channel)	2^{24}
Input signal level	TTL / ECL
Communication interface	9pin RS-232 at 115,2 kbps
Power supply	AC/DC 9 – 24V 300mA

* As measured, never seen to exceed this value.

Filter & Tag Control Unit (FTC 01) Operation

Panel View



Operation

The Panel allows three operations to be performed: Set the desired filter, set the desired tag and to start or stop the preset measurements. If there is no Photon

Counting module (PCM) connected, only setting of the filter is possible, since other operations have no meaning in this mode. If so the display says "No PCM" as shown on the picture below.



If any action is performed by the PCM or the filter revolver, the busy indicator (the red LED above the button) is blinking.

Set Filter

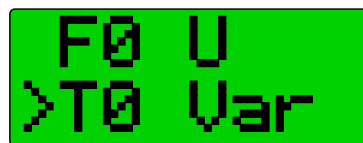
Press and hold the button until the set filter mode indicator is displayed.



In this mode each button press shorter than 0.5 sec will set the next filter, if both PCM and Filter revolver are not busy.

Set Tag

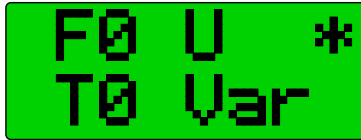
Press and hold the button until the set tag mode indicator is displayed.



In this mode each button press shorter than 0.5 sec will set the next tag, if both PCM and Filter revolver are not busy.

Start/Stop measurements

Press and hold the button until the start/stop mode indicator is displayed.



In this mode each button press shorter than 0.5 sec will start (if not started) or stop (if already started) the preset measurements. If the Filter revolver is moving the button press will not have any effect.

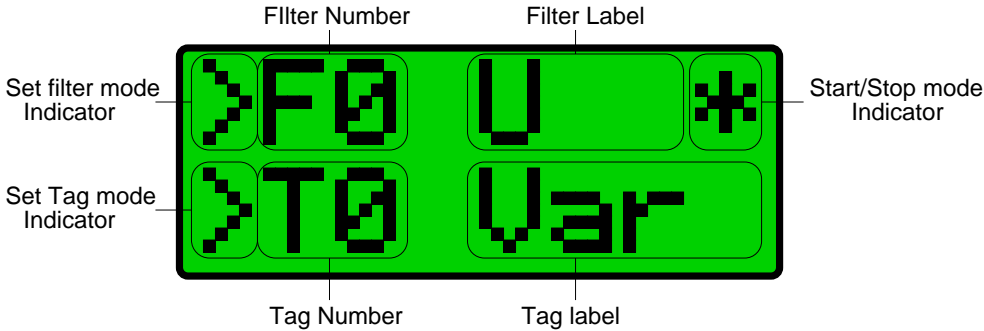
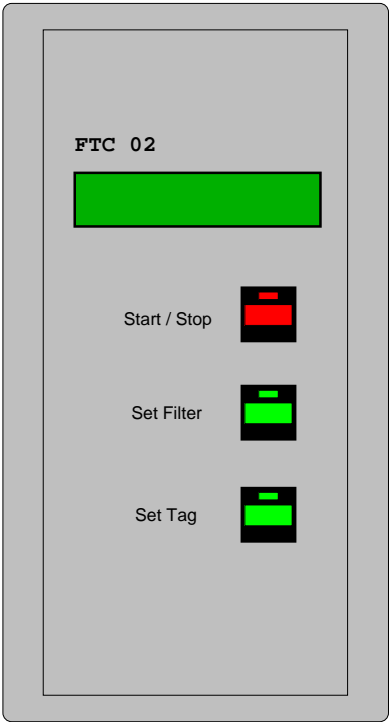
Additional Notes

1. In start/stop mode button press will not start any batch scripts loaded in phot-client. It will start only the previously set measurement.
2. If photclient is running a batch script pressing the button in start/stop mode will abort script execution. Pressing it again will not restart it.
3. If no integration is set with the command *integr* (see *photconsole(8)*) the the button press in start/stop mode will not start any measurements.

Filter & Tag Control Unit (FTC 02) Operation



Panel View



NOTE: FTC 01 display is shown, but there is no principal difference with the one installed here.

Operation

The Panel allows three operations to be performed: Set the desired filter, set the desired tag and to start or stop the preset measurements. If there is no Photon Counting module (PCM) connected, only setting of the filter is possible, since other operations have no meaning in this mode. If so the display says "No PCM".

If any action is performed by the PCM or the filter revolver, the busy indicators (the red and green LEDs above the buttons) are blinking.

Set Filter

Each press of the **Set Filter** will set the next filter, if both PCM and Filter revolver are not busy.

Set Tag

Each press of the button **Set Tag** will set the next tag, if both PCM and Filter revolver are not busy. In case there is no PCM connected this button has the same function as the **Set Filter** button.

Start/Stop measurements

Each press of the button **Start/Stop** will start (if not started) or stop (if already started) the preset measurements. If the Filter revolver is moving the button press will not have any effect. In case there is no PCM connected this button has the same function as the **Set Filter** button.

Additional Notes

1. In start/stop mode button press will not start any batch scripts loaded in phot-client. It will start only the previously set measurement.
2. If photclient is running a batch script pressing the button in start/stop mode will abort script execution. Pressing it again will not restart it.
3. If no integration is set with the command *integr* (see photconsole(8)) the the button press in start/stop mode will not start any measurements.

4. In case there is no PCM connected all buttons have the same function as the **Set Filter** button.

Communication between Photon Counting Module and Filter & Tag Control Unit

Communication Protocol

Photon Counting Module (PCM) and Filter & Tag Control Unit (FTC) communicate using commands sent by PCM and replies sent by FTC back to PCM and additional set of signals. There must be a reply to each command, but replies will also be initiated if the filter or tag is changed using the FTC panel. This is done in order to make PCM always aware of the current state of FTC.

PCM Outputs

PCM_BUSY

This signal gives information about the PCM status to FTC. If PCM is performing measurements this signal is set to '1'. On idle it is set to '0'.

PCM_REQ

The signal gives read data request to FTC. Before rising this signal PCM_OA0 – PCM_OA1 and PCM_OD0 – PCM_OD2 should be set.

PCM_OA0 – PCM_OA1

The address of the FTC command register to be written (2 bits).

PCM_OD0 – PCM_OD2

The data to be written to the FTC command register (3 bits).

GPS_EVENT

This signal gives EVENT signal to Acutime 2000 GPS Receiver.

PCM Inputs

FB_NOT_BUSY

This signal gives information to PCM about the status of FTC. If busy the signal is '0', else it is '1'.

FB_READY

This signal tells PCM whether FTC has finished the requested operation. Before rising this signal FTC sets the result of the operation in PCM_ID0 – PCM_ID2.

FB_BUTTON

This signal is raised for approximately 10ms if the Start/Stop button of FTC is pressed.

FB_NOT_PRESENT

This signal should be always set to '0' when FTC is connected to the PCM. This indicates the presence of FTC. If nothing is connected PCM reads it as '1'.

PCM_ID0 – PCM_ID2

The data to be read from FTC containing the result of the requested operation.

GPS_PPS

Pulse Per Second signal from the GPS receiver.

FTC Commands and Replies

Command Structure



A0 Channel selector. Must be '0' for channel 1 and '1' for channel 2.

A1 Mode selector. Must be '0' for filter manipulation and '1' for tag manipulation.

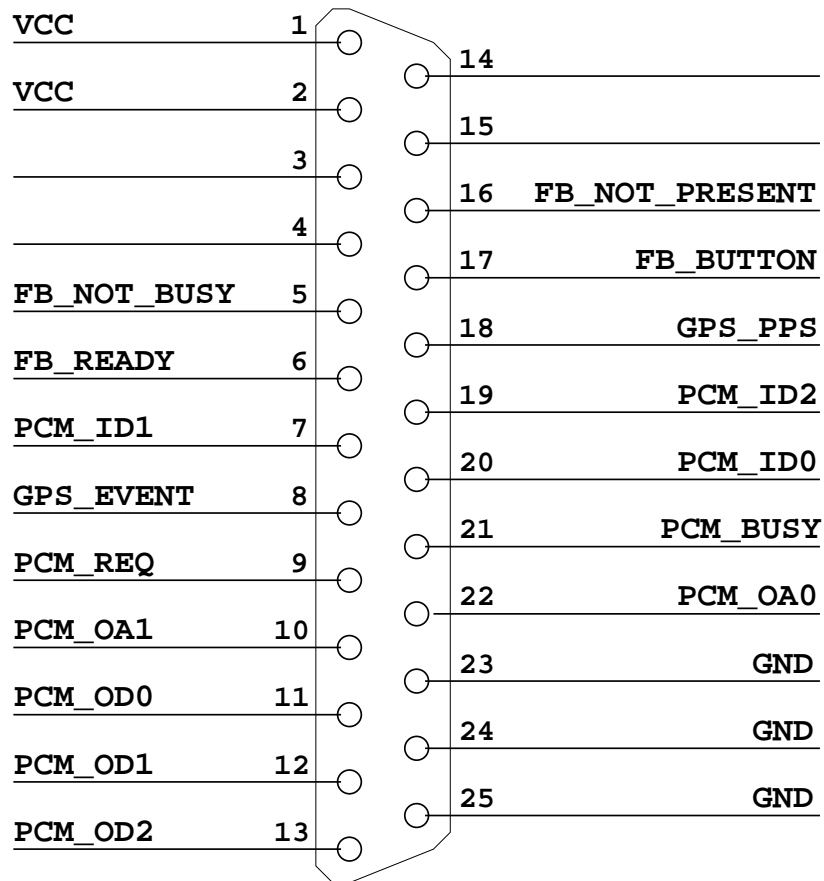
D0 – D2 For $D0 - D2 \in [000, 110]$ requests filter/tag with the given here number to be set. For $D0 - D2 = 111$ requests the number of the currently set filter/tag.

Reply Structure

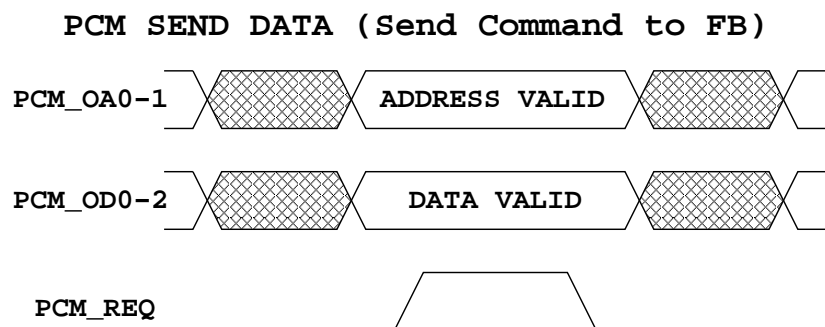
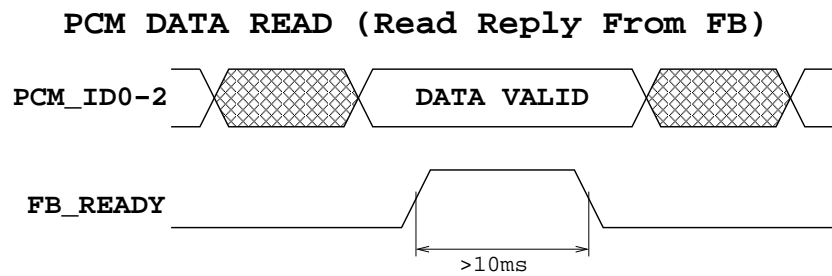


D0 – D2 If $D0 - D2 \in [000, 110]$, D0–D2 is the number of the currently set filter or tag, depending on the request which provoked the replay. If $D0 - D2 = 111$ the requested action ended with error.

PCM-FTC-GPS Connector Pinout



Timing Diagrams



Additional Notes

1. All command sent while FB_NOT_BUSY=0 will be ignored. FTC is not responsive when busy.
2. If FTC has only one filter revolver, PCM_OA0 is ignored.
3. The presence of PCM is detected by FTC using the presence of VCC on pins 1 and 2.

References

- Alekseev, I., & Gershberg, R., 1997, In: *The Earth and the Universe*, Eds. Asteriadis, G., Bantelas, A., Contadakis, M., Katsambalos, K., Papadimitriou, A., & Tsiavos, I., Aristotle University of Thessaloniki, Thessaloniki, Ziti Editions, p. 53
- Allred, J. C., Hawley, S. L., Abbett, W. P., Carlsson, M., et al., 2006, *ApJ*, 644, 484
- Antov, A., Pamukchiev, I., Svyatogorov, O., Bogdanovski, R., Parov, I., Kotsev, N., Konstantinova–Antova, R., Nashvadi, Y., 2001 *Balkan Mmeeting of Young Astronomers Proceedings*, 226–236
- Antov A. & Konstantinova–Antova R., 1995, in: *Robotic observatories*, edited by M.F. Bode, 69, Praxis Publishing Ltd, Chichester, England
- Athay, R. & Moreton, G., 1961, *ApJ*, 133, 935
- Basri, G., 2001, in *11th Cambridge Workshop on Cool Stars, Stellar Systems and the Sun*, ASP Conference Proceedings, V.223, Ramon J. Garcia Lopez, Rafael Rebolo, and Maria Rosa Zapaterio Osorio (eds), Astronomical Society of the Pacific, ISBN: 1-58381-055-2, P.261
- Benedict, G. F., Nelan, E., McArthur, B., Story, D., van Altena, W., Ting-Gao, Y., Jefferys, W. H., Hemenway, P. D., Shelus, P. J., Whipple, A. L., Franz, O. G., Fredrick, L. W., Duncombe, R. L., 1993, *Astronomical Society of the Pacific*, V.105, P.487-493
- Bopp, B., & Espenak, F., 1977, *Astronomical Journal*, V.82, P.916
- Bopp, B., & Fekel, F., 1977, *Astronomical Journal*, V.82, P.490
- Chabrier, G., & Baraffe, I. 1997, *A&A*, 327, 1039

- Crespo-Chacon, I., Montes, D., Garcia-Alvarez D., Fernandez-Figueroa M., Lopez-Santiago J., Foing, B., 2006, *A&A*, 452 (3), 987–1000
- Daubechies, I., 1990, *IEEE Trans. Inform. Theory*, 36, 961–1004
- Dhillon, V. S.; Marsh, T. R.; Stevenson, M. J.; Atkinson, D. C.; Kerry, P.; Peacocke, P. T.; Vick, A. J. A.; Beard, S. M.; Ives, D. J.; Lunney, D. W.; McLay, S. A.; Tierney, C. J.; Kelly, J.; Littlefair, S. P.; Nicholson, R.; Pashley, R.; Harlaftis, E. T.; O'Brien, K., 2007, *MNRAS*, V.378, P.825-840
- Donati, J.-F., Morin, J., Petit, P., Delfosse, X., Forveille, T. et al. 2008, *MNRAS*, 390, 545
- Favata, F., Micela, G., Reale, F., 1999, *A&A*, 354, 1021
- Farge, M., 1992, *Annu. Rev. Fluid Mech.*, 24, 395–457.
- Fleming, T. A., Giampapa, M. S., Schmitt, J., 2000, *ApJ*, V.533, P.372-377
- Gershberg, R. E., 1970, *Вспышки красных карликовых звезд*, Москва, Наука
- Gershberg, R. E., 2002, *Активность солнечного типа звезд главной последовательности*, ISBN9665498266
- Gershberg, R. E., 2005, *Solar-type activity of main sequence stars* (Heidelberg: Springer), 494
- Gershberg, R. E., Katsova, M. M., Lovkaya, M. N., Terebizh, A. V., Shakhovskaya, N. I., 1999, *A&A Suppl.*, V.139, P.555-558
- Giampapa, M. S., 1983, in *Solar and stellar magnetic fields: Origins and coronal effects*, Proceedings of the Symposium, Zurich, Switzerland, August 2-6, 1982 (A84-42426 20-90)., P.187
- Gizis, J., Monet, D., Reid, I., Kirkpatrick, J., Liebert, J., Williams, R., 2000, *Astronomical Journal*, V.120, P.1085-1099
- Gliese, W. and Jahreiss, H., 1991, *Preliminary Version of the Third Catalogue of Nearby Stars*.
- Gordon, K. & Kron, G., 1949, *Publ. of the Astronomical Society of the Pacific*, 61 (362): 210–214

- Gudel, M., Audard, M., Guinan, E. et al., 2001, in Proc. of "X-ray astronomy 2000", ASP Conf. Ser.vol. 234, R. Giacconi, L. Stella, S. Serio (eds)
- Guo, T., Ding, M.D., Schmieder, B., Demoulin, P., Li, H., 2012, ApJ, 746:17
- Hamamatsu Photonics K.K., "Photomultiplier tubes - Basics and Applications", 3rd Edition, Hamamatsu Photonics, Electron Tube Division
- Hartmann, L. & Noyes, R., 1987, Ann.Rev.Astron. Astrophys., V.25, P.271
- Hawley, S. L., Gizis, J. E., Reid, I. N., 1996, Astronomical Journal V.112, P.2799
- Herbig, G. H., 1956, Publ. of the Astronomical Society of the Pacific, V.68, P.531
- Herbst, W. & Miller, R., 1989, Astronomical Journal, V.97, P.891-899
- Hunt-Walker, N., Hilton, E., Kowalski, A., Hawley, S. and Matthews, J., Publ. of the Astr. Soc. of the Pacific, 2012, 124, 545-551
- Jenkins G.M. & Watts D.G., 1969, Spectral Analysis and its Applications, (Holden-Day: San Francisco)
- Johns-Krull, C. M., & Valenti, J. A. 1996, ApJ, 459, L95
- Joy, A, H., Abt, H. A., 1974, Astronomical Journal V.112, P.2799
- Joy, A. & Humason, M., 1949, Publ. of the Astronomical Society of the Pacific, V.61, 133
- Kaiser, G., 1994: A Friendly Guide to Wavelets. Birkhauser, 300 pp.
- Kaiser J.F. & Reed W.A., 1977, Rev. Sci. Instrum. 48, No. 11, 1447
- Kalmin S.Yu. & Shakhovskoy D.N., 1995, Kinematika i Fizika Nebesnyh Tel, 11, No. 3, 85
- Katsova, M. M., Boiko, A. Ya., Livshits, M. A., 1997, A&A, 321, 549
- Kellett, B., Bromage, G., Brown, A., Jeffries, R., James, D., Kilkenney, D., Robb, R., Wonnacott, D., Lloyd, C., Clayton, C., 1995, ApJ, V.438, P.364-375

- Konstantinova–Antova, R.K., Antov, A.P., 1995, in Proc. of the IAU Colloquium No. 151 "Flares and Flashes", Lecture Notes in Physics; vol. 454, J. Greiner, H. Duerbeck, R. Gershberg (eds), 87
- Kouprianova, E. G., Tsap, Y. T., Kopylova, Y. G., Stepanov, A. V., 2004, in Multi-wavelength investigations of solar activity (Cambridge Univ. Press), ed. A. V. Stepanov et al., Proc. IAU Symp., 223, 391
- Krishnamurthi, A., Terndrup, D. M., Linsky, J. L., Leto, G., 2001, in 11-th Cambridge Workshop on Cool Stars, Stellar Systems and the Sun, Proceedings, V.223, R.J. Garcia Lopez, R. Rebolo and M. R. Zapaterio Osorio., ISBN: 1-58381-055-2, P.1538
- Leinert, C., Henry, T., Glindemann, A., McCarthy, D. W., Jr., 1997, A&A V.325, P.159-166
- Liebert, J., Kirkpatrick, J., Reid, I., Fisher, M., 1999, ApJ, V.519, P.345-353
- Liller, W., 1952, Publ. of the Astronomical Society of the Pacific, V.64, P.129
- Linsky, J. L., Wood, B. E., Brown, A., Giampapa, M. S., Ambruster, C., 1995, ApJ, V.455, P.670
- Lippincott, S. L., 1969, Astronomical Journal, V.74, P.224-228
- Lippincott, S. L., 1983, N: Activity in red-dwarf stars; Proceedings of the Seventy-first Colloquium, Catania, Italy, August 10-13, 1982 (A83-47476 23-90). Dordrecht, D. Reidel Publishing Co., 1983, p. 201, 202.
- Liu, Chang; Deng, Na; Lee, Jeongwoo; Wiegelmann, Thomas; Jiang, Chaowei; Dennis, Brian R.; Su, Yang; Donea, Alina; Wang, Haimin, 2014, ApJ, V.795
- Luyten, W., 1949, ApJ, V.109, P.532
- Marcy, G. & Chen, G., 1992, ApJ, V.390, P.550
- Mavridis L.N., Asteriadis G. and Mahmoud F.H., 1982, in: Compendium in Astronomy, eds. E.G. Mariolopoulos, B.S. Theocaris and L.N. Mavridis, 253, Reidel Dordrecht

- Meyers, S. D., B. G. Kelly, and J. J. O'Brien, 1993, An introduction to wavelet analysis in oceanography and meteorology: With application to the dispersion of Yanai waves. *Mon. Wea. Rev.*, 121, 2858–2866.
- Mirzoyan, L. V., Hambarian, V. V., Garibjanian, A. T., Mirzoyan, A. L., 1988, *Астрофизика*, V.29, P.44
- Moreton, G. E. & Ramsey, H. E., 1960, *Publ. of the Astronomical Society of the Pacific*, 72, 357
- Morin, J., Donati, J.-F., Petit, P., Delfosse, X., Forveille, T. et al., 2008, *MNRAS*, 390, 567–581
- Morin, J., Donati, J.-F., Petit, P. et al. 2010, *MNRAS*, 407, 2269
- Neuhauser, R. & Comeron, F., 2001, in 11th Cambridge Workshop on Cool Stars, Stellar Systems and the Sun, ASP Conference Proceedings, V.223, Ramon J. Garcia Lopez, Rafael Rebolo, and Maria Rosa Zapaterio Osorio (eds), *Astronomical Society of the Pacific*, ISBN: 1-58381-055-2, P.1097
- Oppenheimer, B. R., Golimowski, D. A., Kulkarni, S. R., Matthews, K., Nakajima, T., Creech-Eakman, M., Durrance, S. T., 2001, *The Astronomical Journal*, V.121, 4, PP.2189-2211
- Osten, R. A., Hawley, S. L., Allred, J. C., et al. 2005, *ApJ*, 621, 398
- Petit, M., 1954, *Ciel et Terre*, No 11-13, P.3
- Petit, M., 1955, *Journal Obs.*, V.38, P.354
- Petit, M., 1957, *Астрон. журнал*, V.34, P.805
- Petit, M., 1958, *Contr.Osserv.Astrofisico Univ. Padova in Asiago*, V.95, P.29
- Petit, M., 1959, *Переменные звезды*, V.12, P.4
- Petit, M., 1961, *Journal Obs.*, V.44, P.11
- Pettersen, B., 1980, *A&A* 80, 53
- Pettersen, B., 1991, *Societa Astronomica Italiana*, (ISSN 0037-8720), V.62, P.217-242

- Pettersen, B., Coleman, L., 1981, ApJ, V.251, P.571–582
- Pettersen, B. R., Lambert, D. L., Tomkin, J., Sandmann, W. H., Lin, H., 1987, A&A, V.183, P.66-72
- Pettersen, B. R., Olah, K., & Sandmann, W. H. 1992, A&A, 96, 497
- Pettersen, B. R.; Panov, K. P.; Ivanova, M. S.; Sandmann, W. H., 1986, A&A Suppl. Ser. 66, 235
- Phan-Bao, N., Martin, E., Donati, J.-F., Lim, J., 2006, ApJ. 646, L73-L76
- Reiners, A., 2007, A&A 467, 259
- Reiners, A., Basri, G., Browning, M., 2009, ApJ, 692, 538–545
- Reuyl, D., 1943, ApJ, V.97, P.186
- Rodono, M., 1974, A&A, V.32, P.337
- Rojas-Ayala, B. et al. 2012, ApJ 748, 93
- Rojzman, G. Sh., Pisma v Astronomicheskii Zhurnal, vol. 10, Apr. 1984, p. 279-283
Soviet Astronomy Letters, vol. 10, Mar.-Apr. 1984, p. 116-118. Translation
- Romanyuk, Y., Svyatogorov, O., Verlyuk, I., Zhilyaev, B., 2001, The synchronous network of optical telescopes: a new instrument for stellar photometry., Proceedings of the 5th Hellenic Astronomical Conference 2001.
- Roques, P.,E., 1953, Publ. of the Astronomical Society of the Pacific, V.65, P.19
- Roques, P.,E., 1954, Publ. of the Astronomical Society of the Pacific, V.66, P.256
- Samus, N.,N., Durlevich, O.,V., Kazarovets, E.,V., Kireeva, N.,N., Pastukhova, E.,N., Zharova, A.,V., et al., 2012, General Catalogue of Variable Stars (Samus+ 2007-2012)
- Scargle, J., 1982, ApJ 263, 835-853
- Sciortino, S., Maggio, A., Favata, F., Orlando, S. 1999, A&A, 342, 502
- Schmitt, J. & Liefke, C., 2002, A&A, V.382, P.L9-L12

- Shakhovskaya, N. I., 1995, in Flares and Flashes, J.Greiner, H.Duerbeck, and R.Gershberg (eds), V.454, P.61
- Shakhovskoy, N. I., 1993, in Cataclysmic variables and related physics, O.Regeev and G.Shaviv (eds), Ann.Israel Phys.Soc., V.10., P.237
- Shibata, K. & Magara, M., 2011, Living Rev. Solar Phys. 8, 6
- Shkolnik, E., Liu, M., Neil Reid, I., 2009, ApJ 699
- Spiesman, W., Hawley, S., 1986, ApJ 92, 664
- Stauffer, J. R. & Hartmann, L. W., 1986, ApJ Suppl., V.61, P.531-568
- Stepanov, A. V., Kliem, B., Zaitsev, V. V., Furst, E., Jessner, A., Kruger, A., Hildebrandt, J., Schmitt, J. H. M. M., 2001, A&A 374, 1072
- Svestka, Z., 1976, Solar Flares, Geophysics and astrophysics monographs v.8, 225
- Terndrup, D., Krishnamurthi, A., Pinsonneault, M., Stauffer, J., 1999, Astronomical Journal, V.118, P.1814-1818
- Tinney, C. G., Delfosse, X., Forveille, T., 1997, ApJ, V.490, P.L95-L98
- Torrence, Ch., Compo, G., 1998, in Bull. of the American Meteorological Society, vol. 79, No. 1, 61
- Torres, C., Busko, I., Quast, G., 1985, Revista Mexicana de Astronomia y Astrofisica, V.10, Spec. issue, P.329-332
- Trimble Navigation Ltd., Acutime 2000 GPS Smart Antenna User Guide rev.B
- van Altena W., Lee J., Hoffleit E., 1995, The General Catalogue of Trigonometric Stellar Parallaxes (Fourth ed.).
- van de Kamp, P.; Worth, M. D., 1972, Astronomical Journal, V.77, P.762-763
- van Maanen, A., 1940, ApJ, V.91, P.503
- van Maanen, A., 1945, Publ. of the Astronomical Society of the Pacific, V.57, P.216
- Wachmann, A., 1939, B.Z, V.21, P.25

- Woodgate, B. E., Martres, M.-J., Smith, Jr., J. B., et al. 1984, *Advances in Space Research*, 4, 11
- Zaitsev, V. V., Kislyakov, A. G., Stepanov, A. V., Kliem, B., Furst, E., 2004, *Astronomy Letters*, vol. 30, 319
- Zappa, F., Cova, S., Ghioni, M., Lacaita, A., Samori, S., 1996. "Avalanche photodiodes and quenching circuits for single-photon detection". *Applied Optics* 35 (12): 1956–1976.
- Zhang, J. and Wang, J., 2002, *ApJ*, 566:L117-L120
- Zhilyaev B.E., Romanyuk Ya.O. and Svyatogorov O.A. 1992, *AZh.*, 69, 895
- Zhilyaev, B., Romanyuk, Y., Svyatogorov, O., Verlyuk, I., Kaminsky, B., Andreev, M., Sergeev, A., Gershberg, R., Lovkaya, M., Avgoloupis, S., Seiradakis, J., Contadakis, M., Antov, A., Konstantinova-Antova, R., Bogdanovski, R., 2007, *A&A*, 465, 1, 235-240
- Zhilyaev B. E., Romanyuk Ya. O., Verlyuk I. A., et al., 2000, *A&A*, 364, 641